ABSTRACT

WILLIAMS, NAKEYA DENISE. Mathematical Modeling of Cardiovascular Dynamics During Head-up Tilt. (Under the direction of Mette S. Olufsen.)

Short-term cardiovascular responses during head-up tilt (HUT) involve complex regulation in order to maintain blood pressure at homeostatic levels. Patient specific pulsatile and non-pulsatile models that use heart rate as an input to predict dynamic changes in arterial blood pressure during HUT are presented in this dissertation. This study shows how mathematical modeling can be used to extract features of the system that cannot be measured experimentally. More specifically, it is shown that it is possible to develop mathematical models that can predict changes in cardiac contractility and vascular resistance, quantities that cannot be measured invasively, but which are useful to assess the state of the system. The cardiovascular system is pulsatile, yet predicting the control in response to head-up tilt for the complete system is computationally challenging, and limits the applicability of the model. Therefore, a simpler non-pulsatile model is developed that can be interchanged with the pulsatile model, which is significantly easier to compute, yet it still is able to predict internal variables. The pulsatile and non-pulsatile models contain five compartments representing arteries and veins in the upper and lower body of the systemic circulation, as well as the left ventricle. A physiologically based sub-model describes gravitational pooling of blood into the lower extremities during HUT. For both the pulsatile and non-pulsatile models, cardiovascular regulation models adjust cardiac contractility and vascular resistance to the blood pressure changes during HUT. In addition, an optimal control approach involving a direct transcription method, is explored to predict changes in cardiac contractility and vascular resistance during HUT and head-down tilt (HDT). Head-down tilt for our purposes is defined as tilting the patient back to supine position after head-up tilt.

The model is rendered patient specific via the use of parameter estimation techniques. This process involves sensitivity analysis, prediction of a subset of identifiable parameters, and nonlinear optimization. The approach proposed here was applied to analysis of carotid blood pressure (carotid and aortic for the pulsatile model) and heart rate HUT data from healthy young subjects. Results showed that it is possible to identify a subset of model parameters that can be estimated allowing the models to predict changes in arterial blood pressure observed at the level of the carotid bifurcation. It is also shown that a simpler non-pulsatile model can be used in conjunction with other physiological models, yet still portray the same dynamics as the pulsatile model. We also show that an optimal control approach is useful for controlling quantities that effect the cardiovascular system during HUT in comparison to numerical optimization with piece-wise linear splines. Moreover, the model estimates physiologically reasonable values

for arterial and venous blood pressures, blood volumes, and cardiac output for which data are not available.

Mathematical Modeling of Cardiovascular Dynamics During Head-up Tilt

by
Nakeya Denise Williams

A dissertation submitted to the Graduate Faculty of
North Carolina State University
in partial fulfillment of the
requirements for the Degree of
Doctor of Philosophy

Applied Mathematics

Raleigh, North Carolina

2014

APPROVED BY:

_____   _____
Hien T. Tran   Stephen L. Campbell

_____   _____
Ernest L. Stitzinger   Mette S. Olufsen
                                                          Chair of Advisory Committee

DEDICATION

To my mother, Elizabeth, for always providing me with words of encouragement and being my personal cheerleader.

BIOGRAPHY

Nakeya Denise Williams was born and raised in Baltimore, Maryland. Since grade school, she has always had an interest in mathematics and its applications. After graduating from The Institute of Notre Dame in 2004, she attended Marymount University in Arlington, VA. However, she missed her hometown and moved back to Baltimore to attend Morgan State University in the Spring of 2005. There she was introduced to mathematical modeling of biological systems and infectious diseases. While pursuing her Bachelors degree, she participated in the Historically Black College and University Undergraduate Program (HBCU-UP) and gained experience in engaging in mathematical research. She was awarded the opportunity to attend a workshop on infectious disease modeling in Capetown, South Africa during the summer after her junior year at Morgan Stat, cementing her desire to attend graduate school. After graduating in 2008, Nakeya moved to Raleigh, NC to pursue her doctorate in Applied Mathematics at North Carolina State University. She began working with Dr. Mette Olufsen to study predictive modeling of cardiovascular dynamics. She received her Masters degree in 2010 in Applied Mathematics at NC State and visited Denmark in 2012 to collaborate with clinicians for her study on the effects of orthostatic intolerance on cardiovascular regulation. While in graduate school, Nakeya also enjoyed her teaching assistantship and tutoring all levels of students. She spent her summers mentoring undergraduates in the NC State Research Experiences for Undergraduates (REU) program and tutoring elementary students. After completing her PhD, she will be relocating to West Point, NY for a postdoctoral position in the Department of Mathematical Sciences at the United States Military Academy.

ACKNOWLEDGEMENTS

TABLE OF CONTENTS

vi

LIST OF TABLES

<h1 align="center">LIST OF FIGURES</h1>

xv

Chapter 1

Introduction

Orthostatic intolerance (OI) occurs when the act of standing upright causes an imbalance in blood pressure and flow in the body. It effects an estimated 500,000 Americans and generally affects young women (female-to-male ratio at least 5:1), typically less than 45 years of age [113]. The majority of these patients experience an exaggerated increase in heart rate (more than 30 beats/minute) when they stand. This boost in heart rate is an indication that the cardiovascular system is working hard to maintain blood pressure and flow to the brain in the presence of deficient cardiovascular regulation. Other than hypertension, OI is the most common disorder associated with blood pressure regulation. It is also the most frequently experienced dysautonomia, the reason for the majority of patients referred to centers specializing in autonomic disorders. The cause of OI is generally unknown. In fact, it is so poorly understood that over the years it has been given at least 18 different titles, including neurocirculatory asthenia, mitral valve prolapse syndrome, postural orthostatic tachycardia syndrome (POTS), and hyperadrenergic orthostatic tachycardia. It is now officially known as orthostatic intolerance by the American Autonomic Society [113].

Considering that the etiology of OI is abstruse, the symptoms are vague and plentiful. They include lightheadedness, dizziness, anxiety, and fatigue. The most common symptom is syncope, the clinical term for fainting. A vital characterization is that symptoms are worsened by upright posture, and are relieved when lying down. When a human stands, approximately 750 ml of thoracic blood is translocated downward due to gravity (Figure 6.7), reducing the venous return and cardiac filling [64, 121]. This reduces the blood volume in the heart by 20% over about 15 seconds and lowers central venous pressure. Consequently, the fall in cardiac contractility, mediated by the Frank-Starling mechanism [80], lowers the stroke volume. This reduces the pulse pressure and also the mean arterial pressure. Baroreceptor reflexes normally accommodate for the decrease in pressure very rapidly. Baroreceptor nerve signals located in the carotid sinuses sense the drop in blood pressure causing sympathetic nervous system activation and
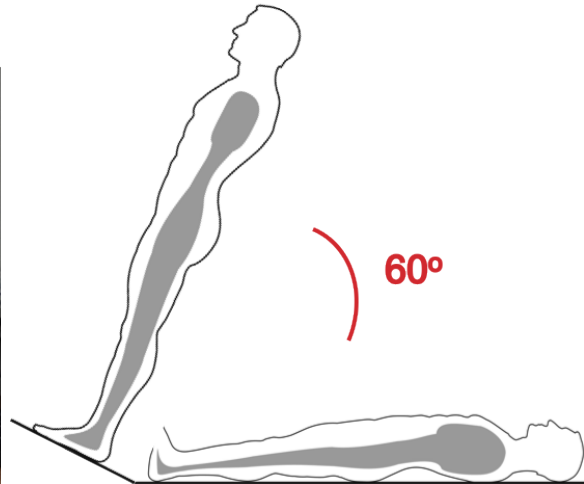
Figure 1.1: The HUT test: The subject depicted is tilted to an angle of 60 degrees at a constant speed of 15 degrees per second. Upon HUT blood is pooled in the lower extremities.

parasympathetic withdrawal, modulating the release of norepinephrine and acetylcholine. This in turn leads to an increased heart rate, cardiac output, and vasoconstriction. If the autonomic nervous system is faulty, as in patients with chronic orthostatic hypotension, there is a gradual decrease of blood pressure until the brain is no longer sufficiently perfused, causing a gradual loss of consciousness, invoking syncope [113].

Diagnosis of patients with orthostatic intolerance include procedures stimulating the cardiovascular and nervous systems. Some of these are designed to look at specific parts of these systems, e.g. the valsalva maneuver and transcranial doppler tests, and others are intended to evoke patient symptoms in a controlled setting where doctors can monitor the physiology responsible. Head-up tilt (HUT) testing has become the standard method to diagnose syncope and other symptoms of OI [64, 88]. Measurements taken include echocardiogram (ECG) recorded using standard precordial leads and blood pressure recorded using photoplethysmography (Finapres Medical Systems B.V.). The test is simple, it involves a motorized table, with a foot support raising the patient from supine to approximately 60-70 degrees upright (Figure 1.1) without the use of the patient's own muscles. The patient is tilted to an upright position until systolic blood pressure drops to 70 mmHg or the appearance of orthostatic symptoms such as dizziness, lightheadedness or syncope. The purpose is to hopefully reproduce the patient's problem in a controlled laboratory setting and gain knowledge on what cardiovascular mechanisms are effected. However, these tests are unable to give clinicians information on aspects of the cardiovascular system that are affected by HUT, including cardiac contractility and vascular resistance.

Diagnosis of OI is ambiguous. Patients can undergo extensive clinical evaluation without identification of a specific abnormality, and therefore a large number of patients remain undiagnosed [113]. Another problem in the diagnosis is its overlap with other conditions such as Chronic Fatigue Syndrome (CFS), Neurally Mediated Syncope (NMS), and physical deconditioning (deterioration of heart and skeletal muscle due to sedentary lifestyle, debilitating disease, or prolonged bed rest. Treatment of OI also represents a real challenge. The causes and pathophysiology vary between patients. Because of this, not all patients will respond the same way to a treatment. Therefore, treatment plans must be tailored to each patient for maximum efficacy. Unfortunately, there are no trials to advise clinicians on treatment options. Two typical approaches are to try to increase blood volume and to promote vasoconstriction [113]. Volume expansion can be improved by increasing salt intake. Ideally, this can be done with diet alone, but when this is unsuccessful, prescription 1g sodium chloride (salt) tablets can be given to supplement sodium intake. This should be accompanied by an increase in water intake.

Drugs that affect the sympathetic nervous system have also been advocated to adjust blood volume and promote vasoconstriction. Some experts have justified the use of drugs that prevent central sympathetic outflow, due to the belief that increased central sympathetic outflow will tend to reduce blood volume over the long term. However, drugs have side affects and are not always effective for every patient. Desmopressin (DDAVP) is an synthetic derivative of vasopressin that acts to decrease urine formation by increasing water reabsorption in the kidneys leading to plasma volume expansion. Clonidine (Catapres) and methyldopa (Aldomet) act on the brain to decrease sympathetic nervous system tone, stabilizing heart rate and blood pressure. Both have been advocated, but without convincing evidence that they are reliable treatment [113]. Another, and contradictory, approach has been to use drugs such as midodrine and phenylpropanolamine. They cause vasoconstriction (increase peripheral vascular resistance and decrease venous capacitance) and help to decrease venous pooling. Beta blockers, like Propanolol, have also been suggested for use in patients with OI. These block the receptors that are responsible for the effects of epinephrine and norepinephrine, but as with all the other drugs, evidence for their effectiveness is lacking.

OI can be gravely disabling and can be progressive in nature, particularly if it is caused by an underlying condition which is deteriorating. As mentioned, this disorder is difficult to diagnose and treat, and not all patients respond the same to treatments. Therefore, improving characterization of the underlying circulatory responses may lead to a clarification of some of the issues, and may facilitate the discovery of the pathophysiology of this disorder. Understanding cardiovascular regulation during HUT is difficult and involves complex measurements that are experimentally difficult to achieve, hence mathematical modeling is a great alternative to study cardiovascular dynamics. Moreover, the patient specific models may be used to learn about the impact on treatment of disease. The goal of this study is to develop pulsatile

and non-pulsatile patient specific compartmental models that predict changes in arterial blood pressure during HUT and study quantities that impact dynamics. To counteract the response of the cardiovascular system when the tilt occurs, i.e., the drop in blood pressure, quantities representing vascular peripheral resistance and cardiac contractility are made time-varying by use of piece-wise linear splines and an optimal control approach.

1.1 Summary of the dissertation

My work focused on three aims: (1) development of a patient-specific pulsatile model that models the effect on the cardiovascular control system for patients suffering from OI during head-up tilt (HUT) (2) development of a non-pulsatile model that can accurately be interchanged with the pulsatile model and predict dynamics for HUT and head-down tilt (HDT)[1]; and (3) analyzing a piecewise method and an optimal control method to regulate peripheral resistance and cardiac contractility in response to the HUT by allowing these quantities to vary with time. Several papers have been or will be submitted for publication on this work. This dissertation will consist of general information pertinent to all papers given in chapters 2, 3, and 4, as well as the individual papers themselves given in chapters 5, 6, and 7. Therefore, there may be some repetition and overlap throughout this manuscript.

For aim (1), a compartmental pulsatile model analogous to an electrical circuit was developed, along with a physiologically based sub-model describing gravitational pooling of blood into the lower extremities. Furthermore, a model predicting regulation through the use of piecewise linear splines and estimated using least-squares optimization [99] was developed. For aim (2), a simpler non-pulsatile model that can be interchanged with the pulsatile model to describe cardiovascular dynamics during HUT and HDT was developed, which is significantly easier to compute, yet it still is able to predict internal variables [4]. For aim (3), the least square optimization cardiovascular regulation model using piecewise linear splines is compared to an optimal control method using a collocation method to adjust peripheral resistance and cardiac contractility [98].

Newly developed methodologies for sensitivity analysis, parameter subset selection, and parameter estimation [104] were used to choose model parameters that are to be estimated, while the technique developed in [75] was utilized for the least squares numerical optimization of model parameter values. The methodology for the optimal control approach to regulate model parameters was developed and implemented using the general pseudo-spectral optimal control software, GPOPS [11].

- Chapter 2 introduces the physiological background necessary for developing the models

---

[1]For our purposes head-down tilt (HDT) is the process of tilting the patient back to supine position after HUT.

given in Chapters 4, 5 and 6. The chapter contains general descriptions of the cardiovascular system, including the heart and vasculature. Moreover, regulation of the cardiovascular system is described including autonomic regulation and arterial blood pressure regulation.

- Chapter 3 reviews previous efforts to model blood pressure and flow dynamics, along with discussion of the advantages and disadvantage of those methods.

- Chapter 4 presents model analysis and techniques used throughout this thesis, including bases for model development, sensitivity analysis, subset selection, and optimal control. This chapter discusses how models were rendered patient specific using a gradient-based optimization algorithm minimizing the least squares error between data and the model presented in chapters 5 and 6. Also, discussed are optimization schemes used to predict time-varying parameters based on linear piecewise splines and on an optimal control method discussed in Chapter 7 to regulate peripheral resistance and cardiac contractility.

- Chapter 5 presents a pulsatile compartment cardiovascular model designed to predict blood pressure and flow dynamics during HUT as well as peripheral resistance and cardiac contractility using a piecewise linear approach. This published study shows how to estimate constant parameters and time-varying quantities allowing the model to fit data measured at the level of the carotid artery. We also show how carotid pressure can be calculated from data measured at the level of the aorta and that similar parameter estimates are obtained comparing model outputs against the measured and calculated carotid pressures [99].

- Chapter 6 introduces a comparison between a non-pulsatile model that can predict dynamics during HUT and HDT and the pulsatile model given in Chapter 5. Although a pulsatile model for the cardiovascular system is beneficial for numerous problems, it can be adequate to analyze the system with the simpler non-pulsatile model. The non-pulsatile model development is described in detail illustrating advantages and disadvantages in comparison to the pulsatile model. This study showed that results predicted with the non-pulsatile model can be incorporated in the pulsatile model in the study of HUT dynamics using the least-squares optimization method to predict time-varying quantities. We also describe how the non-pulsatile model can be used for longer time scales to include HUT/HDT dynamics. This work has been published in a conference proceedings [4] and is being prepared for submission for publication in a journal.

- Chapter 7 shows that optimal control can be used with the non-pulsatile model to predict the time-varying quantities, peripheral resistance and cardiac contractility. Model results were compared to the piecewise linear spline approach presented in Chapters 6 and 7.

The implementation of the optimal control approach results into the pulsatile model are also discussed. Tel can be used for longer time scales to include HUT/HDT dynamics. This work has been published in a conference proceedings [98] and is being prepared for submission for publication in a journal.

- Chapter 8 provides some simulations illustrating the pulsatile model predicting the effect of the drugs (Desmopressin, midodrine and phenylpropanolamine) that are used as treatments for OI.

- Finally, Chapter 9 will include the closing remarks and summarize the results of the dissertation, including ideas for future work.

Chapter 2

Physiological Background

This chapter presents an overview of the physiology involved in modeling the cardiovascular control system. General information comes from Burton [21], Levick [80], and Smith and Kampine [130]. Section 2.1 discusses the relevant features of the cardiovascular system (CVS), while Section 2.2 discusses aspects of autonomic regulation of blood pressure within the cardiovascular system.

2.1 The cardiovascular system

The primary responsibility of the cardiovascular system (CVS) is the transportation of nutrients (i.e. oxygen, amino and fatty acids, and vitamins) to the tissues; and removing of gaseous wastes (i.e carbon dioxide and urea) from the body. The CVS is a control system that distributes hormones to the tissues, and secretes bioactive agents (i.e. peptides, renin, and nitric acid) [80]. The system consists of two main components that form a closed network, the larger systemic division composed of the aorta, arterial branches, capillaries, veins, and vena cavae; and the much smaller pulmonary division consisting of the pulmonary artery, capillaries, and the pulmonary veins. The systemic vessels supply and drain all the tissues and organs of the body, while the pulmonary vessels facilitates the primary exchange of oxygen and carbon dioxide. Although the systemic and pulmonary divisions function in a similar manner, they have some vital differences; the systemic division has a much higher volume, its vessels are longer and thicker, and it operates under higher pressure and with more resistance to flow. Blood is driven through the systemic and pulmonary divisions by a blood pressure differential generated by the heart, see Figures 2.1 and 2.2. Figure 2.1 depicts the blood flow through the systemic and pulmonary circuits, while Figure 2.2 shows the distribution of pressure and the pressure differentials for the various vessels in the two circuits.

Veins serve primarily as storage vessels, although they do have some regulation properties
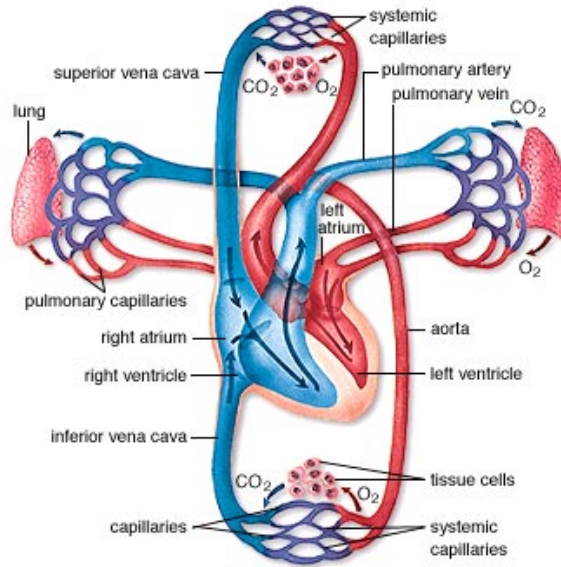
Figure 2.1: Blood flows from the left ventricle through the systemic arteries and veins to the right atrium. It is expelled from the right ventricle and pumped through the pulmonary circulation back to the left atrium. Systemic artery and pulmonary veins contain blood high in O_2 and low in CO_2, while systemic veins and pulmonary arteries are low in O_2 and high in CO_2.

and the arteries function to distribute blood flow and pressure throughout the body. The distensibility of vessels (i.e. the ability of the vessel to stretch) results in changes in vessel volume in response to pressure changes. The total blood volume in a typical 70 kg man is about 5.5 liters [80]. Also, total blood volume consists of stressed and unstressed blood volume as proposed by [30]. Unstressed volume is the volume needed to fill the circulation to the point where the pressure starts to rise. The stressed volume is the volume in the circulation minus the unstressed volume. Volumes and percentages for an individual with a total blood volume of 4544 ml are given in Table 2.1. Total blood volume percentages are illustrated in Figure 2.3. Due to their distensibility and size, veins and venules contain about two-thirds of the total blood volume, while one-sixth is on the arterial side. However, the pressure distribution is quite different, being a nearly inverse relation to the volume distribution, see Figure 2.4 which illustrates total blood volume percentages in conjunction with pressure value through out the systemic circulation. The relationship between pressure, volume and flow will be discussed further in Section 2.1.2.
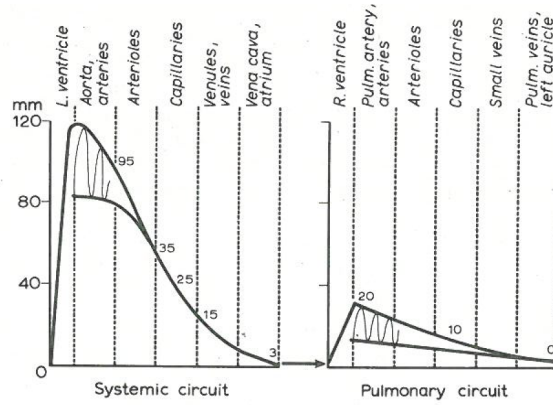
Figure 2.2: The distribution of intravascular pressures in the systemic and in the pulmonary circuits. The attenuation of the pulse pressure (systolic minus diastolic) is indicated. The numbers on the curves are mean pressures. Note, mean pressure decreases exponentially in systemic circulation and linearly in the pulmonary circulation. Reprinted w.p. from [21].
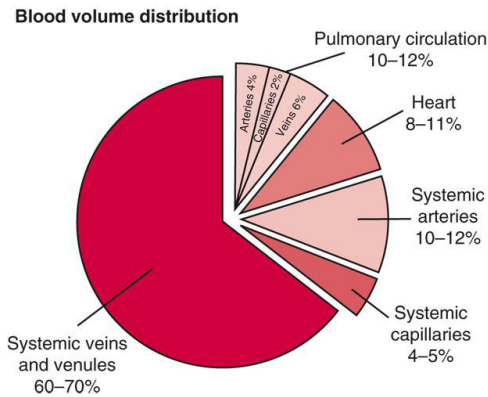
Figure 2.3: Approximate distribution of 5.5 liters blood in a supine, resting man. On standing, the percentage of blood in the lungs falls by about one-third, as does the volume in the heart, while the volume in the peripheral veins increases. Reprinted w.p. from [41].

2.1.1 The circulation of blood

The heart propels the blood through both divisions of the CVS system. It consists of four chambers, two for the right and two for the left side of the heart, which supply the pulmonary and systemic systems, respectively. Each side of the heart is comprised of an atrium and a ventricle. The right ventricle propels deoxygenated blood through the pulmonary artery to the

9

lungs, see Figures 2.1 and 2.5. Pulmonary veins then return oxygenated blood from the lungs to the left side of the heart, completing the short, low pressure pulmonary circulation. The left ventricle pumps oxygentated blood to the tissues of the body. The tissues absorb a portion of the oxygen, and the semi-deoxygenated blood returns via the superior and inferior vena cavae, to the right atrium. This completes the high pressure systemic circulation. The two sides of the heart eject the same volume of blood per unit time, called the cardiac output (CO). Valves at the inflow and outflow of the ventricles allow pressure to build up within the ventricles and prevent blood from flowing backwards. Atrioventricular valves separate the atria and the ventricles and semilunar valves are located at the exit of the ventricles. In the left ventricle these are named the mitral and aortic valves, and in the right ventricle they are the tricuspid and pulmonary valves, see Figure 2.5.

The left and right sides of the heart each consist of a pump, distributing system, exchange system, and a collecting system. The pumps are the right and left ventricles. Typically the two ventricles are in nearly identical phase and rhythm because they are composed mainly of myocardium (i.e. cardiac muscle), which compresses both chambers simultaneously. The my-

Table 2.1: Blood volumes and percentage of total blood volume, from Beneken and Dewit [30]. Volumes are scaled to a total blood volume of 4544 ml.

Vessel	Volume (ml)	Stressed volume %	Total %
Ascending aorta	82.0	1.80	35.4
Thoracic arch	91.0	2.00	33.0
Thoracic aorta	89.0	1.96	33.7
Abdominal aorta	78.0	1.72	25.6
Intestinal arteries	23.0	0.51	26.1
Leg arteries	75.0	1.65	16.0
Head arteries	87.0	1.91	22.4
Arm arteries	244	5.36	7.40
Pulmonary arteries	119	2.62	58.0
Abdominal veins	315	6.93	3.20
Intestinal veins	649	14.3	6.50
Leg veins	295	6.49	12.9
Head veins	353	7.78	7.60
Arm veins	244	5.36	7.40
Inferior vena cava	530	11.7	7.90
Superior vena cava	530	11.7	7.90
Left ventricle	125	2.75	–
Right ventricle	125	2.75	–
Left atrium	80.0	2.72	–
Right atrium	80.0	1.95	–
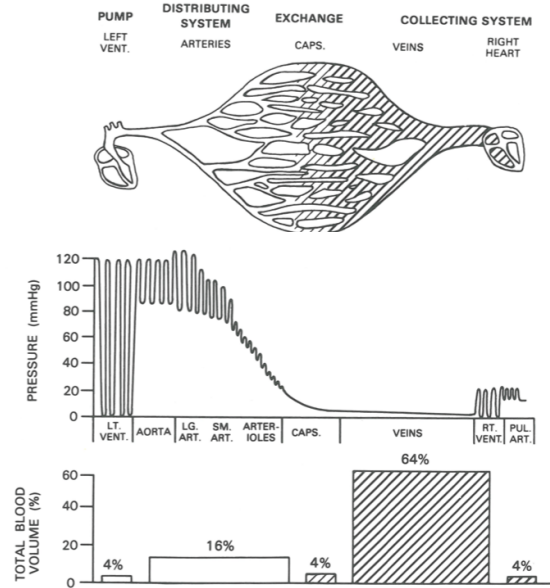
Figure 2.4: Pressure and volume distribution in the systemic circulation. Illustrating the inverse relationship between internal pressure and volume in different portions of the circulatory system. Reprinted w.p. from [130].

ocardium of the left ventricle is generally 8 to 10 mm thick, while that of the right ventricle is about 2 to 3 mm [130]. Because the heart is a muscle, it has the ability to contract and relax. The cardiac cycle describes this process and is comprised of the phases, systole (i.e. ventricular contraction) and diastole (i.e. ventricular relaxation) based on the position of the inlet and outlet valves. During systole, the internal ventricular pressures rise quickly to a peak. In the left ventricle, which is a high-pressure pump, typical systolic pressures reach 120 mmHg, while in the right ventricle, the low-pressure pump, systolic pressures would be about 25 mmHg, see Figure 2.2. Following contraction is diastole where the internal pressures fall quickly to near zero and the ventricles fill with blood [130].

At a rate of 75 beats per minute (bpm), the complete cycle for filling and emptying of the chamber would take 0.8 sec, see Figure 2.7. At the beginning of diastole, at a ventricular volume of about 60 ml, the aortic valve is closed while the mitral valve is open, allowing blood to fill the left ventricle at a low pressure, see Figures 2.6 and 2.7. At the end of ventricular filling, at about 120 ml, the ventricular muscle contracts while the ventricular volume is constant (iso-volumetric contraction), to increase the pressure inside the ventricle [80]. As the ventricular pressure exceeds that of the atrium, the mitral valve closes. Ventricular contraction continues to raise ventricular pressure until it exceeds pressure in the aorta, causing the aortic valve to

11
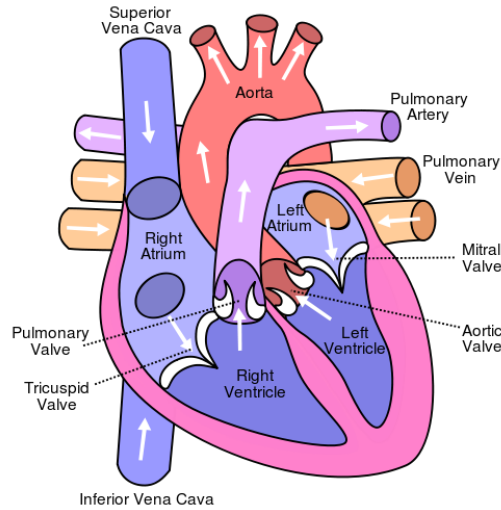
Figure 2.5: The four chambers of the heart and connecting vessels and valves. Reprinted w.p. from Wikimedia Commons [3].

open and blood to be ejected into the aorta.The aortic valve closes when the pressure in the aorta exceeds that in the ventricle. At this time the majority of the blood has been ejected. After a period of ventricular relaxation (i.e., iso-volumetric relaxation) at low ventricular volume the cardiac cycle is completed (Figures 2.6 and 2.7). It should be noted that for healthy individuals at no time are both valves open. The dynamics of the right ventricle mirrors that of the left ventricle except the systolic pressure is about 25 mmHg.

The distributing system of blood circulation involves the arterial system. The arteries are hollow cylindrical, branch-like structures, see Figure 2.4. Arterial pressure is pulsatile, meaning the heart ejects blood intermittently (systole), with rests in between (diastole). The pulmonary artery pressure is typically about 25/10 mmHg. The first number indicating systolic pressure and the second diastolic pressure. This pressure decreases to about 10 mmHg at the beginning of the lung capillaries, see Figure 2.2. In the systemic circulation, the aorta and its arterial branches are long and rather thick-walled. They transport blood to the smaller arteries and arterioles. Their internal pressure falls from approximately 120/80 mmHg at the beginning of the aorta to a constant mean pressure of about 25 mmHg at the arteriolar level of the capillaries.

Capillaries are the most important factor in **the exchange system**. They are tiny microscopic tubes that form a mesh-like structure, see Figure 2.4. Their large surface area facilitates the diffusion of O_2, CO_2, water, electrolytes, and nutrients through their walls. They have internal pressures that range from values of about 25 mmHg on the arterial side to approximately

10 mmHg on the venous side, see Figure 2.2. Although the capillaries have an immense total cross-sectional area, their combined volume is rather small in comparison to other vessels, see Figure 2.4.

The smallest venules to the largest terminal veins in the vena cavae comprise **the collecting system** of the circulation. It is responsible for draining blood back to the atria. Veins are thin-walled cylindrical structures that have a large capacity to hold blood. Veins below the heart have one-way valves that prevent back flow and hence aid in the transport of blood back to the heart. They have a low internal pressure ranging from approximately 10 mmHg near the capillaries to about 0 mmHg at the heart entrance, see Figure 2.2. In the upright individual, the vascular pressures in the lower extremities are increased due to the effect of gravity. This will be discussed in subsequent chapters.
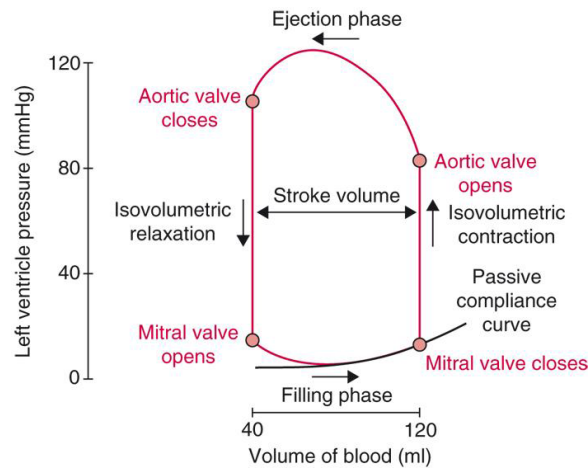
Figure 2.6: Pressure-volume loop for human left ventricle. Includes the phases of the cardiac cycle and the opening an closing of valves. As the ventricle contracts, the mitral valve closes; as ventricular pressure increases and exceeds aortic pressure, the aortic valve opens. Upon completion of ejection, ventricular pressure falls below aortic pressure, and the aortic valve closes. As ventricular pressure falls below atrial, the mitral valve opens and diastolic filling continues until the ventricle contracts again. Reprinted w.p. from [80].

2.1.2 Vasculature

The cardiovascular system is composed of a network of blood vessels. All blood vessels have an endothelial lining and consist of varying proportions of elastin, smooth muscle cells, and
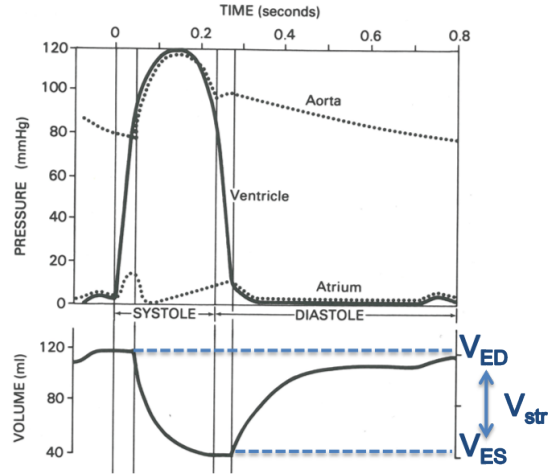
Figure 2.7: Changes in pressure, volume and flow in aorta, left ventricle and left atrium during human cardiac cycle. Right side (not shown) has similar patterns but lower pressures. Reprinted w.p. from [80].

collagen, see Figure 2.8. Table 2.2 gives percentages of compositions of varying blood vessel walls. As mentioned previously and seen in Figure 2.4 the pressure distribution in blood vessels is quite different to the volume distribution. This disposition of pressure and volume is in large part due to the composition and comparable elasticity of the arteries and veins, in particular, to their pressure-volume relations. Although it is accurate that the entire arterial tree serves as a distributing conduit, not all arteries are alike. From an anatomical and functional perspective they may be divided into two main groups that differ structurally and functionally from each other, and both in turn differ prominently from veins. Figure 2.9 shows the various types of blood vessels and their structures.

Table 2.2: Composition of the blood vessel wall (%) from [80].

	Endothelium	Smooth muscle	Elastin tissue	Collagen
Elastic artery	5	25	40	27
Arteriole	10	60	10	20
Capillary	95	0	0	5
Venule	20	20	0	60

Large arteries including the aorta are the most distensible as a result of their high elastin

14
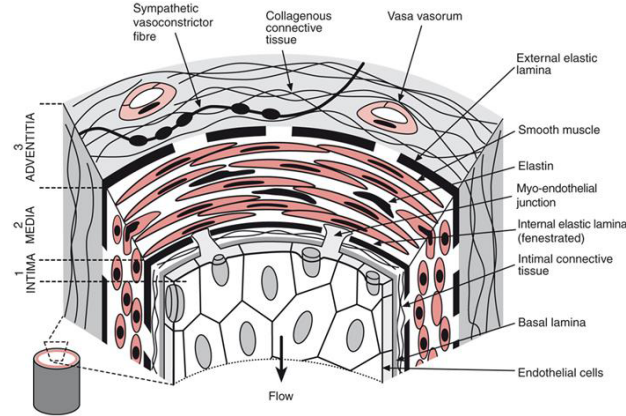
Figure 2.8: The structure of the wall of a blood vessel. Reprinted w.p. from [80].
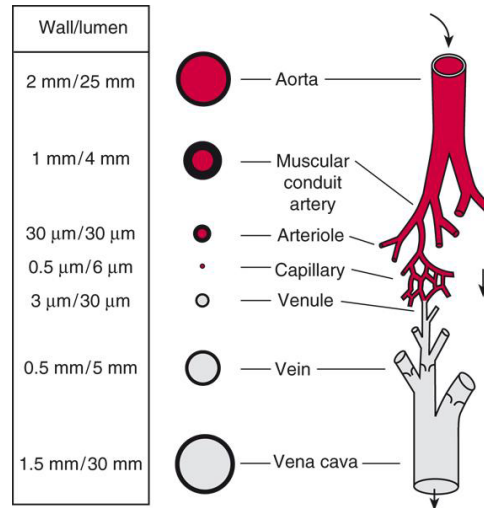
Figure 2.9: Different types of blood vessels, seen in cross-section and *en face*. Reprinted w.p. from [80].

content [130]. They are capable of substantial expansion and recoil and are known as the "pressure storers" of the circulation. All arteries consist of elastin, but the amount decreases as the arteries decrease in diameter. The arterioles have the ability to contract, as a consequence of their high content of circular smooth muscle cells causing them to constrict, thereby increasing the resistance to blood flow. Hence, these vessels are usually called the "resistance" vessels [130]. Their pressures typically range from 60 to 90 mmHg in the small arteries from 40 to

60 mmHg in the arterioles. Both arteries and veins branch in a bifurcating tree-like structure before reaching the capillary bed for a given tissue. The number of vessels and the total cross-sectional area of the vasculature increases exponentially as blood travels toward capillaries, see Figure 2.10. Table 2.3 shows a comparison of the number and size of different types of blood vessels in a dog.
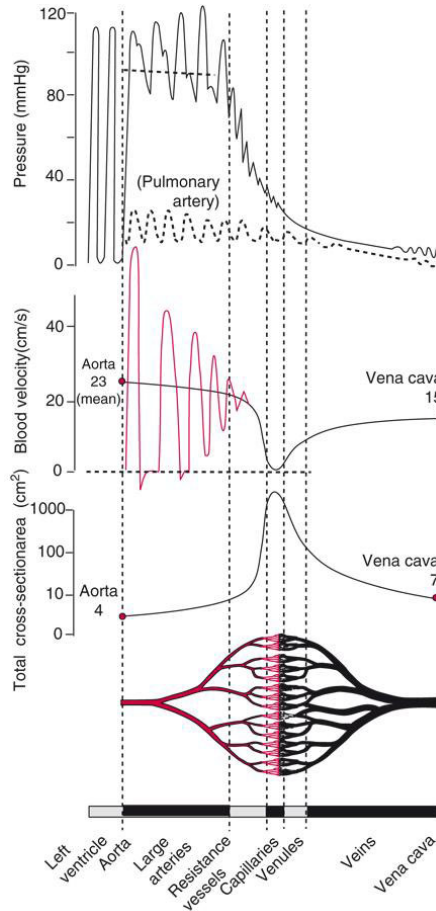
Figure 2.10: Branching of a typical vascular bed with changes in blood pressure, velocity, and the area of the arteries, capillaries, and veins within the circulatory system. The top graph shows the drop in mean pressure across the main arteries (dashed line) is only 2 mmHg. The large pressure drop across the terminal arteries and arterioles shows that they are the main resistance vessels. Low pulmonary pressure profile is also shown. The middle graphs depicts the pulsation of blood velocity (red line) and change in mean velocity across circulation (black line). The blood flow passes each vertical dashed line per minute, namely the cardiac output. Mean velocity is blood flow divided by the cross-sectional area of the vascular bed. The bottom graph depicts the increase in total cross-sectional area of the circulation in microvessels. Reprinted w.p. from [80].

16

Table 2.3: Comparison of number and size of different types of blood vessesl in a dog mesentry from [80] with permission.

Vessel	Number	Length(mm)	Diameter(mm)	Total cross-sectional area (mm^2)
Main artery	1	60	3	7
Arteriole s and small arteries	1,380,000	1.5-2	0.024-0.031	739
Capillaries	47,3000,000	0.4	0.008	2378
Venules	2,100,000	1.0	0.026	1151
Small veins	180,000	1-1.4	0.075-0.28	1019
Large veins	61	39-60	1.5-6	174

Blood is acquired from the arterioles for distribution throughout the systemic capillaries. Their vessel walls mostly consist of endothelial cells and are very thin. A single capillary is just wide enough to supply individual red blood cells (about 2-5 μm) carrying metabolites, with the blood flowing at a relatively slow rate. This combination of characteristics allows for the easy diffusion of metabolites between the capillaries and tissues [80]. Unlike the arteries, the network of capillaries forms a mesh-like structure, see Figure 2.10.

The veins are very thin-walled and consist primarily of collagen, a non-elastic connective tissue protein that slightly stretches. They have the ability to store a large volume of blood while incurring only minimal pressure change [130]. They grow into a branching structure reversed from that of the arterial tree, see Figure 2.10. Their pressures are low, ranging from about 10 mmHg at the ends of the capillaries to about 2 mmHg at the entrance of the vena cavae to the heart. As depicted in Figures 2.3 and 2.4, the venous system generally contains about four times more blood than the arterial system; yet, if more blood is infused into the vascular system, 90% of the new fluid will be taken up the veins due to their great distensibility. Consequently, the veins are known as the "volume storers" of the circulation [130].

2.2 Regulation of the cardiovascular system

There are two primary objectives of cardiovascular regulation: (1) the conservation of a sufficient and relatively constant arterial pressure; and (2) an adequate regulation of blood flow through local tissues to guarantee proficient metabolism, capillary exchange of gases and nutrients, and temperature balance. This study focuses on the first objective.

Arterial blood pressure is perhaps the most essential regulated component in the cardiovascular system. The nucleus solitary tract (NTS), the site of the most critical cardiovascular control centers in the body, regulate the arterial pressures primarily via adjustment of cardiac contractility and peripheral resistance. However, the medullary cardiovascular centers are them-

selves influenced by impulses from higher neural centers via parasympathetic and sympathetic activity and by several sensors throughout the body, most notably arterial baroreceptors.

2.2.1 Arterial blood pressure regulation

The mechanism by which arterial pressure is controlled is dependent upon whether long-term or short-term adjustments are needed. Long-term arterial pressure modifications (weeks and months) are generally produced through changes in extracellular fluid and blood volume and renal mechanisms. The latter are heavily influenced by neurohormonal factors that control water and sodium excretion by the kidneys and are not discussed in more detail here.
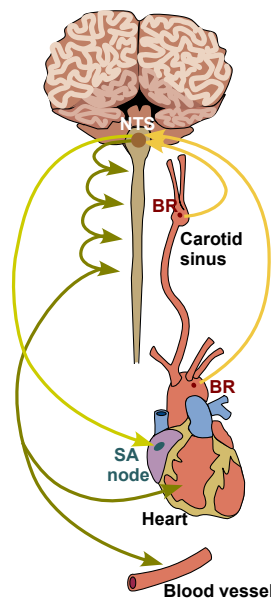
Figure 2.11: The aortic and carotid sinus baroreceptors and their central connections. The baroreceptors respond to alterations in blood vessel wall distention, which decrease their nerve firing rate. The sympathetic and parasympathetic nervous systems are then signaled allowing for changes in peripheral resistance, heart rate, and cardiac contractility.

On the other hand, short-term modifications (over seconds to hours) are intended to remedy temporary imbalances of pressure such as those caused by postural change, hemorrhage, or exercise. The response to the cardiovascular disturbance is a combination of adjustment of the local blood vessels to the altered volumes and pressures; and autonomic neural responses mediated via the parasympathetic and sympathetic nervous systems intended to return the
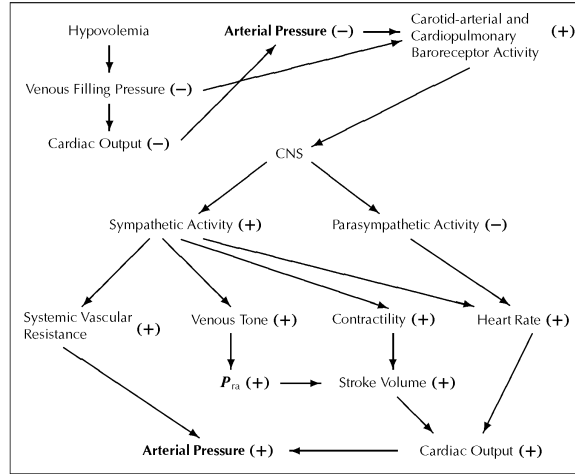
Figure 2.12: Baroreceptor control loops. A decrease in blood volume (hypovolemia) results in a decrease of venous filling pressure which leads to a decrease in cardiac output. This decrease causes a decrease in arterial blood pressure, which is sensed by the baroreflexes and chemoreflexes in the carotid and aortic sinuses. These sensors could also be activated by the decrease in venous filling pressure. The signaling of those receptors are mediated by the central nervous system resulting in parasympathetic withdrawal and sympathetic activation. Vascular resistance, venous tone, contractility and heart rate are all increased due to increased sympathetic activity, while parasympathetic withdrawal also increases heart rate. The increase of venous tone leads to an increase in right atrial pressure and that change in conjunction with the change in contractility causes the stroke volume to increase. The rise in heart rate as well as the rise in stroke volume causes the cardiac output to increase, which along with the change in vascular resistance leads the arterial blood pressure to return to homeostasis.

arterial pressure to homeostasis. This work will focus on short-term adaptation of arterial blood pressure.

2.2.2 Arterial baroreceptors and short-term regulation

Short-term regulation of blood pressure refers to control mechanisms that respond in seconds or minutes to stabilize blood pressures and it is important for the prompt control of orthostatic stress [66]. Short-term control depends primarily on the baroreflex response, which stabilizes pressure by means of neural negative feedback. The baroreceptors, located in the carotid sinus and the aortic arch, see Figure 2.11, respond to changes in vessel wall distention due to changes in arterial pressure. Decreased arterial pressure decreases vessel wall distention, which

decreases the baroreceptor nerve firing rate sent to the medulla The medulla generates a signal and disperses it through the sympathetic and parasympathetic systems of motor neurons. The sympathetic system is stimulated in response to decreased baroreceptor firing rate. Increased sympathetic outflow gives rise to an increase in norepinephrine, which in turn leads to vessel constriction, decreased peripheral resistance, increased heart rate, and increased cardiac contractility after a delay within 5-10 cardiac cycles. As a consequence, stroke volume and cardiac output increase, resulting in an increase in blood pressure. The decrease in baroreceptor firing rate also decreases the activity to the parasympathetic nerve channels. Parasympathetic withdrawal leads to a decrease in the release of acetylcholine, which speeds up cardiac electrical conduction leading to an increased heart rate within 1-2 cardiac cycles [130]. The short-term neural baroreflex feedback loop response is given in Figure 2.12.

In this study, the systemic circulation is modeled, while the pulmonary circulation is not considered. The afferents of the control of the baroreflex is not directly modeled. Instead we focus on predicting the impact on the vascular targets of heart rate, cardiac contractility, and vascular resistance.

Chapter 3

Cardiovascular Models

The cardiovascular system is a complex structure and its regulation makes it difficult to model the system as a whole. Simplifying assumptions are made depending on the objective of the study. Blood pressure and flow can be modeled using approaches ranging from detailed three-dimensional models of local structure and flow patterns to system level models designed to model global features. Furthermore, the cardiovascular control can be modeled using anything from empirical models down to elaborate molecular models.

A large number of previous studies have analyzed cardiovascular regulation of heart rate from a medical, statistical, and modeling point of view. These studies can be separated in two groups: multi-dimensional models and global system level models. Multi-dimensional models are useful for examining local flow behavior on a small scale. This is beneficial when modeling fluid dynamics of a specific artery or the heart itself. For example, Peskin and Mcqueen [112] developed a three-dimensional model for blood flow in the heart, using the immersed boundary method and Viscardi et al. [38] developed a model to test the effect of bicuspid aortic valve geometry on ascending aorta flow using two and three dimensional fluid dynamic models. Though these models give excellent insights into a distinct portion of the body, their use is restricted to localized investigations. Additionally, these models are often formulated as open-loop input/output models which do not accurately describe the closed-loop features of the cardiovascular system.

Global models are commonly developed to gain qualitative insight of the system. They can more easily integrate closed-loop phenomena and feedback controls to the models. In system-level models, several regions of the body are often lumped together in compartments. Generally, these models predict blood pressure and flow in and between compartments representing locations in the cardiovascular system using electrical circuits with capacitors, resistors, and inductors. Lumped parameter compartmental models can have states that represent quantities that pulse with cardiac dynamics (pulsatile models), e.g., [92, 93, 118, 138] or mean values aver-

aged over the timespan of an entire cardiac cycle (non-pulsatile models), e.g., [55, 73, 85, 105]. Pulsatile models are advantageous when analyzing dynamics within heart beats and can be used to understand how modulation of the system effects pulsatility. Non-pulsatile models tend to be simpler and have the advantage of being able to analyze dynamics over longer time-scales, as well as being able to couple with more complex models.

Kappel and Peer [73] developed a compartmental model to predict mean pressures during baroreflex response under a submaximal workload. In this study, the blood flow was non-pulsatile, which made it easier to use optimal control techniques. Despite the simplicity of the Kappel and Peer model, it gives a rather satisfactory description of the regulation process acting on the cardiovascular system in response to a submaximal workload by a single input/single output control system. Ottesen's baroreflex model [105] is another example which involves non-pulsatile flow and averaged state quantities over several cycles. His model is an open-loop model that predicts the nonlinear baroreflex-feedback mechanism involving time-delay based on physiological theory and empirical facts. Though the model is easily analyzed in the same manner as the model by Kappel and Peer, the open-loop feature disregards effects of regulatory responses produced by the circulation.

Patient specific models combine models with data, allowing for patient specific estimation of model parameters. Estimating model parameters involves solution of an inverse problem, i.e. given a model and data one has to estimate the model parameters to allow the model to fit the data [59]. In general, this problem is difficult to solve, and typically, no unique analytical solution can be found [125]. Some studies have successfully developed patient specific models of the cardiovascular system, but most of these do not include pulsatility [55, 67, 85]. There are a few models that include pulsatility [93, 131], though the model by Olufsen et al. [93] estimated too many model parameters and the model by Pope et al. [131] only addressed how to estimate parameters for a subject in supine position. Other contributions include the study by Ten Voorde et al. [134] who developed a model predicting short term blood pressure and heart rate variability for a healthy young male, and studies by Ursino et al. who modeled heart rate regulation [8, 138, 139]. The latter studies compared the model output with experimental data but did not address parameter estimation. Another example, is the recent model by [129], which computes heart rate regulation in rats. This study does address parameter estimation, but does not address parameter identifiability.

3.1 Lumped compartmental models

Lumped parameter pulsatile and non-pulsatile models can be constructed analogously to an electrical circuit. In these models, transmural pressure $p(t)$ (mmHg) is analogous to voltage and time-dependent volume $V(t)$ (ml) to charge, while volumetric flow rate $q(t)$ (ml/s) repre-

sents the electrical current. Each compartment has a compliance component $C(t)$ (ml/mmHg), similar to electrical capacitance, representing the change in volume given a change in pressure for that compartment, i and the hydrodynamic inertia of the blood flow is analogous to an inductance denoted by $L(t)$. For each of these compartments, blood pressure p_i (mmHg), also called transmural pressure, is defined as the difference between intravascular pressure p_{int} and extravascular pressure p_{ext}, i.e. $p_i = p_{int} - p_{ext}$. Extravascular pressure is typically constant at atmospheric pressure, so the convention is to set $p_{ext} = 0$. However, extravascular pressure can be non-constant due to the significance of tissue pressure with respiration as done in a model of cardiovascular and respiratory dynamics in congestive heart failure by [83].

Blood flow from high to low arterial pressure is opposed by resistance represented by properties of both the vessel and the fluid. This relationship is described by the physiological correspondence of Ohm's law for a given vessel group

$$q = \frac{\Delta p}{R}, \tag{3.1}$$

where $\Delta p = p_{i,in} - p_{i,out}$ (mmHg) is the pressure differential between the inlet i, in and outlet i, out of compartment, i and R (mmHg $\cdot$ s/ml) is the resistance of the vessel to blood flow. The nominal values for the models are obtained by calculating mean pressures. The perfusion of tissues can be regulated by adjusting arteriole resistance to enforce changes in blood flow to tissues as required, i.e. lowering R increases q. We use Ohm's law for hemodynamics as the fundamental relationship for building our models.

In a rigid cylindrical tube with Newtonian fluid, Ohm's law is equivalent to laminar flow and can be described by an adaptation of Navier-Stokes equations called Poiseuille's law given by

$$q = \frac{\Delta p \pi r^4}{8 L \nu},$$

which encompasses an explicit form for resistance

$$R = \frac{8 \nu L}{\pi r^4},$$

where r is the radius of the vessel, ν is the viscosity of the blood, and L is the length of the cylindrical vessel, leading to equation (3.1). Actually, blood flow is unsteady and for smaller vessels, viscosity is dependent upon the flow rate, hence the flow is neither Newtonian nor laminar. However, for larger vessels, viscosity is relatively constant, and flow is generally laminar away from the vessel opening. Consequently, Poiseuille's law is justifiable for a system-level model [103, 130]. However, since there are no explicit measures of viscosity, vessel length or vessel radius in our models, we do not utilize this law explicitly. Instead we use it as a qualitative assumption for development of models for vessel dynamics.

In lumped compartment models, stressed volume $V_{i,str}(t)$ (ml) is given by

$$V_{i,str}(t) = V_i(t) - V_{i,unstr} = C_i(t)(p_i(t) - p_{ext}), \quad p_{ext} = 0, \tag{3.2}$$

where $V_{i,unstr}$ (ml) is the unstressed volume, i.e. the volume at zero transmural pressure. From this point forward, "pressure" will refer to the transmural pressure across the vascular wall and "pressure differential" refers to the perfusion between two locations in a vessel. Flows between adjacent compartments have a resistance component, R (mmHg $\cdot$ s/ml). Using Ohm's law, we have the net change in volume for each compartment

$$\frac{dV_i(t)}{dt} = q_{in}(t) - q_{out}(t), \quad q_{in}(t) = \frac{p_{i-1}(t) - p_i(t)}{R_{in}}, \quad q_{out}(t) = \frac{p_i(t) - p_{i+1}(t)}{R_{out}}. \tag{3.3}$$

The notations $i-1$ and $i+1$ refer to the anterior and posterior compartments, respectively. A representative compartment is shown in Figure 3.1.
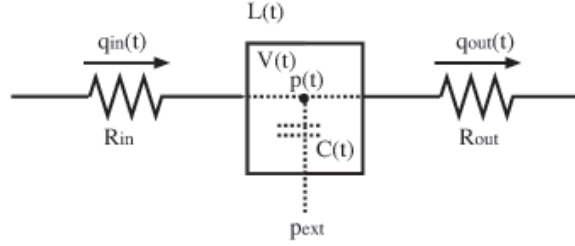
Figure 3.1: Representative vascular compartment of the cardiovascular system. V: volume (ml); p: transmural pressure (mmHg); p_{ext}: extravascular pressure $= 0$ (mmHg); C: compliance (ml/mmHg); R: resistance (mmHg $\cdot$ s/ml); q_{in}, q_{out}: volumetric blood flow rates into and out of the vascular compartment (ml/s).

A system of differential equations is obtained by differentiating (3.2) and equating with (3.3) giving

$$\frac{dV_i(t)}{dt} = C_i(t)\frac{dp_i(t)}{dt} + p_i(t)\frac{dC_i(t)}{dt} = q_{in}(t) - q_{out}(t). \tag{3.4}$$

An equation of this form is associated with each vascular compartment for both the pulsatile and non-pulsatile lumped compartmental model mentioned previously. For pulsatile models, the heart compartment equations can be derived from (3.3) as

$$\frac{dV_v(t)}{dt} = \frac{p_f - p_v}{R_{valve,in}} - \frac{p_h - p_a}{R_{valve,out}}, \tag{3.5}$$

where V_v is the ventricular volume, p_f is the ventricular filling pressure, p_v is the ventricular pressure, p_a is the arterial pressure at the outflow of the ventricle, and $R_{valve,in}$ and $R_{valve,out}$ are the inflow and outflow valves of the ventricular, respectively. The non-pulsatile model heart compartment, however, involves functions depicting the averaged cardiac cycle, e.g. Starling's law given in Kappel et al. [73].

A component that is not present in models discussed in this thesis, but is used by others [20, 108] is inductance, generally denoted by L. It is used to reduce the errors in the low frequency range that arise in compartment models, however due to its difficulty to estimate it is often omitted. Equations involving inductance can be included in the heart compartment and are of the form

$$\frac{dq_i}{dt} = \frac{1}{L_i}(p_i - p_{i+1}).$$

Inductance in a cardiovascular model, depicts the inertial effects of blood in the ventricle. It can contribute to modeling the ejection phase of the cardiac cycle. The inertial effects of blood in the ventricle tend to lower root aortic pressure in early systole increase pressure in late systole. Inertial effects were taken into account in Danielsen and Ottesen [28] and Beregovaya and Korenovskaya [86] for this purpose.

From this point forward all pressures, volumes and flows are assumed to be time-dependent quantities and they are to be denoted by p, V, and q except where noted otherwise. The parameters R and C can be set as constants or modeled as functions of time, pressure, or other relevant physiological quantities.

3.2   Cardiac models

As discussed in Section 2.1.1, the right side of the heart generates pressure for the pulmonary circulation and the left side for the systemic circulation. The same mathematical ventricular function could be used for each heart chamber within a given cardiovascular model, the differences being only in parameter values that represent the model function. Various complex nonlinear models have been developed to describe the pulsatile pumping of the heart. One approach is to utilize a time-varying elastance model first developed by Suga et al [54] where the ventricular pressure p_{lv} (mmHg) is defined as

$$p_v(t) = E_v(t)\left[V_v(t) - V_d\right], \tag{3.6}$$

where V_d is the unstressed volume of the ventricle and E_v is the elastance, which can be represented by various functions. One such function by Danielsen [28], shown in Figure 3.2, is given by

$$E_v(t) = E_{min}(1 - \phi(t)) + E_{max}\phi(t), \tag{3.7}$$

where

$$\phi(t) = \begin{cases} a_\phi \sin(\frac{\pi t}{t_{ce}}) - b_\pi \sin(\frac{2\pi t}{t_{ce}}) & \text{for} 0 \leq t_{ce}, \\ 0 & \text{for} t_{ce} \leq t \leq t_h. \end{cases} \tag{3.8}$$

Parameters E_{min} and E_{max} are minimal diastolic and maximal systolic values of ventricular elastance function, respectively, t_h is the heart period and t_{ce} the time for onset of constant elastance. The relation between heart period t_h and t_{ce} is given by

$$t_{ce} = K_0 + K_1 t_h, \tag{3.9}$$

where K_0 and K_1 are constant parameters. This model is simple with only three unknown parameters. Several researchers have used this model [27, 61, 97, 102, 118, 135, 140], affording several sources for model validation.

Another function for elastance based on the model by Suga et al. [54], but modified by Ellwein [34] is given as

$$E_v(t) = \begin{cases} \frac{E_{max} - E_{min}}{2}\left[1 - \cos\left(\frac{\pi t}{T_M}\right)\right] + E_{min}, & 0 \leq t \leq T_M \\ \frac{E_{max} - E_{min}}{2}\left[\cos\left(\frac{\pi(t - T_M)}{T_R}\right) + 1\right] + E_{min}, & T_M \leq t \leq T_M + T_R \\ E_{min}, & T_M + T_R \leq t \leq T \end{cases} \tag{3.10}$$

where parameters T_M, and T_R are the time for maximum (systolic) elastance, and remaining time to relaxation, respectively. These can be expressed as fraction of the length of the cardiac cycle T(s), thus allowing for a variable heart rate H. This function is simple, easy to implement, and most importantly smooth so as to be used with parameter estimation techniques. Furthermore, a change in contractility of the heart, i.e. during cardiovascular regulation, could be represented by a change in parameters representing the maximum elastance or the timing of the elastance function. This elastance time-varying function is shown in Figure 3.2.

Another approach for modeling the pumping of the heart proposed by Danielsen and Otte-sen [26, 107] that originates from a model developed by Mulier [96] given by

$$p_v(V_v, t) = a(V_v - b)^2 + (cV_v - d)f(t), \tag{3.11}$$

26
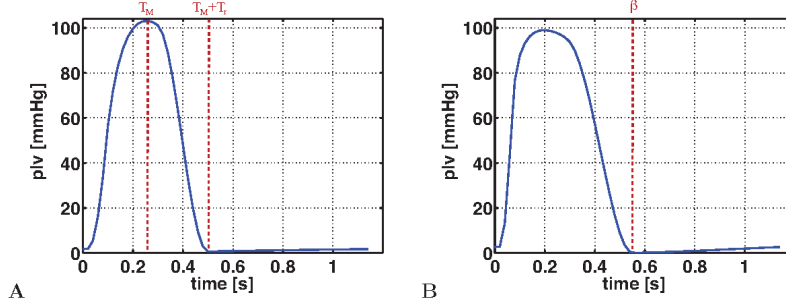
Figure 3.2: Ventricular pressure modeled using (A) the time-varying elastance (3.10); and (B) Muiler's isovolumic model (3.11).

where p_v is ventricular isovolumic pressure, $a(V_v - b)^2$ and $cV_v - d$ are the diastolic and systolic components of pressure, respectively. The parameter a represents the ventricular elastance during relaxation and b represents the ventricular volume at zero diastolic pressure. The parameters c and d relate to the volume dependent (contractility) and volume independent components, respectively. The function $f(t)$ is the normalization of g defined as

$$
f(t) = \begin{cases}
\dfrac{1 - e^{-\left(\frac{t}{\tau_c}\right)^\alpha}}{\left(1 - e^{-\left(\frac{t_p}{\tau_c}\right)^\alpha}\right) e^{-\left(\frac{t_p - t_b}{\tau_r}\right)^\alpha}}, & 0 \le t \le t_b, \\[3ex]
\dfrac{1 - e^{-\left(\frac{t}{\tau_c}\right)^\alpha} e^{-\left(\frac{t - t_b}{\tau_r}\right)^\alpha}}{\left(1 - e^{-\left(\frac{t_p}{\tau_c}\right)^\alpha}\right) e^{-\left(\frac{t_p - t_b}{\tau_r}\right)^\alpha}}, & t_b < t < t_h.
\end{cases}
$$

(3.12)

where the time constants τ_c and τ_r characterize the contraction and relaxation process, respectively, while α is a measure of the overall rate of onset of these processes. The constant t_b is the time when the relaxation process begins to evolve and is given by

$$
t_b = t_p \left\{ 1 - \left(\frac{\tau_r}{\tau_c}\right)^{\frac{\alpha}{\alpha-1}} \left[\frac{e^{-\left(\frac{t_p}{\tau_r}\right)^\alpha}}{1 - e^{-\left(\frac{t_p}{\tau_c}\right)^\alpha}} \right]^{\frac{1}{\alpha-1}} \right\}.
$$

(3.13)

This method was based on the Frank-Starling mechanism and involved a function that could increase pressure through cardiac muscle contractions without injection-induced volume decrease (i.e. isovolumic heart). Further details can be found in Muiler [96]. The model is depicted in Figure 3.2. Although, this is not the actual behavior of a pumping heart, it has been shown that this function does mimic both isovolumic and ejecting properties of the heart throughout the cardiac cycle when it is used with a cardiovascular system model [26, 107]. However, this

method does not allow the ventricular pressure to return to diastolic pressure and there is no definite end to the contraction.

The left heart function not only needs to describe the pressure in the left atrium and ventricle, but also the control of flow between the heart and the surrounding vessels. The human heart uses valves to direct and restrict blood flow as described in Section 2.1.1. This movement of the valves introduces semi-discrete behavior into the model (diode), since the flow out of the heart is either negligible (when the valve is closed) or a non-zero function of the pressure drop between the heart and the aorta. An approach used for modeling the succession of opening and closing of the valves as a resistance that varies with pressure was introduced by Rideout [118] and later used by Olufsen et al. [93]. This is done using a small baseline resistance to define the "open" valve and a resistance that is several orders of magnitude larger to define the "closed" valve. The resistance of a valve is then defined by the smooth sigmoidal function

$$R_{valve} = R_{valve,closed} - \frac{R_{valve,closed} - R_{valve,open}}{1 + e^{-\beta(p_{in} - p_{out})}}, \tag{3.14}$$

where p_{in} and p_{out} denote the pressures in compartments on either side of the valve and β describes the speed of the transition from open to closed. For $p_{in} > p_{out}$, $R_{valve} \rightarrow R_{valve,open}$ (the valve is open), and when $p_{out} > p_{in}$ the valve closes. Values in the exponent are chosen to ensure that the valve closes efficiently and that the flow is virtually zero while the valve is closed. It is important to note that this function is smooth to guarantee differentiability during gradient-based optimization.

Another method to account for the valves is including an "on-off switch" prompted by pressure changes. Olufsen et al. [91] uses this method where they set the closed switch value to zero and the open value to one, permitting the flow function to be stimulated. Nonetheless, the physical behavior of a valve is not discrete as this model depicts. Furthermore, the model is not smooth, which is not useful for parameter estimation analysis.

In work presented in this thesis, equations are developed using the information given in Section 3.1 with the exception of the inductance component. The cardiac model used in this work is from Ellwein given in 3.10, while the valves are modeled as in refeq:Rv.

Chapter 4

Model Analysis

Physiological models that are complex in nature, such as those discussed in the previous chapter frequently include an abundance of parameters. While physiological ideas can be used to establish values for some of these parameters, some parameters can only be estimated based on observations from experimental data, and several parameters cannot be determined at all. Models using nominal parameter values may produce intuition for the overall model dynamics and the behavior for a given group of patients, but since physiological components are known to vary substantially between individuals, such simulations cannot render patient specific knowledge.

The most rudimentary method for parameter identifiability is to manually adjust parameters to predict established or observed model outputs, see e.g., Kappel et al. [37], Spronck et al. [14], and Olufsen et al. [94]. This method may become unmanageable and may not provide optimal solutions for large models with numerous states and for multiple patient-specific subject studies. Nonlinear optimization techniques provide a more manageable approach for identifying parameters. These techniques estimate a set of model parameters that minimize the least squares residual between computed and measured quantities, i.e. solving the inverse problem. For example, Olufsen et al. [93] used the Nelder-Mead algorithm [101] to estimate parameters in a model developed to predict blood flow variations during postural change from sitting to standing. Although the model was developed to predict dynamics in individual subjects, this approach was done on only one subject due to the size of the model (11 differential equations and 111 parameters). In another study, Ellwein et al. [84] used a multi-step process involving gradient-based optimization for estimating patient-specific values for the 44 parameters given in 32 differential equations to predict cardiorespiratory response to hypercapnia for a patient with congestive heart failure. The estimation process took several hours for the one subject, a time frame not reasonable for clinical applications. In physiological studies, these techniques have mostly been used for simpler problems with a small number of parameters or for problems

where most of the internal states can be determined.

Complex nonlinear problems have an abundance of states and parameters, where many states are unobservable. These problems may use optimization techniques that give rise to solutions that are not unique and frequently result in numerical defects, since the differential equations may be stiff, contain delays, or be ill-posed. Hence, the use of numerical optimization techniques compel necessary scrutiny. Any given set of optimal parameters only represent a local solution to the minimization problem. Parameters that determine this local minimum may or may not be within physiological range, and there may be several sets of parameters that characterize the same model states. Therefore, it is important to compute nominal (initial) parameter values using *a priori* information such as the subject's height and weight, details from literature, or experimental data [34]. Furthermore, the solution can be insensitive to some of the model parameters, i.e., a small change in some parameters may give rise to essentially no change in the output states. Also, if the insensitive parameters are physiologically important, additional experiments may be required to estimate these parameters. Moreover, model parameters that are sensitive may be correlated. For example, two resistances may run parallel to one another in the circuit model and thus both parameters will be sensitive to the model, but only one can be identified. To this end, sensitivity analysis and subset selection are used as methods for estimating vital parameters given limited experimental data.

Sensitivity analysis methods can be devised either using a deterministic or stochastic approach, investigating global or local behavior. Our model contains only deterministic components, hence we disregard the stochastic approaches. Furthermore, examining only local behavior is appropriate since we begin with knowledge about each of our nominal parameters close to where we want to know our model behavior. This analysis has not been used substantially for the investigation of physiological models to our knowledge. A previous study by Wu et al. [147], compared local sensitivity analysis approaches using a direct method involving partial derivatives and an automatic approach to compute derivatives to understand what parameters had the largest impact on biological models with time-delays. Another study by Glover and Levan [48] uses local sensitivity analysis to parameterize models of adsorption bed behavior including fixed-bed adsorbers for solvent recovery. Morio [89] discusses both local and global methods used for a simple physical system.

In a physiological study, Olansen et al. [65] used invasive pressure measurements from dogs along with sensitivity analysis and a nonlinear least-squares optimization method to parameterize a cardiopulmonary circulation model. However, in their study it was not clear how parameters were ranked. Classical sensitivity analysis [36, 44] is used to rank parameters according to sensitivity [99, 4]. We adopted a similar procedure as in [34] where we use the sensitivity ranking results to shorten the parameter identification computational time and simplify the model. This ranking was used to separate parameters into two groups: sensitive and insensitive.

We also attempt to identify dependencies between parameters in the models using methods from Olufsen and Ottesen [104]. Parameter interdependencies can cause issues with numerical optimizers due to near singularities of the Jacobian matrix used in gradient-based optimization. Several combinations of parameters leading to the same solution may inhibit the optimization method from settling on an optimal parameter set.

The general equations for calculating nominal values for model parameters is presented in Section 4.1. The least squares optimization method is discussed in Section 4.2. Section 4.3 discusses the method used for sensitivity analysis. Two classes of subset selection and their use in these studies are given in Section 4.4. Finally, in Section 4.5 we present the optimal control method used to render quantities time-varying in Chapter 7.

4.1 Nominal parameter values

Literature values were used in conjunction with subject specific information to determine nominal values for all model parameters (resistances, compliances, cardiac, and HUT parameters), as well as to predict initial conditions for all state variables. Nominal parameter values were obtained by considering mean values for all pressures, flows, and volumes in the system obtained while the subject was in supine position (before HUT). The mean pressure in the upper arteries, $\bar{p}_{au}$, was estimated from data as the average pressure over the "steady" portion of the pressure-time series (in supine position). The resistance between any large arteries in the body is small (in supine position), thus the mean pressure in the lower arteries, $\bar{p}_{al}$, was estimated as 98 percent of $\bar{p}_{au}$. The same applies to the resistance between upper and lower body veins, consequently we set the upper body venous pressure $\bar{p}_{vu} = 3.5$ [80], while the mean pressure in the lower body veins, $\bar{p}_{vl} = 3.75$ [80].

Values for the total blood volume V_{tot} (ml) can be estimated using a number of formulas that are functions of height, weight, and/or body surface area [5, 57, 60, 90]. In the studies in the subsequent chapters, blood volumes within each compartment were obtained as fractions of the total blood volume, which for healthy subjects, were predicted from [128]

$$V_{tot} = \begin{cases} (3.47 \cdot \text{BSA} - 1.954)\,1000, & \text{Female} \\ (3.29 \cdot \text{BSA} - 1.229)\,1000, & \text{Male} \end{cases} \tag{4.1}$$

where $\text{BSA} = \sqrt{l\,w/3600}$ denotes the body surface area, l (cm) denotes the height and w (kg) the weight of the subject studied. The total volumetric blood flow, or cardiac output (CO), was estimated from the assumption that the total blood volume is circulated in the body within one minute [34], $\text{CO} = V_{tot}/60$ (ml/s). Alternative estimates for cardiac output could be derived based on measurements of arterial blood pressure as discussed in recent studies by [70]. The disadvantage of these studies is that their models must be validated against actual cardiac

output measurements.

Average flows between the upper and lower body, were estimated utilizing the assumption, that for a subject in supine position 90% of the blood flows between upper body arteries and veins, while 10% of the blood flow supports the vasculature in the lower extremities [30]. Several studies provide information on blood flow to the different regions of the body, e.g. [18, 30, 87]. For our studies, blood volume and blood flow distributions are taken from Beneken and DeWit [30], where they are given by organ and volumes are expressed as both stressed volume (the blood volume which generates the intravascular pressure) and unstressed volume (the blood volume necessary to fill the blood vessels without generating an intravascular pressure). Total volume can be given by the sum of the stressed and unstressed volumes, $V_{tot} = V_{str} + V_{unstr}$. Table 2.1 gives these volumes and percentages for an individual with a total blood volume of 4544 ml. These values are scaled according to the subject being studied. The values from Beneken and Dewit are scaled using the subject's blood volume to estimate average blood flow rates $\bar{q}_i$ for each compartment.

Utilizing estimates for blood flow, pressure and volumes, nominal values for model resistors and compliances can be found by rewriting the Ohm's law (3.1) and the pressure-volume (3.2) relations as

$$
\begin{aligned}
R &= \frac{\bar{p}_{in} - \bar{p}_{out}}{\bar{q}}, \\
C &= \frac{\bar{V} - \bar{V}_{unstr}}{\bar{p}} = \frac{V_{str}}{\bar{p}},
\end{aligned}
$$

where $\bar{p}, \bar{q}, \bar{V}$ denote mean values for the respective blood pressures, flow, and volumes.

For the heart model, parameters representing minimum and maximum elastance as well as timing of the pump function must be estimated. The minimum left ventricular elastance can be obtained from the pressure-volume relation (3.2), noting that when the left ventricular volume equals the end-diastolic volume (V_{ED}) we have

$$
\bar{p}_{pv} = E_{min} (V_{ED} - V_{lh,un}),
$$

where $\bar{p}_{pv}$ denotes the pulmonary venous pressure. This pressure is not appearing elsewhere in the model. We assumed that pulmonary venous pressure is slightly higher (4 mmHg) than its systemic counter-part [51, 136]. Similarly, the maximum left ventricular elastance can be predicted by assessing the same relation at the end-systolic phase. For this case

$$
p_{lh,sys} = E_{max} (V_{ES} - V_{lh,un}),
$$

where $p_{lh,sys}$ denotes the maximal systemic arterial pressure (obtained from the data) and V_{ES}

Table 4.1: Model parameters: The nominal parameter values and equations used for predicting them. $\bar{p}_{au}$ includes data from the supine portion of the blood pressure (bp) time-series ($t < 180s$), and N denotes the number of points within this period. $\overline{p}_{au,sys}$ includes the systolic blood pressure values for the M periods found for $t < 180$. Values for venous blood pressure are from [1].

Name	Definition	Equation	Value	Units
V_{tot}	total blood volume	Eqn (5.10)	5377 ± 549	ml
l	height		183 ± 8	cm
w	weight		80 ± 10	kg
CO	cardiac output	$V_{tot}/60$	90 ± 9	ml/s
$\bar{p}_{au}$	upper body mean arterial bp	$\dfrac{1}{N}\sum_{i=1}^{N} p_{au}(i)$	68 ± 11	mmHg
$\bar{p}_{al}$	lower body mean arterial bp	$0.98\ \bar{p}_{au}$	67 ± 11	mmHg
$\bar{p}_{vu}$	upper body mean venous bp		3.5	mmHg
$\bar{p}_{vl}$	lower body mean venous bp		3.75	mmHg
$\bar{q}_{up}$	upper body flow	0.9 CO	81 ± 8	ml/s
$\bar{q}_{low}$	lower body flow	0.1 CO	9.0 ± 0.9	ml/s
$R_{i,op}$	small resistance, open valve		0.001	mmHg s/ml
$R_{i,cl}$	large resistance, closed valve		20	mmHg s/ml
R_{aup}	upper body peripheral resistance	$\dfrac{\bar{p}_{au} - \bar{p}_{vu}}{\bar{q}_{up}}$	0.81 ± 0.19	mmHg s/ml
R_{alp}	lower body peripheral resistance	$\dfrac{\bar{p}_{al} - \bar{p}_{vl}}{\bar{q}_{low}}$	7.1 ± 1.6	mmHg s/ml
R_{al}	upper body arterial resistance	$\dfrac{\bar{p}_{au} - \bar{p}_{al}}{\bar{q}_{low}}$	0.15 ± 0.03	mmHg s/ml
R_{vl}	lower body venous resistance	$\dfrac{\bar{p}_{vl} - \bar{p}_{vu}}{\bar{q}_{low}}$	0.028 ± 0.003	mmHg s/ml
C_{au}	upper body arterial compliance	$0.19\ \bar{V}_{au}/\bar{p}_{au}$	1.7 ± 0.4	ml/mmHg
C_{al}	lower body arterial compliance	$0.05\ \bar{V}_{al}/\bar{p}_{al}$	0.26 ± 0.06	ml/mmHg
C_{vu}	upper body venous compliance	$0.05\ \bar{V}_{vu}/\bar{p}_{vu}$	51 ± 5	ml/mmHg
C_{vl}	lower body venous compliance	$0.16\ \bar{V}_{vl}/\bar{p}_{vl}$	4.3 ± 0.4	ml/mmHg
$\bar{p}_{pv}$	mean pulmonary venous bp		4	mmHg
$\bar{p}_{lh,sys}$	mean max systemic arterial bp	$\dfrac{1}{M}\sum_{i=1}^{M} p_{au,sys}(i)$	102 ± 13	mmHg
V_{ED}	end-diastolic volume		125	ml
V_{ES}	end-systolic volume		70	ml
$V_{lh,un}$	unstressed ventricular volume		10	ml
E_{min}	min elastance	$\dfrac{\bar{p}_{pv}}{V_{ED} - V_{lh,un}}$	0.03	mmHg/ml
E_{max}	max elastance	$\dfrac{\bar{p}_{lh,sys}}{V_{ES} - V_{lh,un}}$	1.7 ± 0.2	mmHg/ml
T_R	max elastance to relaxation	0.18/T	0.20 ± 0.01	N.D.
T_M	time of max elastance	data	0.11 ± 0.01	N.D.
T	length of ith cardiac cycle	data	0.90 ± 0.07	s
S	mean left heart contractility		15.3034	mmHg
α	contractility parameter		0.0013006	sec^{-2}
β	contractility parameter		0.01985	mmHg/sec
γ	contractility parameter		0.0149367	sec^{-1}
c	contractility parameter		6	N.D.

denotes the end systolic volume. For both parameters we assumed that the unstressed value of the ventricular volume $V_{lh,unstr} = 10$ ml, which was used in previous studies, e.g. [34]. The nominal value for the contractility of the left heart, S, and parameters associated with S (α, β, γ) used in Chapters 6 and 7 come from Batzel et al. [66].

The timing of the pump is achieved via parameters T_M, T_R and T. For this study we estimated T_M from data (for each cardiac cycle we let T_M be the time at which the pressure wave reached its maximum, while T_R was defined relative to the length of the cardiac cycle as $T_R = 0.19/T$ [34],[107]. Table 4.1 specifies parameter values for all model parameters.

Initial values for all differential equations, i.e., for all arterial and venous pressures, as well as the left ventricular volume were set as average values predicted as described above. These values can be found in Table 4.1 along with values for all nominal parameters. In general, model parameters are assembled into a vector which we denote as θ, the components of which are denoted by θ_k . The pressures and volumes comprise the states of the model, denoted by x_j and written together as the vector x. Physiological data, or observations, are denoted as y, and may represent one state or a combination of states in the model. With these monikers we set up the computational elements of the parameter estimation problem.

4.2 Least squares optimization

The models can be described by a system of coupled nonlinear ODEs as discussed in Chapter 3 that may be written as

$$\frac{dx}{dt} = F(x, t; \theta), \tag{4.2}$$

where $F : \mathbb{R}^{1+n+q} \to \mathbb{R}^n$, $x \in \mathbb{R}^n$ denotes the state vector, $t \in \mathbb{R}$ demotes time, and $\theta \in \mathbb{R}^q$ denotes the parameter vector. Corresponding to the available data, we assume an output vector $y \in \mathbb{R}^m$ associated with the states. It is assumed that this output can be computed as a function of the states, time and the model parameters, i.e.

$$y = g(x, t; \theta), \tag{4.3}$$

where $g : \mathbb{R}^{1+n+q} \to \mathbb{R}^m$. It is assumed that for each component of the model output y, there is an associated set of data D sampled at time t_i. To solve the inverse problem we assume that the data and corresponding model outputs can be evaluated at times where the data are sampled [104]. These are given by

$$D = (D_1(t_{11}), D_1(t_{12}), \ldots, D_1(t_{1k_1}), \ldots, D_m(t_{m1}), D_m(t_{m2}), \ldots, D_m(t_{mk_m}))^T, \tag{4.4}$$

$$y = (y_1(t_{11}), y_1(t_{12}), \ldots, y_1(t_{1k_1}), \ldots, y_m(t_{m1}), y_m(t_{m2}), \ldots, y_m(t_{mk_m}))^T, \qquad (4.5)$$

where D_i and y_i denote the ith component of the vectors D and y, respectively, $i = 1, \ldots, m$, and k denotes the sampling points for each component in the output vector.

Nonlinear optimization was utilized to estimate a set of model parameters that minimize the least squares error between the measured data and the model. This formulation relies on the assumption that the measurements, D_i, can be described fully by the underlying model output, y_i, plus an error term, ϵ_i, representing the measurement noise, i.e., we assume that

$$D_i = y_i + \epsilon_i, \quad i = 1, 2, \ldots, m. \qquad (4.6)$$

To satisfy the statistical model we assume that the errors ϵ_i are independent identically distributed (iid) random variables with mean $E[\epsilon_i] = 0$, covariance $\text{cov}(\epsilon_i, \epsilon_j) = 0$, and constant variance $\text{var}[\epsilon_i] = \mu^2$ [24, 59]. Given this form of the statistical model, the least squares error j is given by

$$J(\theta) = R^T R = \frac{1}{k - q} \sum_{i=1}^{m} |y_i - D_i|^2, \qquad (4.7)$$

where $R = (r_1, r_2, \ldots, r_k)^T$ with $r_i = (y_i - D_i)/\sqrt{k - q}$ is the model residual for the ith observation and q is the number of parameters.

A gradient-based local optimizer, specifically the Levenberg-Marquardt algorithm [75] is utilized to estimate parameters. Gradient-based optimization is useful if the cost function is easily differentiable and if we have knowledge of our system. This method uses the gradient of the cost function to determine where the cost is at a minimum instead of using a derivative-free algorithm such as the direct-search algorithm, Nelder Mead [101]. Levenberg-Marquardt is of benefit when we start far from the minimizer. That is, the theory supporting this method predicts rapid convergence when the initial parameter estimates are near the solution, and satisfactory convergence when they are far away from the solution.

4.3   Sensitivity analysis

The first step in identifying a subset of parameters to be estimated given available data, is to conduct sensitivity analysis and rank parameters from the most to the least sensitive. To perform sensitivity analysis on the models, we start with considerable knowledge about each of our nominal parameters, near which we want to know the behavior of our models. The analysis described by Eslami [36] and Frank [44] is used to derive sensitivity equations for the system equations (4.2). The dynamic sensitivity matrix, S, expresses the sensitivity of the model output

y to the model parameters, θ and is defined as

$$
S = \frac{\partial y}{\partial \theta} = \begin{pmatrix} \partial y_1/\partial \theta_1(t_{11}) & \ldots & \partial y_1/\partial \theta_q(t_{11}) \\ \vdots & \vdots & \vdots \\ \partial y_1/\partial \theta_1(t_{1k_1}) & \ldots & \partial y_1/\partial \theta_q(t_{1k_1}) \\ \vdots & \vdots & \vdots \\ \partial y_m/\partial \theta_1(t_{m1}) & \ldots & \partial y_1/\partial \theta_q(t_{m1}) \\ \vdots & \vdots & \vdots \\ \partial y_m/\partial \theta_1(t_{mk_m}) & \ldots & \partial y_1/\partial \theta_q(t_{mk_m}) \end{pmatrix}, \tag{4.8}
$$

For a given θ_i and y_i, sensitivities S_i, $i = 1, \ldots, q$ (represented by columns in matrix (4.8)) indicate how sensitive the model output is to a given value of the ith parameter at the times of measurements. Since model output and parameter units vary, it is beneficial to compute relative sensitivities defined as

$$
\tilde{S} = \frac{\partial y}{\partial \theta} \frac{\theta}{y}, \quad y \neq 0. \tag{4.9}
$$

Sensitivities can be computed analytically [24], using automatic differentiation [34], or by using finite differences [131]. Computing them analytically can be laborious and susceptible to errors for large systems. Automatic differentiation [42] uses operators that calculate exact derivatives to machine precision. Thus, it is the most accurate method for computing sensitivities, however computation time is lengthy and too slow for use with the gradient-based optimization algorithms. In our work we chose to derive sensitivities using finite differences. This method is simple to implement, cheap and gives a numerical approximation to the derivatives within an increment δ defined by the user. We used the forward difference approximation

$$
\frac{\partial y_k}{\partial \theta_i} = \frac{y_k(t, \theta + \delta e_i) - y_k(t, \theta)}{\delta}, \tag{4.10}
$$

where $e_i = [0 \ \ldots \ 0 \ \overset{i}{\hat{1}} \ 0 \ \ldots]^T$ is the unit vector in the i'th component direction, and $\delta = \sqrt{\chi}$ is the step-size where $\chi = 10^{-8}$ is the integration tolerance used for solution of the dynamical system. A scaled 2-norm, as described in [104], is used to get the total sensitivity, $\bar{S}_i$, to the ith parameter

$$
\bar{S}_i = ||S_i||_2 = \left(\frac{1}{K} \sum_{j=1}^{K} S_{i,j}^2 \right)^{1/2}. \tag{4.11}
$$

The resulting ranked sensitivities can be sorted from the most to least sensitive, thus parameters may be divided into two groups: ρ sensitive and $q - \rho$ insensitive parameters. Insensitive

parameters are not to be estimated, hence, the subset of identifiable parameters is decreased to only the sensitive parameters. Olufsen et al. [104] analyzed the computational accuracy of dividing the parameters into sensitive and insensitive. Since the differential equations are solved numerically with an absolute error $\mathcal{O}(10^{-\nu})$ and sensitivities are computed using finite differences as done in our work, then the error of the sensitivities are $\mathcal{O}(10^{-\nu/2})$ [131]. Parameters with sensitivities smaller than this bound are included in the set of insensitive parameters. It should be noted that this analysis is local, i.e results depend on the actual nominal values of the parameters. Hence the better the initial estimates of the parameters, the more accurate the analysis. Consequently, we also employed an additional analysis, subset selection, to determine which parameters were identifiable.

4.4   Subset selection

There are two main identifiability analysis methodologies for nonlinear ODE models. They include structural identifiability analysis and practical identifiability analysis [52]. Structural identifiability techniques verify system identifiability by exploring the system structure (i.e., the model itself). There are two basic assumptions for which structural identifiability analysis rely: model structures are completely accurate and there are no measurement errors. However, these two assumptions are obviously not valid in practice. For instance, in biomedical research, both model uncertainty and measurement error are usually large. Thus, even when structural identifiability analysis advocates that model parameters can be uniquely identified, the estimates of model parameters may still be uncertain. Thus, it is necessary to assess whether structurally identifiable parameters can be estimated with sufficient accuracy from noisy data. This is so-called practical identifiability analysis. Note that structural identifiability analysis determines a theoretical ground for practical identifiability analysis. If the structural analysis advocates that a model is not theoretically identifiable, the practical analysis is not necessary since theoretical unindentifiability must imply practical unindentifiability. Thus, only theoretically identifiable models need further practical identifiability analysis, a few of which will be discussed in detail here.

In the studies in the subsequent chapters, two practical identifiability methods are explored to test the models for parameter correlations analyzed by Olufsen et. al [104]. The goal of practical identifiability is to predict a subset of parameters that can be identified given the model and available data. It is essential since only a limited amount of data is available for "real-world" models. The results from a subset selection is a set of identifiable parameters and a set of parameters that should remain constant at nominal parameter values during optimization. This differs from sensitivity analysis, which finds individual parameters to which the system is independently sensitive.

The first method, also discussed by Pope et al. [131], to determine identifiable parameters uses singular value decomposition of the sensitivity matrix S followed by QR factorization (SVD-QR). The sensitivity matrix defined in (4.8) was decomposed as $S = U\Sigma V^T$, where U is the left hand singular vector, Σ is a diagonal matrix containing the singular values σ_i of S, and V is the associated right hand singular vector. The number of identifiable parameter values can be found by predicting the numerical rank ρ of S by using the singular values. Given a tolerance ϵ, the numerical rank of the matrix is the largest k such that the singular values $\sigma_{n-k+1} > \epsilon\sigma_n$. For our study, similar to the sensitivity analysis, $\epsilon = \sqrt{\chi}$, the square root of the integration tolerance χ. Using ρ, the matrix of eigenvectors V can be written as $[V_\rho\ V_{n-\rho}]$.

The identifiable parameters, which are the parameters associated with the ρ eigenvalues that correspond to the highest eigenvectors are then found using QR-decomposition with column pivoting. It should be noted that the QR decomposition is not unique, but differ with the concrete implementation of the algorithm. However, for a given ρ the algorithm will return a set of ρ identifiable parameters. Independent of the exact algorithm, the subset is found by $V_\rho^T P = QR$, where Q is an orthogonal matrix, and the first ρ elements of R form an upper triangular matrix with diagonal elements in decreasing order. The permutation matrix P can be used to reorder the parameter vector $\hat{\theta} = P^T\theta$. Finally, the partition $\hat{\theta} = \{\hat{\theta}_\rho, \hat{\theta}_{n-\rho}\}$, where $\hat{\theta}_\rho$ contains the first ρ identifiable elements, while the vector $\hat{\theta}_{n-\rho}$ contains parameters that cannot be identified, thus these were kept at their nominal parameter values. The latter does introduce bias in the computations, but reduces the variance. At the same time estimation of only sensitive parameters make the estimation algorithm more robust ([31, 60]).

The second method used in our studies is based on structured analysis of correlations computed from the covariance matrix. This analysis gives parameter sets that are pair-wise correlated. We use the model Hessian [56] (a positive definite symmetric matrix also known as the Fisher information matrix [6] defined by $\mathcal{H} = S^T S$, where S is the sensitivity matrix defined in (4.8)). Using the model covariance matrix $C = \mathcal{H}^{-1}$, the correlation matrix c can be computed as

$$c_{i,j} = \frac{C_{i,j}}{\sqrt{C_{i,i}C_{j,j}}}. \tag{4.12}$$

The correlation matrix is symmetric with 1's in the diagonal. All off-diagonal elements have values between $-1 \leq c_{i,j} \leq 1$, values in the range $y \in [0.85, 0.95]$ indicate that parameters are correlated [104]. Moreover, it should be noted that all analysis methods presented here are local and only valid in a region close to the parameter values investigated, i.e., results may change as the parameters change. To ensure that optimized parameters were not correlated, this analysis along with the sensitivity analysis can be repeated for the optimized parameter values as well.

4.5 Optimal control problem

Optimal control is a topic that appears in many branches of mathematics and engineering. In aerospace engineering, it is used in various applications including trajectory optimization, altitude control, and vehicle guidance [115, 122, 126]. In mathematical biology, optimal control techniques are utilized in mathematical models predominately for treatment of disease (i.e. cancer and HIV). For example, Neilan and Lenhart [100] present an SEIR (Susceptible, Exposed, Infected, Recovered) model with control acting as a rate of vaccination and an optimal control problem formulated to include an isoperimetric constraint on the vaccine supply. The goal of the study was to minimize the number of infectious individuals and the overall cost of the vaccination over a specific number of years. Zarei et al. [57] consider a mathematical model of HIV dynamics that includes the effect of antiretroviral therapy. They perform analysis of optimal control regarding maximizing the CD4+ T-cell counts and minimizing both the viral load and cost of drugs. De Pillis and Radunskaya [114] presented an analysis of a mathematical model of tumor growth with an immune response and chemotherapy. They used optimal control to describe treatment protocols which have the potential to be more efficient than standard periodic protocols already in use.

An optimal control problem consists of a cost functional that is a function of state and control variables. It contains a set of differential equations that describe the paths of the control variables that minimize the cost functional [81]. The objective of a standard optimal control problem is to find a control function $u(t)$ to minimize a cost functional

$$J(u(t)) = \Phi(x(t_0), t_0, x(t_f), t_f) + \int_{t_0}^{t_f} L(x(t), u(t), t) \, dt \tag{4.13}$$

subject to the first-order dynamic constraints

$$\dot{x}(t) = f(x(t), u(t), t), \tag{4.14}$$

the boundary conditions

$$\phi(x(t_0), t_0, x(t_f), t_f) = 0, \tag{4.15}$$

and the inequality path constraints

$$C(x(t), u(t), t) \leq 0. \tag{4.16}$$

Here $x(t)$ is the state, t_0 is the initial time, and t_f is the terminal time. Furthermore, f defines the right-hand side of the dynamic constraints, C defines the path constraints, and ϕ defines the boundary conditions.

For illustration, we consider the following example from Lewis and Syrmos [81]. The example involves the control of temperature in a room where the goal is to heat the room using the least possible energy. The room temperature is modeled using Newton's law of cooling,

$$\dot{\theta}(t) = -a(\theta(t) - \theta_\alpha) + bu(t),$$

where $\theta(t)$ is the temperature in the room with respect to time, θ_α is a constant representing the ambient air temperature outside of the room, and $u(t)$ is the control representing the heat supply to the room. If we let $x(t) = \theta(t) - \theta_\alpha$, then the state equation becomes

$$\dot{x}(t) = -ax + bu. \tag{4.17}$$

where the constants a and b depend on the room insulation. The objective is to control the temperature to be around 10 at $t = t_f$ with the least supplied energy. Thus the cost functional is given by

$$J = \frac{1}{2}s(x(t_f) - 10)^2 + \frac{1}{2}\int_0^{t_f} u^2 \, dt \tag{4.18}$$

for some weight coefficient s.

If the control variable $u(t)$ is unconstrained, the necessary conditions for the optimal solution (x^*, u^*) are given in terms of the Hamiltonian, H,

$$H(x, u, \lambda, t) = L(x, u, t) + \lambda^T f(x, u, t).$$

The following equations, including the original dynamics and initial conditions represent necessary conditions for optimality known as the Euler-Lagrange equations. These equations are used to design the control $u(t)$ that minimizes the cost function using Pontryagin's principle,

$$
\begin{aligned}
\dot{x}* &= \partial H/\partial \lambda = f(x^*, u^*, t), \quad x^*(t_0) = x_0, \tag{4.19}\\
-\dot{\lambda}* &= \partial H/\partial x(x^*, u^*, \lambda^*, t),\\
0 &= \partial H/\partial u(x^*, u^*, \lambda^*, t),
\end{aligned}
$$

with transversality condition

$$(\Phi_x - \lambda)^T \Big|_{t_f} dx(t_f) + (\Phi_t + H)^T \Big|_{t_f} dt_f = 0. \tag{4.20}$$

However, if the control $u(t)$ is constrained to lie in an admissible region (e.g., in our case, the control is bounded above and below by some constants), the stationarity condition $\partial H/\partial u = 0$

is replaced with the more general condition

$$H(x^*, u^*, \lambda^*, t) \leq H(x^*, u, \lambda^*, t).$$

for all admissible controls $u(t)$ [81]. Also, note that in the transversality condition, since $dx(t_f)$ and dt_f are not independent, we cannot simply set the coefficients of those quantities to zero. If $dx(t_f) = 0$ (fixed final state) or $dt_f = 0$ (fixed final time), the transversality condition is simplified.

Considering the temperature control example from above, the Hamiltonian is

$$H = \frac{u^2}{2} + \lambda(-ax + bu). \tag{4.21}$$

The optimal control $u(t)$ is determined by solving:

$$\dot{x} = -ax + bu, \tag{4.22}$$

$$\dot{\lambda} = a\lambda, \tag{4.23}$$

$$0 = u + b\lambda. \tag{4.24}$$

From the stationarity condition (4.24), the optimal control is given by

$$u(t) = -b\lambda(t), \tag{4.25}$$

thus to determine $u^*(t)$ we need to only find the optimal costate $\lambda^*(t)$. Substituting (4.25) into (4.22) yields the state-costate equations

$$\dot{x} = -ax - b^2\lambda \tag{4.26}$$

$$\dot{\lambda} = a\lambda \tag{4.27}$$

In this example, the final time is fixed (i.e. $dt_f = 0$) and the final state is free (i.e. $dx(t_f)$ is free). Thus, from the transversality condition (4.20), we have

$$\lambda(t_f) = \left. \frac{\partial \Phi}{\partial x} \right|_{t_f} = s(x(t_f) - 10).$$

So the boundary condition of x and λ are specified at t_0 and t_f, respectively. This is so called the two-point boundary value (TPBV) problem. Assuming that $\lambda(t_f)$ is known, from the solution

of (4.27) we have

$$\lambda(t) = e^{-a(t_f - t)}\lambda(t_f).$$

Hence

$$\dot{x} = -ax - b^2\lambda(t_f)e^{-a(t_f - t)}$$

and solving the above ODE, we have

$$x(t) = x(0)e^{-at} - \frac{b^2}{a}\lambda(t_f)e^{-at_f}\sinh(at).$$

Now we have the second equation about $x(t_f)$ and $\lambda(t_f)$,

$$x(t_f) = x(0)e^{-at_f} - \frac{b^2}{a}\lambda(t_f)e^{-at_f}\sinh(at_f).$$

Assuming $x(0) = 0$, $\lambda(t_f)$ can be solved as

$$\lambda(t_f) = \frac{-10as}{a + sb^2 e^{-at_f}\sinh(aT)}.$$

Now the costate equation becomes

$$\lambda^*(t) = \frac{-10ase^{at}}{ae^{at_f} + sb^2\sinh(aT)}$$

and finally we obtain the optimal control

$$u^*(t) = \frac{-10abse^{at}}{ae^{at_f} + sb^2\sinh(aT)}.$$

TPBV problems are difficult to solve even for the simplest optimal control problems as illustrated in the given example. In most cases, we rely on numerical methods and optimal control software packages utilizing indirect and direct methods.

4.5.1 Indirect methods

As summarized by Betts, Garg, Stryk et al. and Rao [9, 15, 46, 144], indirect methods employ the calculus of variations and Pontryagin's principle to determine the first order necessary conditions for an optimal solution of the problem given in (4.13), thus transforming the optimal control problems into a Hamiltonian boundary-value problem (HBVP). The most common indirect methods are the indirect shooting method, indirect multiple-shooting method, and indirect collocation method.

The most basic indirect method is the shooting method [74, 81, 144]. Typically, an initial

guess is made of the unknown boundary conditions at one end of the interval. Using this guess, in addition to the known initial conditions, the Hamiltonian system Eq. (4.20) is integrated to the other end. Upon reaching the terminal time, the terminal conditions obtained from the numerical integration are compared to terminal conditions given in Eqs. (4.15) and (4.20). If the integrated terminal conditions digress from the known terminal conditions by more than a specified tolerance ϵ, the unknown initial conditions are modified and the process is repeated until the difference between the integrated terminal conditions and the required terminal conditions is less than some specified threshold.

While the shooting method is attractive due to its simplicity, it introduces significant numerical instabilities due to ill-conditioning of the Hamiltonian dynamics. It is particularly problematic when the time interval of interest is lengthy in comparison to the time-scales of the Hamiltonian system in a neighborhood of the optimal solution. To overcome the numerical issues, a modified method called the multiple-shooting method was developed [49, 81, 132]. In a multiple-shooting method, the time interval is divided into subintervals. The shooting method is then utilized over each subinterval with the initial values of the state and adjoint of the interior intervals being unknowns that need to be determined. This method introduces additional variables into the problem (i.e., the values of the state and adjoint at the interface points). Although size of the problem is increased due to the extra variables, the multiple-shooting method is an advancement over the standard shooting method because the sensitivity to errors in the unknown initial conditions is diminished because integration is performed over significantly smaller time intervals. However, even multiple-shooting can present problems if a sufficiently good guess of the co-state is not given.

In an indirect collocation method, the state and co-state are parameterized using piecewise polynomials as described with the direct collocation method below. The collocation procedure leads to a root-finding problem where the vector of unknown coefficients consists of the coefficients of the piecewise polynomial. This system of nonlinear equations is then solved using an appropriate root-finding technique.

4.5.2 Direct methods

In direct methods for solving optimal control problems, the continuous state and/or control functions of time and cost are approximated and the problem is transcribed into a finite-dimensional nonlinear programming problem (NLP). The NLP is solved using well developed algorithms and software [17, 110, 111, 117]. The direct methods have the advantage that the optimality conditions do not need to be derived, the initial guess does not to be highly accurate, a guess of the co-state is not necessary, and the problem can be reformulated fairly easily if needed. On the downside, direct methods are not as accurate as indirect methods due

to their basis on numerics rather than theory, they require more work to verify optimality, and many do not provide knowledge of the co-state. There are several direct methods that have been established, including the two earliest developed methods: direct shooting and direct multiple-shooting [19, 78, 148]. Both of these methods parameterize the control using a specified functional form and the dynamics are integrated using explicit numerical integration (e.g., a time-marching algorithm). However, these methods are computationally expensive as a result of the numerical integration and require a priori knowledge of the switching structure of path constraints. POST [47] and STOPM [5] are well-known computer software for direct shooting methods.

Another direct method is based on collocation where both the state and control are parameterized via a set of basis functions and a set of differential algebraic constraints are enforced at a finite number of collocation points. Unlike the shooting methods, this approach does not require a priori knowledge of path constraints and is less sensitive to the initial guess. In direct collocation methods, the time interval is divided into subintervals and a fixed polynomial is used for approximation in each subinterval. The convergence of the numerical discretization is achieved by increasing the number of subintervals. The most common discretization methods are: Runge-Kutta methods that use piecewise polynomials and orthogonal collocation methods that use orthogonal polynomials. Direct collocation leads to a sparse NLP with many of the constraint Jacobian entries as zero. Although sparsity in the NLP increases the computational efficiency, the convergence to the exact solution is at a polynomial rate and often a large number of subintervals are needed for accurate approximation of the solution. Some examples of direct collocation computer softwares are SOCS [16], OTIS [58], DIRCOL [143], DIDO [120] and GPOPS [11, 12].

A particular class of collocation methods called pseudo-spectral methods have been studied in recent years. In a pseudo-spectral method, the basis functions are generally Lagrange polynomials and the collocation points are obtained from Gaussian quadrature rules. These methods are based on spectral methods and generally have exponentially faster convergence rates that then the other methods mentioned for a small number of discretization points [46]. The three most commonly used sets of collocation points are Legendre-Gauss (LG), Legendre-Gauss-Lobatto (LGL), and Legendre-Gauss-Radau (LGR) points, leading to the Gauss pseudo-spectral method (GPM), Lobatto pseudo-spectral method (LPM), and the Radau pseudo-spectral method (RPM), respectively. All three sets of points are obtained from the roots of a Legendre polynomial and/or linear combinations of a Legendre polynomial and its derivatives [23]. There are defined on the domain (-1,1), however they differ significantly in that LG points include neither of the endpoints, the LGL points include both of the endpoints, and the LGR points include one of the endpoints.

Although direct methods have many advantages, most of them do not give any informa-

tion about the co-state. The co-state is important for verifying the optimality of the solution, mesh refinement, sensitivity analysis, and real time optimization [46]. Co-state estimates have recently been established for pseudo-spectral methods by relating the Karush-Kuhn-Tucker (KKT) conditions of the NLP to the continuous co-state dynamics as demonstrated by Seywald and Stryk [127, 142]. For the GPM and RPM, the KKT conditions are found to be exactly equivalent to the discretized form of the first-order necessary conditions of the optimal control problem. This is not true for the LPM, thus this property allows for a co-state estimate that is more accurate for GPM and LPM than the one obtained from the LPM. However, the GPM initial and final point is not achieved due to the dynamics not being collocated at the endpoints. Hence, the RPM seems the most reasonable collocation method to employ to solve an optimal control problem. In work discussed in Chapter 7, we utilize the optimal control software GPOPS, which employs the RPM.

4.5.3   GPOPS (General Pseudo-spectral Optimal Control Software)

GPOPS solves multiphase optimal control problems utilizing the Gauss Pseudo-spectral Method (GPM). All the following information comes from [11, 12]. Given a set of P phases, i.e. separate time intervals on which the problem is solved, (where $p \in (1, \ldots, P)$), the general cost function to be minimized is of the form

$$
J = \sum_{p=1}^{P} \left[\Phi^{(p)}(x^{(p)}(t_0), x^{(p)}(t_f), t_f^{(p)}; q^{(p)}) + \int_{t_0^{(p)}}^{t_f^{(p)}} \mathcal{L}^{(p)}(x^{(p)}(t), u^{(p)}(t); q^{(p)}) \, dt \right]
\tag{4.28}
$$

subject to the dynamic constraints

$$
\dot{x}^{(p)} = f^{(p)}(x^{(p)}, u^{(p)}, t; q^{(p)}),
\tag{4.29}
$$

the inequality path constraints

$$
C_{\min}^{(p)} \le C^{(p)}(x^{(p)}, u^{(p)}, t; q^{(p)}) \le C_{\max}^{(p)},
\tag{4.30}
$$

the boundary conditions

$$
\phi_{\min}^{(p)} \le \phi^{(p)}(x^{(p)}(t_0), t_0^{(p)}, x^{(p)}(t_f), t_f^{(p)}; q^{(p)}) \le \phi_{\max}^{(p)},
\tag{4.31}
$$

and the linkage constraints

$$L_{\min}^{(s)} \le L^{(s)}(x^{(p_l^{(s)})}(t_f), t_f^{(p_l^{(s)})}; q^{(p_l^{(s)})}, x^{(p_r^{(s)})}(t_0), t_f^{(p_r^{(s)})}; q^{(p_r^{(s)})}) \le L_{\max}^{(s)}, \begin{cases} p_l, p_r & \in [1, \dots, P], \\ s & = 1, \dots, L. \end{cases}$$
(4.32)

where $x^{(p)}(t) \in \mathcal{R}^{n_p}$, $u^{(p)}(t) \in \mathcal{R}^{m_p}$, $q^{(p)} \in \mathcal{R}^{q_p}$ and $t \in \mathcal{R}$ are the state, control, static parameters, and time in phase $p = [1, \dots, P]$, respectively, L is the number of pairs of phases to be linked, and $(p_l^{(s)}, p_r^{(s)}) \in [1, \dots, P], s = 1, \dots, L$, are the "left" and "right" phase numbers, respectively.

The discretization of the multi-phase optimal control problem is done via the the RPM. RPM is an orthogonal collocation method based on using global polynomial approximations to the dynamic equations at a set of Legendre-Gauss-Radau (LGR) collocation points. The theory of the RPM can be found in [11, 23, 46]; however, no knowledge of the RPM is required for using GPOPS. The optimality conditions of the nonlinear programming problem (NLP) are equivalent to the discretized optimality conditions of the continuous control problem. This feature is not prevalent in other pseudo-spectral methods.

GPOPS is organized as follows. For a complete review of the usefulness of GPOPS, see [11, 12]. Note that the user must specify the optimal control problem to be solved by writing MATLAB functions that define the following functions in each phase of the problem:

G1 the cost functional

G2 the right-hand side of the differential equations and the path constraints (i.e. the differential-algebraic equations)

G3 the boundary conditions (i.e. event conditions)

G4 the linkage constraints (i.e. how the phases are connected)

Moreover, the user must specify the lower and upper limits on every component of the following elements:

G5 initial and terminal time of the phase

G6 the state at the following points in time:

- at the beginning of the phase
- during the phase
- at the end of the phase

G7 the control

G8 the static parameters

G9 the path constraints

G10 the boundary conditions

G11 the phase duration (i.e. the total length of phase in time)

G12 the linkage constraints (i.e. phase-connect conditions)

Note that each of the functions must be defined for each phase of the problem. Our problem does not necessarily have all the components mentioned, i.e. we have only one phase thus there are not linkage constraints. GPOPS utilizes third party solver SNOPT (Sparse Nonlinear Optimizer) to solve the NLP problem.

SNOPT is a package for constrained optimization. It can be used to solve both linear and nonlinear functions subject to bounds on the variables and sparse linear or nonlinear constraints. It is applicable to large-scale linear and quadratic programming problems, linearly constrained optimization, and general nonlinear problems. It employs a unique sequential quadratic programming (SQP) algorithm [111] that exploits sparsity in the constraint Jacobian and maintains a limited-memory quasi-Newton approximation to the Hessian of the Lagrangian. The algorithm applies to constrained optimization problems of the form

$$\min_{x \in \mathcal{R}^n} f(x) \tag{4.33}$$

$$\text{subject to } l \leq \begin{pmatrix} x \\ c(x) \\ Ax \end{pmatrix} \leq u, \tag{4.34}$$

where $f(x)$ is a linear or nonlinear objective function, $c(x)$ is a vector of nonlinear constraint functions with sparse derivatives, A is a sparse matrix, and l and u are vectors of lower and upper bounds. It is assumed that the nonlinear functions are smooth and that their first derivatives are obtainable.

Search directions for the optimization problem are attained from quadratic programming sub-functions that minimize (or maximize) a quadratic model of the Lagrangian function subject to linearized constraints. The Lagrangian function is reduced along each search direction to guarantee convergence from any starting point. More information on SNOPT and SQP methods can be found in [111].

Chapter 5

Patient Specific Pulsatile Model of HUT

Abstract

Short term cardiovascular responses to head-up tilt (HUT) involve complex cardiovascular regulation in order to maintain blood pressure at homeostatic levels. This chapter presents a patient specific model that uses heart rate as an input to fit the dynamic changes in arterial blood pressure data during HUT. The model contains five compartments representing arteries and veins in the upper and lower body of the systemic circulation, as well as the left ventricle facilitating pumping of the heart. A physiologically based sub-model describes gravitational pooling of blood into the lower extremities during HUT, and a cardiovascular regulation model adjusts cardiac contractility and vascular resistance to the blood pressure changes. Nominal parameter values are computed from patient specific data and literature estimates. The model is rendered patient specific via the use of parameter estimation techniques. This process involves sensitivity analysis, prediction of a subset of identifiable parameters, and nonlinear optimization. The approach proposed here was applied to analysis of aortic and carotid HUT data from five healthy young subjects. Results showed that it is possible to identify a subset of model parameters that can be estimated allowing the model to fit changes in arterial blood pressure observed at the level of the carotid bifurcation. Moreover, the model estimates physiologically reasonable values for arterial and venous blood pressures, blood volumes, and cardiac output for which data are not available.

5.1 Introduction

The head-up tilt (HUT) test is often used to assess a patient's ability to regulate blood pressure [64, 88], in particular for patients suffering from frequent episodes of syncope, lightheadedness, or dizziness [88]. During this procedure quantities measured include non-invasive beat-to-beat recordings of arterial blood pressure and heart rate. The test starts with the patient placed on a tilt-table in supine position. After steady values for pressure and heart rate are obtained the table is tilted to an angle of 60-70 degrees.

Upon tilting, gravity causes pooling of 500-1000 ml of blood in the lower extremities reducing the venous return, cardiac filling, and cardiac output [64, 121]. The change of volume leads to a decrease of blood pressure in the upper body (above the center of gravity), while blood pressure in the lower body (below the center of gravity) is increased. During HUT the baroreceptors located in the carotid sinus sense the drop in blood pressure causing sympathetic activation and parasympathetic withdrawal. This in turn leads to an increase in heart rate, along with changes in cardiac contractility and vascular resistance [32, 51, 136]. For most people, the receptors located in the aortic arch sense an increase in pressure [64, 71], which in principle should cause a decrease in heart rate. This response is contradictory to observed heart rate increase. Thus we hypothesize that during HUT, the carotid sinus baroreceptors are the main receptors activated leading to the observed increase in heart rate. Consequently, models developed to analyze the dynamics of blood pressure regulation were compared with data measured at the level of the carotid sinus. However, in most tilt-table experiments blood pressure is measured at the level of the aortic arch. In this study, we use data from both locations. Figure 6.1(a) shows an example of blood pressure time series measured at the two locations. Data measured at the level of the carotid sinus are used directly, while data measured at the level of the aortic arch are first translated to the level of the carotid sinus. Figure 6.1(b) shows an example of measured and calculated carotid blood pressures.

The baroreflex system, described above, is the main contributor to the control engaged during HUT. However, other sensory systems also play a role in modulating the vascular targets including inputs from cardiopulmonary sensors, the vestibular system, the central command center, and the muscle sympathetic system [39, 124]. In this study, we do not directly model the afferents but focus on predicting the impact on the vascular targets: heart rate, cardiac contractility, and vascular resistance by allowing model parameters representing these quantities to vary in time. The time-varying parameters are embedded in a compartmental model including the left heart as well as arterial and venous compartments representing the upper (above the center of gravity) and lower (below the center of gravity) parts of the body. Heart rate and the time for end-systole are used as the model inputs, while systolic and diastolic arterial blood pressure in the upper body (representing pressure at the level of the carotid arteries) is the

model output. Parameter estimation techniques are used to render the model patient specific allowing the model to fit blood pressure dynamics observed at the level of the carotid arteries.

The paper is organized as follows: The methods are outlined in section 2. This section includes a description of the data (section 2.1); the cardiovascular model, and methods used for calculation of nominal parameter values and initial conditions (section 2.2); model analysis including a formulation of the optimization problem, sensitivity analysis, parameter identification, and methods used for nonlinear optimization (section 2.3). Results are presented in section 3, and we conclude with section 4 discussing our findings.

5.2   Methods

A large number of previous studies have analyzed cardiovascular regulation of heart rate from a medical, statistical, and modeling point of view. These studies can be separated in two groups: studies which analyze the system dynamics using signal processing techniques and studies that are based on mechanistic differential equations models. Signal processing based studies (e.g. [7, 33, 53, 150]) typically analyze the frequency and magnitude components of the measured signals. Mechanistic models investigate the system dynamics using techniques developed from physical laws. Such models are often used to describe dynamics for an average healthy subject, or to predict the impact of a given disease (e.g. [8, 10, 40, 72, 65, 79, 94, 106, 116, 118, 141]). While the signal processing techniques typically analyze actual signals from individual subjects, mechanistic models are most commonly developed to gain more insight into the system, i.e., they were not adapted to display individual dynamics. Patient specific models, which use mechanistic descriptions to predict signals recorded from individual subjects, can be obtained by combining a general mechanistic model with patient specific estimation of model parameters. Estimating model parameters involves solution of an inverse problem, i.e. given a model and data one has to estimate the model parameters [59]. This problem is in general difficult to solve, and typically, no unique analytical or numerical solution can be found [125].

One of the main obstacles in developing patient specific models, is that "good" physiologically models often have a large number of variables and parameters, while the number of quantities measured to render these models patient specific is sparse. Therefore, most studies addressing parameter identification and/or parameter estimation use examples involving a "correct" model, good initial parameter values, and a comprehensive set of data. For such systems, model parameters may be estimated via solution of the associated inverse problem [6]. However, in practice, only some parameters can be estimated given a model and available observations, and this process works better if the model analyzed is not too complex.

The overall objective is to build a simple model including only essential elements. Some studies have successfully developed patient specific models of the cardiovascular system, but

most of these models do not include pulsatility [55, 67, 85]. There are a few models that include pulsatility [93, 131], though the model by [93] estimated too many model parameters and the model by [131] only addressed how to estimate parameters for a subject in supine position. Other contributions include the study by [134] who developed a model predicting short term blood pressure and heart rate variability for a healthy young male, and studies by Ursino who modeled heart rate regulation [8, 138, 139]. The latter studies did compare the model output with experimental data but did not address parameter estimation. Another example, is the recent model by [129], which computes heart rate regulation in rats. This study does address parameter estimation, but does not address parameter identifiability.

The work discussed in this paper is a simple model that uses heart rate as input and estimates pulsatile arterial blood pressure during HUT. To make the model patient specific, we use sensitivity analysis and parameter identification combined with nonlinear optimization. The study shows how to estimate constant and time-varying parameters allowing the model fit data measured at the level of the carotid artery. Finally, we show how carotid pressure can be calculated from data measured at the level of aorta and that similar parameter estimates are obtained comparing model outputs against the measured and calculated carotid pressures.

5.2.1 Blood pressure and heart rate data

Data was collected at the Coordinating Research Centre at Frederiksberg Hospital, Copenhagen, Denmark from five fit healthy young male volunteers age 30 ± 4 who had no known heart or vascular diseases. The subjects gave informed consent to participate in the study, which was approved by the local internal review board at Frederiksberg Hospital, Denmark. After resting for 10 minutes in supine position, the subjects were tilted to an angle of 60 degrees at a speed of 15 degrees per second measured by way of an electronic marker. The subjects remained tilted for five minutes, and were then returned to supine position at the same tilt speed. For the model based analysis, we extracted a total of 290 seconds of data: including a 180 seconds segment recorded while the subjects were in supine position (see Fig. 5.1(e)) and a 180 second segment recorded during HUT (see Fig. 5.1(f)). This latter segment overlaps with the supine segment as illustrated on the figure.

Measurements include ECG recorded data using standard precordial leads and blood pressure recorded using photoplethysmography (Finapres Medical Systems B.V.). For pressure measurements, a sensor was placed on the index finger on each hand. The left hand was kept at the level of the aortic arch, which is at the same level as the mitral valve, while the right hand was kept at the level of the carotid sinus, which is at the same level as the carotid bifurcation. The location of the mitral valve and carotid bifurcation were determined by echocardiography and carotid ultrasound, respectively. ECG and blood pressure measurements were sampled contin-
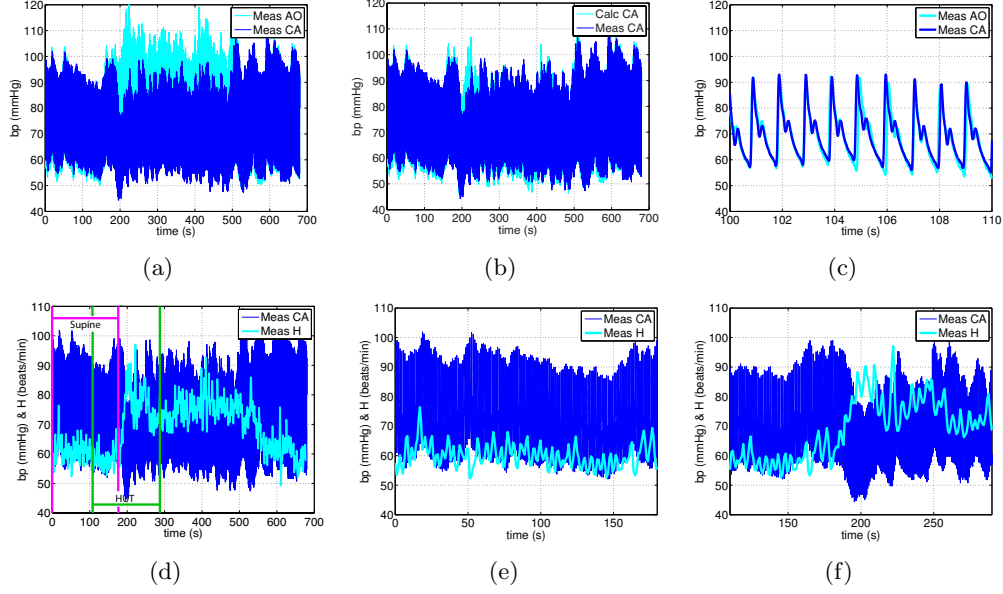
Figure 5.1: Graph (a) shows simultaneous measurements of aortic (cyan) and carotid (blue) blood pressures during HUT, (b) shows measured (blue) and calculated (cyan) carotid blood pressure, and (c) shows a zoom for $t = 100 - 110$ seconds. (d-f) show measured carotid blood pressure (blue) and heart rate (cyan) for the complete data set (d), for data used to estimate the dynamics in supine position (e) (marked with pink lines on (d)), and during HUT (f) (marked with green lines on (d)). Note, there is an overlap between the data shown in (e) and (f).

uously at a rate of 1.0 kHz and saved digitally using an A/D-converter communicating with a computer via Chart 5 (ADInstruments). This program allows extraction of heart rate from the ECG measurements. By keeping the fingers with sensors at the two locations, the measured pressures hydrostatically represents the actual pressures at the two locations. Diastolic values measured are similar to the central pressure values, though systolic values may be overestimated due to the impact of wave-reflection. Examples of peripheral and central wave-forms can be found in the book by [45]. Figure 5.1(a-c) show the two blood pressure time series for a representative subject, while Fig. 5.1(d-f) show heart rate and blood pressure time series measured at the level of the carotid arteries.

To estimate the blood pressure regulation in response to HUT, blood pressure should be measured at the level of the carotid sinus. However, many existing tilt-experiments have only measured blood pressure at the level of aorta. For an upright subject, the main difference between the two signals is the impact of hydrostatic pressure. Thus using a simple model involving gravity, it is possible to calculate the carotid pressure $p_{Ca,p}$ from the pressure measured at the

level of the aortic arch as

$$p_{Ca,p} = p_{Ao} - \rho g h, \qquad (5.1)$$

where p_{Ao} is the measured aortic blood pressure data, ρ (g/ml) is the density of blood, g (cm/s^2) is the constant of gravitational acceleration, and h (cm) is the height difference between the carotid sinus and the aortic arch. Figure 5.1(b) shows the true carotid data along with the calculated carotid data.

5.2.2   Mathematical model

This section describes the cardiovascular model developed to estimate blood flow, volume, and pressure in the systemic circulation during HUT. The model development is split into three parts including: a lumped cardiovascular model estimating dynamics while the subject is in supine position; a model estimating dynamic changes in response to HUT; and a model estimating the impact of cardiovascular regulation on the model parameters. Following the model descriptions, a section describing nominal parameter values and initial conditions used to solve the differential equations is included.

Lumped cardiovascular model

The basic cardiovascular model includes 5 compartments (see Fig. 5.2) representing arteries and veins in the upper and lower body of the systemic circulation, as well as the left heart. The upper body compartments include arteries and veins in the head, thorax, and abdomen, while the lower body compartments include all vessels in the legs. The model mimics an electrical RC-circuit with voltage analogous to pressure, current analogous to flow, charge analogous to volume, compliance analogous to capacitance, while resistance is the same in both formulations. This model is able to estimate pulsatile blood pressure and flow in the various compartments, while it cannot output the actual shape of the wave form.

For each compartment, a pressure-volume relation can be defined as

$$V_i - V_{un} = C_i(p_i - p_{ext}), \qquad (5.2)$$

where V_i (ml) is the compartment volume, V_{un} (ml) is the unstressed volume, C_i (ml/mmHg) is the compartment compliance, p_i (mmHg) is the compartment instantaneous blood pressure, and p_{ext} (mmHg) (assumed constant) is the pressure in the surrounding tissue. For each compartment, we also use a differential equation to predict the change in volume,

$$\frac{dV_i}{dt} = q_{in} - q_{out}. \qquad (5.3)$$
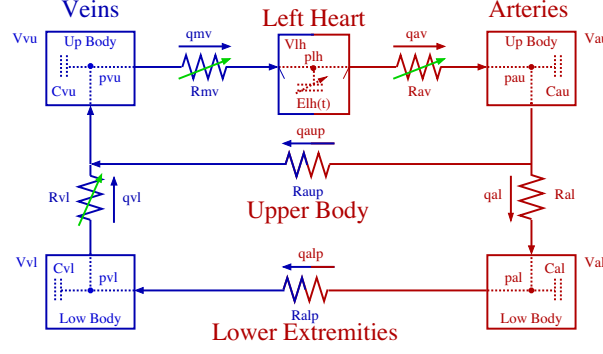
Figure 5.2: Compartment model used for predicting HUT dynamics. For each compartment an associated blood pressure p (mmHg), volume V (ml), and compliance C (ml/mmHg) are defined. The compartments represent the upper body arteries (subscript au), lower body arteries (subscript al), upper body veins (subscript vu), lower body veins (subscript vl), and the left heart (subscript lh). Resistances R (mmHg s/ml) are placed between all compartments: R_{al} denotes the resistance between arteries in the upper and lower body, R_{aup} and R_{alp} denote resistance between arteries and veins in the upper and lower body, respectively. The two heart valves, the mitral valve and the aortic valve, are modeled as pressure dependent resistors R_{mv} and R_{av}. Finally, the resistance between the lower and upper body veins R_{vl} is also modeled as pressure dependent to prevent retrograde flow into the lower-body during the HUT.

where q (ml/s) is the volumetric flow. Using a linear relationship analogous to Ohm's law the volumetric flow q (ml/s) between compartments can be computed as

$$q = \frac{p_{in} - p_{out}}{R}, \tag{5.4}$$

where p_{in} and p_{out} are the pressure on either side of the resistor R (mmHg s/ml). Differentiating (5.2), using (5.3), and inserting (5.4) allows us to obtain a system of differential equations in blood pressure of the form

$$\frac{dp_i}{dt} = \frac{1}{C_i}\frac{dV_i}{dt} = \frac{1}{C_i}\left(\frac{p_{i-1} - p_i}{R_{i-1}} - \frac{p_i - p_{i+1}}{R_i}\right),$$

where i refer to the compartment for which the pressure p_i is computed, while $i-1$ and $i+1$ refer to the two neighboring compartments. For resistances that appear between compartments, R_{i-1} refer to the resistance between compartments $i-1$ and i, and R_i refer to the resistance between compartments i and $i+1$. The latter equation is valid since we assume that C_i (ml/mmHg) is constant. This formulation is utilized for the four arterial and venous compartments.

For the left heart compartment, we also use (5.3). For this compartment, pressure is pre-
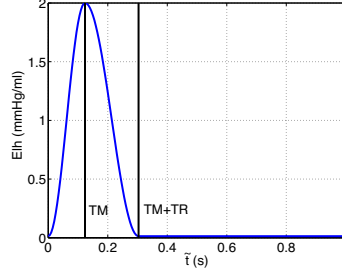
Figure 5.3: Time-varying elastance during a cardiac cycle. The maximum elastance is found at $\tilde{t} = T_M$ and the minimal elastance at $\tilde{t} = T_M + T_R$, while the length of the cardiac cycle $T = 1$ seconds. Values for T_M and $T = 1/H$ are obtained from data.

dicted from volume using the pressure-volume relation

$$p_{lh} = E_{lh}(V_{lh} - V_{un}), \tag{5.5}$$

where E_{lh} (mmHg/ml) is the left heart elastance (the reciprocal of its compliance) and V_{lh} is the left heart volume. Pumping is achieved by introducing a variable elastance function [34] of the form

$$E_{lh}(\tilde{t}) = \begin{cases} \dfrac{E_{max} - E_{min}}{2} \left[1 - \cos\left(\dfrac{\pi \tilde{t}}{T_M} \right) \right] + E_{min}, & 0 \leq \tilde{t} \leq T_M \\[4mm] \dfrac{E_{max} - E_{min}}{2} \left[\cos\left(\dfrac{\pi\left(\tilde{t} - T_M\right)}{T_R} \right) + 1 \right] + E_{min}, & T_M \leq \tilde{t} \leq T_M + T_R \\[4mm] E_{min}, & T_M + T_R \leq \tilde{t} \leq T \end{cases} \tag{5.6}$$

where $\tilde{t}$ is the time within a cardiac cycle $T = 1/H$. E_{min} and E_{max} denote the minimum and maximum elastance, respectively. For each cardiac cycle elastance is increased for $0 < \tilde{t} < T_M$ and decreased for $T_M < \tilde{t} < T_M + T_R$, while during diastole $T_M + T_R < \tilde{t} < T$ elastance is kept constant at its minimum value. Values for T and T_M are obtained from data, while T_R is a model parameter. The time-varying elastance function is illustrated in Fig. 5.3.

Finally, heart valves are modeled using pressure dependent resistors for which a large resistance R_{cl} represents a closed valve, while a small resistance R_{op} represents an open valve. These are modeled as smooth sigmoidal functions of the form

$$R_v = R_{cl} - \frac{R_{cl} - R_{op}}{1 + e^{-\beta(p_{in} - p_{out})}}, \tag{5.7}$$

where p_{in} and p_{out} denote the pressures in compartments on either side of the valve. For $p_{in} > p_{out}$, $R_v \to R_{op}$ (the valve is open), and when $p_{out} > p_{in}$ the valve closes.

Using these relations the five differential equations can be written as

$$\frac{dp_{au}}{dt} = (q_{av} - q_{al} - q_{aup})/C_{au},$$

$$\frac{dp_{al}}{dt} = (q_{al} - q_{alp})/C_{al},$$

$$\frac{dp_{vl}}{dt} = (q_{alp} - q_{vl})/C_{vl},$$

$$\frac{dp_{vu}}{dt} = (q_{aup} + q_{vl} - q_{mv})/C_{vu},$$

$$\frac{dV_{lh}}{dt} = q_{mv} - q_{av},$$

where

$$q_{av} = \frac{p_{lh} - p_{au}}{R_{av}},$$

$$q_{aup} = \frac{p_{au} - p_{vu}}{R_{aup}},$$

$$q_{al} = \frac{p_{au} - p_{al}}{R_{al}},$$

$$q_{alp} = \frac{p_{al} - p_{vl}}{R_{alp}},$$

$$q_{vl} = \frac{p_{vl} - p_{vu}}{R_{vl}},$$

$$q_{mv} = \frac{p_{vu} - p_{lh}}{R_{mv}}.$$

In the last set of equations the left ventricular pressure p_{lh} is predicted using (5.5), the pressure dependent resistances used to model the valves (R_{av}, R_{mv}) are predicted from (5.7), and the total blood volume can be computed from pressures using (5.2). These equations were solved in Matlab using the ODE15s differential equations solver. Abbreviations (subscripts) are given in Table 5.1.

Modeling HUT

The response to HUT is modeled by accounting for hydrostatic pressure acting on each compartment. During supine position, gravity does not influence the system. Upon HUT, blood is pooled in the lower extremities leading to an increase in pressure in the lower body, while pressure in the upper body decreases. To account for gravity, the pressure at the level of the carotid arteries were used as a reference pressure, so an extra term is added to the arterial lower body flow q_{al} and subtracted from the venous flow of the lower body compartments. Figure 5.4 shows the subject tilted at an angle $\theta = 60^o$. The quantity h_{tilt} (cm) represents the distance

between the lower and upper compartment. The gravitational effects are calculated as in [93], and the modified flow equations are given by

$$q = \frac{\rho g h_{tilt} \sin\left(\theta(t)\right) + p_{in} - p_{out}}{R},$$ (5.8)

$$\theta(t) = \frac{\pi}{180} \begin{cases} 0 & t < t_{st} \\ v_t(t - t_{st}) & t_{st} \leq t \leq t_{st} + t_{ed} \\ 60 & t > t_{st} + t_{ed} \end{cases}$$

where ρ (g/ml) is blood density, g (cm/s^2) is the constant of gravitational acceleration, h_{tilt} (cm) is the absolute height between the upper body and lower body compartments, $\theta(t)$ is the tilt angle (in radians), $v_t = 15$ degrees/s is the tilt speed, while t_{st} and t_{ed} denote the time at which HUT is started and ended, respectively. The combined term $\rho g h_{tilt} \sin\left(\theta(t)\right)$ denotes the hydrostatic pressure between the upper and lower body compartments.

Modeling effects of cardiovascular regulation

Upon HUT firing of the baroreceptor nerves are modulated by the aortic and carotid sinus baroreceptors sensing changes in the stretch of the arterial wall. Typically, HUT leads to a decrease in blood pressure mediating an increase in sympathetic outflow along with parasympathetic withdrawal. Sympathetic stimulation elicits changes in vascular resistance and cardiac contractility, while parasympathetic withdrawal primarily has an effect on heart rate (shown on Fig. 5.1) and cardiac contractility. Heart rate is used as an input, thus the parasympathetic heart rate regulation is implicitly accounted for in the model. Regulation of cardiac contractility is modeled by controlling the minimum elastance of the left heart E_{min}, while regulation of vascular resistance is included in the upper and lower body. The upper body compartment includes

Table 5.1: Abbreviations (subscripts) used in the compartmental model.

Abbreviation	Name
au	upper body arteries
al	lower body arteries
aup	upper body "peripheral" vascular bed
alp	lower body "peripheral" vascular bed
vu	upper body veins
vl	lower body veins
lh	the left heart (ventricle and atrium)
av	aortic valve
mv	aortic valve
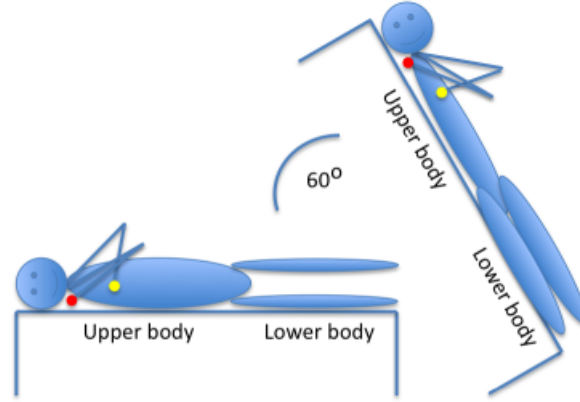
Figure 5.4: The HUT test: The subject depicted is tilted to an angle of 60 degrees at a constant speed of 15 degrees per second. Red and yellow circles indicate the locations for the blood pressure sensors. Each sensor is mounted on the index finger, one finger (red) is placed at the level of the carotid artery, while the other (yellow) is placed at the level of the heart. Upon HUT blood is pooled in the lower extremities.

abdominal and intestinal vessels, while the lower body compartment lumps vessels in the lower extremities. Consequently, both R_{aup} and R_{alp} (see Fig. 5.2) have been regulated. However, as the compartments representing the upper and lower body arteries appear in parallel, both resistances are not identifiable, thus we controlled R_{aup} directly, while we let $R_{alp} = kR_{aup}$, where k is the ratio of the optimized supine values of R_{aup} and R_{alp}.

Two quantities R_{aup} and E_{min}, were controlled to counteract the effect of the tilt. We modeled the control by defining the controlled quantities using piecewise linear functions of time given by

$$X(t) \quad = \quad \sum_{i=1}^{N} \gamma_i H_i(t), \qquad\qquad (5.9)$$

$$H_i(t) \quad = \quad \begin{cases} \dfrac{t - t_{i-1}}{t_i - t_{i-1}}, & t_{i-1} \leq t \leq t_i \\ \dfrac{t_{i+1} - t}{t_{i+1} - t_i} & t_i \leq t \leq t_{i+1} \\ 0, & \text{otherwise,} \end{cases}$$

where the unknown coefficients γ_i, $i = 1 \dots N$ are the new parameters that will be estimated to estimate the control, and N is the number of nodes along the time span analyzed. The spread of the N nodes should be specified in the model. For simulations reflecting dynamics observed in supine position we placed N with a frequency of 6-10 seconds, but during HUT, where dynamics change, significantly more points were added. It should be noted that the more

58

points are added to the time-span, the longer the simulations.

Nominal parameter values

Literature values and subject specific information were integrated to identify nominal values for all model parameters (resistances, capacitors, heart, and HUT parameters) as well as to predict initial conditions for all state variables. Nominal parameter values were obtained by considering mean values for all pressures, flows, and volumes in the system obtained while the subject was in supine position (before HUT). The mean pressure in the upper arteries, $\bar{p}_{au}$, was estimated from data as the average pressure over the "steady" portion of the pressure-time series (in supine position). The resistance between any large arteries in the body is small (in supine position), thus the mean pressure in the lower arteries, $\bar{p}_{al}$, was estimated as 98 percent of $\bar{p}_{au}$. The same applies to the resistance between upper and lower body veins, consequently we set the upper body venous pressure $\bar{p}_{vu} = 3.5$, while the mean pressure in the lower body veins, $\bar{p}_{vl} = 3.75$. Values for the total blood volume within each compartment were obtained as fractions of the total blood volume, which for healthy subjects, can be predicted from [128]

$$V_{tot} = \begin{cases} (3.47 \cdot \text{BSA} - 1.954)\,1000, & \text{Female} \\ (3.29 \cdot \text{BSA} - 1.229)\,1000, & \text{Male} \end{cases} \tag{5.10}$$

where $\text{BSA} = \sqrt{l\,w/3600}$ denotes the body surface area, l (cm) denotes the height and w (kg) the weight of the subject studied. For each compartment, we used stressed and unstressed blood volume as proposed by [30]. Values of stressed blood volume are given in Table 5.2.

Table 5.2: For each compartment volume is estimated as fractions of the total volume V_{tot}, and the total compartment blood volume is separated between a stressed and an unstressed volume, i.e., $V_{tot,i} = V_{str,i} + V_{un,i}$. This table lists stressed volumes calculated as a fraction of the total volume. Values are computed using ideas proposed by [30]. In this study the upper body compartments contain arteries and veins in the head, thorax, and abdomen, while the lower body compartments contain arteries and veins in the legs.

Volume	Position	Fraction of Total Volume	Fraction of Stressed Volume
V_{au}	Upper body arteries	0.11	0.19
V_{al}	Lower body arteries	0.66	0.05
V_{vu}	Upper body veins	0.02	0.16
V_{vl}	Lower body veins	0.06	0.05

Cardiac output was estimated from the assumption that the entire volume is circulated in the body within one minute [34]. Alternative estimates for cardiac output could be derived as discussed in recent studies by [70]. Average flows between the upper and lower body, were estimated utilizing the assumption, that for a subject in supine position 90% of the blood flows between upper body arteries and veins, while 10% of the blood flow supports the vasculature in the lower extremities [30].

Utilizing estimates for blood flow, pressure and volumes, values for model resistors and capacitors (compliances) can be found by rewriting the pressure-volume (6.1) and pressure-flow (5.4) relations as

$$
\begin{aligned}
R &= \frac{\bar{p}_{in} - \bar{p}_{out}}{\bar{q}}, \\
C &= \frac{\bar{V} - \bar{V}_{un}}{\bar{p}} = \frac{V_{str}}{\bar{p}},
\end{aligned}
$$

where $\bar{p}$, $\bar{q}$, $\bar{V}$ denote mean values for the respective blood pressures, flow, and volumes. Subscripts "un" and "str" denote unstressed and stressed volumes, respectively. The stressed volume fractions are given in Table 5.2.

For the heart model, parameters representing minimum and maximum elastance as well as timing of the pump function must be estimated. The minimum left ventricular elastance can be obtained from the pressure-volume relation (5.2), noting that when the left ventricular volume equals the end-diastolic volume (V_{ED}) we have

$$
\bar{p}_{pv} = E_{min} (V_{ED} - V_{lh,un}),
$$

where $\bar{p}_{pv}$ denotes the pulmonary venous pressure. This pressure is not appearing elsewhere in the model. We assumed that pulmonary venous pressure is slightly higher (4 mmHg) than its systemic counter-part [51, 136]. Similarly, the maximum left ventricular elastance can be predicted by assessing the same relation at the end-systolic phase. For this case

$$
p_{lh,sys} = E_{max} (V_{ES} - V_{lh,un}),
$$

where $p_{lh,sys}$ denotes the maximal systemic arterial pressure(obtained from the data) and V_{ES} denotes the end systolic volume. For both parameters we assumed that the unstressed value of the ventricular volume $V_{lh,un} = 10$ ml, which was used in previous studies (e.g. [34]).

The timing of the pump is achieved via parameters T_M, T_R and T. For this study we estimated T_M from data (for each cardiac cycle we let T_M be the time at which the pressure wave reached its maximum, while T_R was defined relative to the length of the cardiac cycle as $T_R = 0.19/T$ [34, 107]. Table 5.3 specifies parameter values for all model parameters.

Table 5.3: Model parameters: The nominal parameter values and equations used for predicting them. $\bar{p}_{au}$ includes data from the supine portion of the blood pressure (bp) time-series ($t < 180s$), and N denotes the number of points within this period. $\bar{p}_{au,sys}$ includes the systolic blood pressure values for the M periods found for $t < 180$. Values for venous blood pressure are from [1].

Name	Definition	Equation	Value	Units
V_{tot}	total blood volume	Eqn (5.10)	5377 ± 549	ml
l	height		183 ± 8	cm
w	weight		80 ± 10	kg
CO	cardiac output	$V_{tot}/60$	90 ± 9	ml/s
$\bar{p}_{au}$	upper body mean arterial bp	$\frac{1}{N}\sum_{i=1}^{N} p_{au}(i)$	68 ± 11	mmHg
$\bar{p}_{al}$	lower body mean arterial bp	$0.98\,\bar{p}_{au}$	67 ± 11	mmHg
$\bar{p}_{vu}$	upper body mean venous bp		3.5	mmHg
$\bar{p}_{vl}$	lower body mean venous bp		3.75	mmHg
$\bar{q}_{up}$	upper body flow	0.9 CO	81 ± 8	ml/s
$\bar{q}_{low}$	lower body flow	0.1 CO	9.0 ± 0.9	ml/s
$R_{i,op}$	small resistance, open valve		0.001	mmHg s/ml
$R_{i,cl}$	large resistance, closed valve		20	mmHg s/ml
R_{aup}	upper body peripheral resistance	$\dfrac{\bar{p}_{au} - \bar{p}_{vu}}{\bar{q}_{up}}$	0.81 ± 0.19	mmHg s/ml
R_{alp}	lower body peripheral resistance	$\dfrac{\bar{p}_{al} - \bar{p}_{vl}}{\bar{q}_{low}}$	7.1 ± 1.6	mmHg s/ml
R_{al}	upper body arterial resistance	$\dfrac{\bar{p}_{au} - \bar{p}_{al}}{\bar{q}_{low}}$	0.15 ± 0.03	mmHg s/ml
R_{vl}	lower body venous resistance	$\dfrac{\bar{p}_{vl} - \bar{p}_{vu}}{\bar{q}_{low}}$	0.028 ± 0.003	mmHg s/ml
C_{au}	upper body arterial compliance	$0.19\,\bar{V}_{au}/\bar{p}_{au}$	1.7 ± 0.4	ml/mmHg
C_{al}	lower body arterial compliance	$0.05\,\bar{V}_{al}/\bar{p}_{al}$	0.26 ± 0.06	ml/mmHg
C_{vu}	upper body venous compliance	$0.05\,\bar{V}_{vu}/\bar{p}_{vu}$	51 ± 5	ml/mmHg
C_{vl}	lower body venous compliance	$0.16\,\bar{V}_{vl}/\bar{p}_{vl}$	4.3 ± 0.4	ml/mmHg
$\bar{p}_{pv}$	mean pulmonary venous bp		4	mmHg
$\bar{p}_{lh,sys}$	mean max systemic arterial bp	$\frac{1}{M}\sum_{i=1}^{M} p_{au,sys}(i)$	102 ± 13	mmHg
V_{ED}	end-diastolic volume		125	ml
V_{ES}	end-systolic volume		70	ml
$V_{lh,un}$	unstressed ventricular volume		10	ml
E_{min}	min elastance	$\dfrac{\bar{p}_{pv}}{V_{ED} - V_{lh,un}}$	0.03	mmHg/ml
E_{max}	max elastance	$\dfrac{\bar{p}_{lh,sys}}{V_{ES} - V_{lh,un}}$	1.7 ± 0.2	mmHg/ml
T_R	max elastance to relaxation	$0.18/T$	0.20 ± 0.01	N.D.
T_M	time of max elastance	data	0.11 ± 0.01	N.D.
T	length of i'th cardiac cycle	data	0.90 ± 0.07	s

Initial values for all differential equations, i.e., for all arterial and venous pressures, as well as the left ventricular volume were set as average values predicted as described above. These values can be found in Table 5.3 along with values for all nominal parameters.

5.3 Model analysis

The model dynamics are first analyzed while the subjects were in supine position, followed by analysis of HUT. For the steady state analysis we first investigated the sensitivity of the carotid blood pressure to the model parameters, we then determined a set of identifiable parameters, and finally we used nonlinear optimization to estimate the parameters. After obtaining base parameters representing steady state dynamics, parameters being regulated by baroreflex regulation were estimated during HUT. Data analyzed for this study include continuous heart rate and blood pressure measurements, as well as gender, age, height, and weight of the subjects. Previous studies by [34, 131] have shown that parameter estimates obtained by minimizing the least squares error between computed and measured values of arterial pressure, gave rise to models that under-estimated cardiac output and total blood volume. These quantities are typically not measured. Consequently, to obtain a set of parameters providing realistic model estimates of cardiac output and blood volume, we used approximate values obtained using allometric scaling laws estimating blood volume as a function of height, weight, age, and gender. The total blood volume was scaled by 85% to get the volume of the systemic circulation, and as discussed in (5.10) cardiac output was estimated by assuming that the total blood volume is circulated in one minute.

The model developed in this study, estimates blood pressure and flow as pulsatile quantities, but since the model is analogous to an RC-circuit it does not allow for prediction of wave-propagation, consequently direct comparison of computed and measured values of blood pressure is erroneous. To obtain adequate pulsatility, we identify model parameters that allow prediction of systolic and diastolic values of blood pressure. These values can be obtained from computing the maximum and minimum pressure within each cardiac cycle. However, the maximum and minimum functions are not smooth, consequently, we applied the smoothing function [149]

$$\min_{\epsilon}(x) = -\epsilon \ln \left(\sum_i \exp(-x_i/\epsilon) \right)$$

for which $\epsilon > 0$ represents the degree of smoothness (large values of ϵ gives rise to more smoothing) and x represents the vector (indexed by i) to be minimized (or maximized).

The allometric data estimating cardiac output and blood volume will be included in the model output during supine position, where these quantities are assumed approximately constant. During HUT and subsequent control these quantities vary and thus model output will only include systolic and diastolic arterial blood pressure. Consequently, the model output

vector is given by

$$y_{sup} = [p_{au,sys,1}, ..., p_{au,sys,M}, p_{au,dia,1}, ..., p_{au,dia,M}, V_{st,1}, ..., V_{st,M}, CO_1, ..., CO_M]^T \quad (5.11)$$

$$y_{tilt} = [p_{au,sys,1}, ..., p_{au,sys,M}, p_{au,dia,1}, ..., p_{au,dia,M}]^T, \quad (5.12)$$

where M is the number of cardiac cycles analyzed and subscripts *sup* and *tilt* refer to supine and HUT simulations, respectively. Note, quantities in y do not depend continuously on time, but represent one value for each cardiac cycle. Using y, we defined the residual vector R between computed (y^c) and measured (y^d) quantities as

$$R = \frac{1}{\sqrt{K}} \left[\frac{y_1^c - y_1^d}{y_1^d}, \frac{y_2^c - y_2^d}{y_2^d}, ..., \frac{y_K^c - y_K^d}{y_K^d} \right]^T, \quad (5.13)$$

where K is the length of the model output vector. For simulations representing supine dynamics $K = 4M$, the model residual (5.11) has four entries of length M, while for simulations during HUT $K = 2M$, here the model residual (5.12) has two entries of length M. Since pressure, volume, and cardiac output have different units, and since the data segments analyzed may vary in length, we scaled the residual by the value of the measurements and by the square root of the number of samples K.

5.3.1 Sensitivity analysis

The first step in identifying a subset of parameters to be estimated given available data, was to conduct sensitivity analysis and rank parameters from the most to the least sensitive. The base model contains $n = 12$ parameters

$$\theta = \{R_{aup}, R_{al}, R_{vl}, R_{alp}, C_{au}, C_{al}, C_{vl}, C_{vu}, T_R, E_{min}, E_{max}, V_{un,lh}\}.$$

The sensitivity matrix is defined as

$$S = \frac{\partial R}{\partial \tilde{\theta}}, \quad (5.14)$$

where $\tilde{\theta}$ is log-scaled parameters and R is the residual vectors given in (5.11) and (5.12). Sensitivities were computed using the forward difference approximation

$$\frac{\partial y_k}{\partial \tilde{\theta}_i} = \frac{y_k(t, \tilde{\theta} + he_i) - y_k(t, \tilde{\theta})}{\delta}, \quad \text{where} \quad e_i = \begin{bmatrix} 0 & ... & 0 & \overset{i}{\hat{1}} & 0 & ... \end{bmatrix}^T$$

is the unit vector in the i'th component direction, and $\delta = \sqrt{\chi}$ is the step-size. $\chi = 10^{-8}$ is the integration tolerance used for solution of the dynamical system. We used a scaled 2-norm to
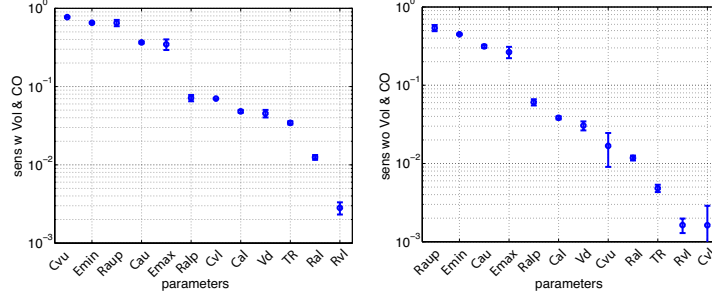
Figure 5.5: Ranked sensitivities $||\partial R/\partial \tilde{\theta}||_2$ plotted on a log scale. Values are displayed from the most to the least sensitive parameter. Left panel show sensitivities estimated using (5.11) and right panel shows those estimated using (5.12).

get the total sensitivity, S_i, to the i'th parameter

$$S_i = \left(\frac{1}{K} \sum_{j=1}^{K} S_{i,j}^2 \right)^{1/2}. \tag{5.15}$$

Sensitivities are shown in Fig. 5.5.

5.3.2 Subset selection

As suggested in [104] we combined two approaches for estimating a subset of uncorrelated parameters. First, we note that the model contains two parallel circuits predicting flow in the upper and lower body. For the supine dynamics, the model could be reformulated as an equivalent circuit with one branch. Thus, parameters in one of the two branches will not be identifiable. We chose to analyze parameters representing compartments in the upper body, while we kept parameters in the lower body compartments (containing less blood volume) constant. The reduced parameter set include parameters $\theta = \{R_{aup}, C_{au}, C_{vu}, T_R, E_{min}, E_{max}, V_{lh,un}\}$. Next, we used singular value decomposition and QR factorization to identify parameters. The sensitivity matrix defined in (5.14) was decomposed as $R'(\tilde{\theta}) = U\Sigma V^T$, where $\tilde{\theta}$ are the log-sacled parameters, Σ is a diagonal matrix containing the singular values σ_i of R', and V is the associated right eigenvector. The number of identifiable parameter values can be found by predicting the numerical rank ρ of R'. Given a tolerance ϵ, the numerical rank of the matrix is the largest k such that the singular values $\sigma_{n-k+1} > \epsilon\sigma_n$. For our study $\epsilon = \sqrt{\chi}$, the square root of the integration tolerance χ. Using ρ, the matrix of eigenvectors V can be written as $[V_\rho \ V_{n-\rho}]$. The parameters associated with the ρ highest eigenvectors are then found using QR-decomposition with column pivoting. It should be noted that the QR decomposition is not unique, but differ

with the concrete implementation of the algorithm. However, for a given ρ the algorithm will return a set of ρ identifiable parameters.

Independent of the exact algorithm, the subset is found by $V_\rho^T P = QR$, where Q is an orthogonal matrix, and the first ρ elements of R form an upper triangular matrix with diagonal elements in decreasing order. The permutation matrix P can be used to reorder the parameter vector $\hat{\theta} = P^T \theta$. Finally, the partition $\hat{\theta} = \{\hat{\theta}_\rho, \hat{\theta}_{n-\rho}\}$, where $\hat{\theta}_\rho$ contains the first ρ sensitive elements, while the vector $\hat{\theta}_{n-\rho}$ contains parameters that cannot be identified. In this study these were kept at their nominal parameter values. The latter does introduce bias in the computations, but reduces the variance. At the same time estimation of only sensitive parameters make the estimation algorithm more robust [31, 60]. For this study, we performed subset selection for the reduced parameter set noted above by analyzing the sensitivity matrix over the entire 180 second interval. This analysis was repeated for all five data sets for each of the two residuals. For the residual in (5.11), results show that independent of the data set studied four parameters could be estimated including $\hat{\theta}_\rho = \{R_{aup}, C_{au}, C_{vu}, E_{min}\}$, while for the residual in (5.12) only two parameters can be estimated $\hat{\theta}_\rho = \{R_{aup}, E_{min}\}$.

This parameter set was tested further, by computing pair-wise correlations. To do so we use the model Hessian defined by $\mathcal{H} = S^T S$, where S is the sensitivity matrix defined in (5.14). Using $\mathcal{H}$ the correlation matrix c can be computed as

$$c_{i,j} = \frac{C_{i,j}}{\sqrt{C_{i,i} C_{j,j}}}, \quad C = \mathcal{H}^{-1}.$$

The correlation matrix c is symmetric with 1's in the diagonal. All off-diagonal elements have values between $-1 \le c_{i,j} \le 1$, values close to 1 indicate that parameters are correlated [104]. Moreover it should be noted that c cannot be computed if $\mathcal{H}$ is singular. The aim here was to investigate correlations among parameters chosen by subset selection. For this subset $\mathcal{H}$ is not singular, and thus c can easily be computed. For either parameters, the entries $c_{i,j}$ are not close to 1, indicating that all parameters in the subsets are identifiable. It should be noted that all analysis methods presented here are local and only valid in a region close to the parameter values investigated, i.e., results may change as the parameters change. To ensure that optimized parameters were not correlated, this analysis should be repeated for the optimized parameter values.

5.3.3 Parameter estimation

Nonlinear optimization was employed to estimate a set of model parameters that minimize the least squares error between the measured data and the model. This formulation relies on the assumption that the measurements can be described fully by the underlying model plus an error

term representing the measurement noise, i.e., we assume that

$$y_{d,i} = y_m(t_i; \theta_\rho, \theta_{n-\rho}) + \epsilon_i, \quad i = 1, 2, \ldots, K$$

where K denotes the number of elements in the output vector. For formulation of the statistical model we assume that the errors ϵ_i are independent identically distributed (iid) random variables with mean $E[\epsilon_i] = 0$, covariance $\text{cov}(\epsilon_i, \epsilon_j) = 0$, and constant variance $\text{var}[\epsilon_i] = \mu^2$. Given this form of the statistical model, the objective function can be defined using the sum of least squares errors

$$\theta_{opt,\rho} = \arg\min_{\theta_\rho} J(\theta), \quad J(\theta) = R^T R = \frac{1}{K} \sum_{i=1}^{K} \left| \frac{y(t_i; \theta_\rho, \theta_{n-\rho}) - y_i}{y_i} \right|. \tag{5.16}$$

The scaling with y_i is included to ensure that all quantities in the output vector can be compared. Note, only parameters in the subset θ_ρ will be estimated, while parameters that are not identifiable $\theta_{n-\rho}$ remain constant at the nominal parameter values. The identifiable parameters θ_ρ were estimated using the Levenberg-Marquadt optimization algorithm [75]. Upper and lower bounds were set for all model parameters. For simulations presented here we allowed parameters to increase or decrease by a factor of 4 from nominal parameter values.

As outlined below, model parameters were estimated first in supine position, and then during HUT.

1. First one value for each of the identifiable parameters during supine position for $t = 0-180$ seconds was estimated. For this simulation, the minimization problem in (5.16) was solved using the residual defined in (5.11) providing optimal values $\hat{\theta}_\rho = \{\hat{R}_{au}, \hat{C}_{au}, \hat{C}_{vu}, \hat{E}_{min}\}$.

2. Second, over the same interval time-varying parameters were estimated as described in (5.9). As in step 1, I solved (5.16) using the residual defined in (5.11) providing optimal values $\hat{\theta}_\rho = \{\hat{\gamma}_{R_{au},i}, \hat{\gamma}_{C_{au},i}, \hat{\gamma}_{C_{vu},i}, \hat{\gamma}_{E_{min},i}\}$. To understand the impact of varying parameters in time, we repeated this simulation three times, including one value for each parameter for each 6, 8, and 10 seconds of data, i.e., we estimated $4 \times \eta$ parameters for $\eta = (18, 23, 30)$.

3. Then the gravitational pooling of blood in the legs was simulated occurring as a response to HUT. Initial values for this simulation were assigned to the optimal values predicted in step 1. HUT simulations were compared against 180 seconds of data for $t = 110 - 290$ seconds. Note this interval overlaps with the interval used for predicting supine dynamics.

4. Finally, I modeled blood pressure regulation by varying parameters representing vascular resistance and cardiac contractility in time as discussed above and in step 2. For this optimization problem (5.9) was used to make parameters time-varying and I solved (5.16)

using the residual defined in (5.12). This optimization determined optimal values $\hat{\theta}_\rho = \{\hat{\gamma}_{R_{au},i}, \hat{\gamma}_{E_{min},i}\}$.

5.4 Results

Following the steps outlined above, I first show results obtained for a subject in supine position followed by results obtained when the same subject was exposed to a HUT test.

5.4.1 Optimization during supine position

For simulations estimating the supine dynamics we used heart rate and blood pressure data from the first 180 seconds of the time series (see Fig. 5.1(e)). The estimates of patient specific parameters were obtained using two approaches, first one set of parameters was estimated over the entire 180 seconds of data, second model parameters were allowed to vary slowly in time. The latter was done using the approach outlined in section 5.3.2. Moreover, to ensure that results were similar for measured and calculated carotid artery data, simulations were repeated (with one parameter per 8 seconds) for both datasets. Finally, Table 5.4 gives a comparison of mean values obtained over all five data sets.

Results comparing simulations with the measured carotid data are shown in Fig. 5.6. Results comparing against calculated carotid data were not significantly different and are thus not shown. Generally, we found that better results are obtained when parameters are allowed to vary slowly in time. Compare Figs. 5.6(a) and 5.6(e). Both simulations gave the same mean value predictions for p_{au}, though with time-varying parameters the model was able to capture fast and slow (likely due to respiration) oscillations. Figure 5.6(a) shows results obtained while estimating one set of parameters of the entire 180 seconds of data, and Fig. 5.6(e) shows results when parameters vary slowly in time. For each of the two simulations, the second column of Fig. 5.6 shows a 5-second segment from $t = 82 - 89$ seconds. The third and fourth columns of Fig. 5.6 show data versus computed values of diastolic and systolic pressures, respectively. It should be noted that time-varying parameters are needed to accurately predict systolic and diastolic pressures, for these simulations $R^2 = 0.65$ and $R^2 = 0.77$.

One limitation of results reported here is that estimated compliance values reflect that the pulse-wave is measured in a peripheral vessel, rather than in the carotid artery. Consequently, compliance values may be too small compared with expected values in the central vessels. However, all other quantities (pressures, volumes, and flows) estimated by the model were physiologically reasonable.
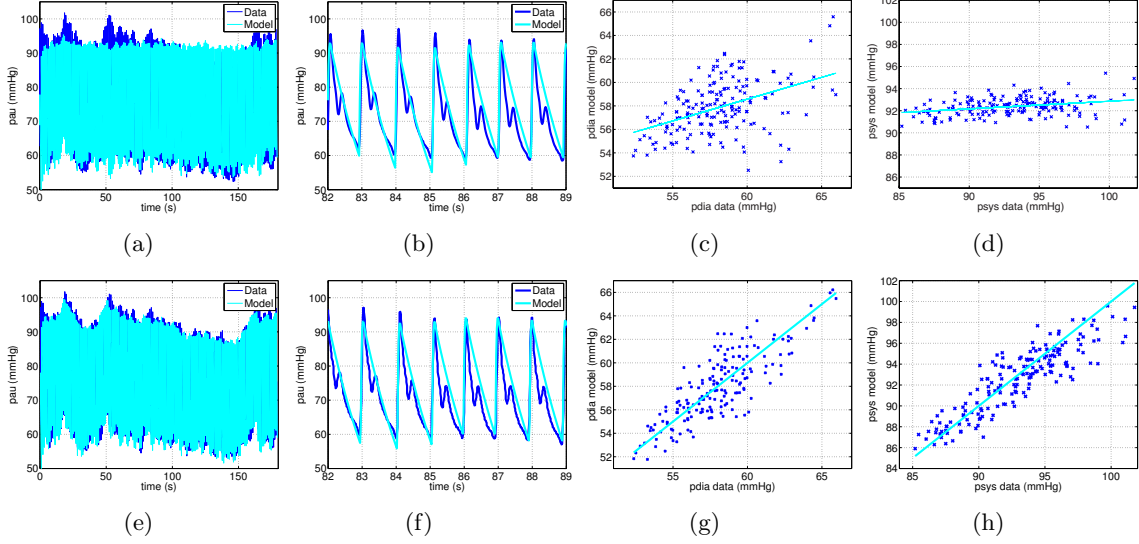
Figure 5.6: Graph (a) shows the measured upper body arterial blood pressure (dark line) and the optimized model output (light line) in supine position (over a 180 seconds time span); (b) shows a zoomed portion of (a) for $t = 82 - 89$ seconds. Graphs (c) and (d) show model versus computed values for diastolic and systolic pressures, respectively, where the light line shows the best one-to-one fit between the computed and measured values. Ideally, the dots should lie on a straight line with slope 1. Graphs (e-h) show the same as (a-d), respectively, but obtained by estimating time-varying parameters. With time-varying parameters (g-h) $R^2 = 0.65$ (diastolic) and $R^2 = 0.77$ (systolic), compare diastolic and systolic computed outcomes to their respective expected outcomes.

Table 5.4: Optimized parameter values found in supine position. The first three columns give results for one representative subject, while columns 4-5 give results averaged over all five subjects.

Parm	Init	Opt	Opt	Init	Opt	Unit
	1 sub	1 sub	(time-var)	5 sub	5 sub	
R_{aup}	0.81	0.86	0.89 ± 0.18	0.82 ± 0.19	0.89 ± 0.18	mmHg s/ml
C_{au}	1.64	2.3	1.4 ± 0.5	1.8 ± 0.4	1.4 ± 0.5	ml/mmHg
C_{vu}	53	67	69 ± 7	54 ± 9	69 ± 7	ml/mmHg
E_{min}	0.03	0.014	0.015 ± 0.002	0.027 ± 0.007	0.015 ± 0.002	mmHg/ml

5.4.2   HUT optimization

Figure 5.8(a) shows the measured and calculated blood pressure and the corresponding model output for a representative subject tilted to 60°. This result represents dynamics without blood
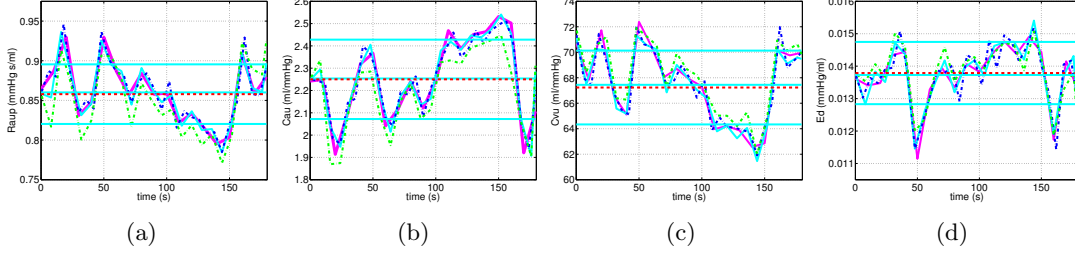
Figure 5.7: The graphs show the four parameters in the subset that were estimated as time-varying parameters in the supine position including (a) upper body peripheral resistance R_{aup}, (b) upper body arterial compliance C_{au}, (c) upper body venous compliance C_{vu}, and (d) minimum ventricular elastance E_{min}. The "zig-zag" lines show the results obtained with 6-sec (blue dashed), 8-sec (cyan solid), and 10-sec (magenta solid) intervals, respectively, against the measured carotid data, while the dashed green line shows results obtained with the calculated carotid data. The solid horizontal lines show mean values and standard deviations for the estimation of the time-varying parameters, and the dashed horizontal red line show the results obtained when estimating one value over the entire period.

pressure regulation, i.e., it was obtained by keeping all parameters constant at optimized values obtained in supine position. Results were obtained by accounting for hydrostatic pooling of blood in the legs as described in (6.18). The arterial blood pressure drops during HUT, and remains low for the duration of the simulation. Figures 5.8(b) and 5.8(c) show that when parameters R_{aup} and E_{min} (shown in Figs. 5.8(e) and 5.8(h)) were controlled the model was able to fit the observed pressure. The result in 5.8(b) was obtained by estimating the time-varying model parameters $\theta_{ctr} = \{\gamma_{R_{aup},i}, \gamma_{E_{min},i}\}$, minimizing the least squares error between measured and modeled carotid blood pressure, while the result in Fig. 5.8(c) reflects comparison with the calculated carotid data as given in (5.1). Results in Figs. 5.8(f) and 5.8(i) show diastolic and systolic model predictions plotted against data. The cyan line with slope one, indicates the unity between model and data. The top row in Fig. 5.9 show results obtained for all five subjects comparing model results against measured carotid data. The bottom two rows (cyan line) of Fig. 5.9 show piecewise linear predictions of peripheral resistance R_{aup} and minimum elastance E_{min}, while Fig. 5.10 show pooled predictions of R_{aup} and E_{min} for all five datasets. Based on these fits we propose to model the change in these quantities using combinations of Hill and

polynomial functions given by

$$
X(t) = \begin{cases} X_{min,ss} & t \leq t_{tilt} \\ X_{min,ss} - (X_{min,ss} - X_{min,m})\dfrac{(t - t_{tilt})^n}{X_{min,h}^n + (t - t_{tilt})^n} & t > t_{tilt} \end{cases}
$$

$$
Y(t) = A(t - t_1)^{k_1}(t_2 - t)^{k_2}, \quad A = \frac{-B}{(t_2 - t_1)/2)^{(k_1 + k_2)}},
$$

where $X_{min,i}, t_{tilt}, n, B, k_1, k_2, t_1, t_2$ are model parameters. The minimum elastance E_{min} is predicted using $X(t)$ and the peripheral resistance by combining the expressions for X and Y. Predictions of arterial pressure at the level of the carotid using these functions are shown in second row of Fig. 5.9. Note the functions predict steady level and transition during tilt fairly well, but neglect the faster variation within these periods. Hence these functions capture the overall trend in the dynamical responses but ignore the faster variations captured by the piecewise linear functions.

The significance of the model was corroborated further by examining dynamics of quantities for which data are not available. Starting at the heart, the volume and cardiac output for a representative subject are depicted in Fig. 5.11. The ventricular volume (Figs. 5.11(a) and 5.11(b)) is within normal physiological bounds for a healthy person [63]. Moreover, consistent with literature observations [2, 62, 107], the CO is decreased slightly when the blood pressure regulation is inhibited as depicted in Fig. 5.11(c). However when the blood pressure regulation is engaged, CO is increased after the onset of HUT and then returns to the values before HUT as seen in Fig. 5.11(d).

Figure 5.12 shows the lower body arterial p_{al} and venous p_{vl} pressure, the upper body venous pressure p_{vu}, as well as flow between upper and lower body on the arterial q_{al} and venous q_{vl} side for a representative subject. We also show dynamics of resistance between upper and lower body on the venous side R_{vl}. These figures represent dynamics observed during HUT, i.e., model parameters are time-varying. Immediately upon HUT flow from lower to upper body veins stop, as the venous valve closes preventing return flow in the leg veins. As a result flow to the lower body is reduced. These observations agree with those found in literature [71]. Similar observations were made for all five data sets.

Simulations shown above were obtained by regulating two quantities R_{aup}, and E_{min}, while $R_{alp} = kR_{aup}$. Results show, that similar dynamics were obtained for all five datasets. Moreover, it should be noted (compare Figs. 5.7 & 5.10) that the parameters estimated during HUT (Fig. 5.10) vary by orders of magnitude, while in supine position (Fig. 5.7) they only varied slightly. Finally, it should be noted, that during HUT none of the compliance parameters were included in the parameter estimation, these are only identifiable when cardiac output and blood volume are included in the least squares cost (5.16). During supine position we used the residual
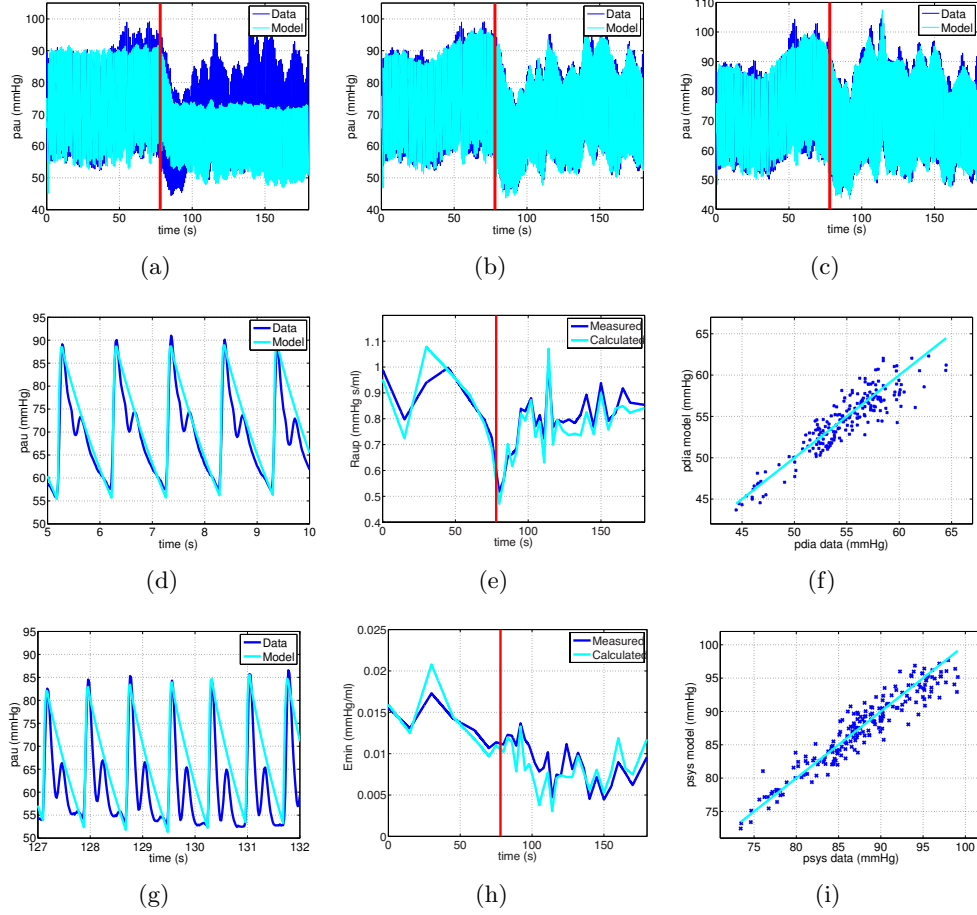
Figure 5.8: Panel (a) shows the measured upper body arterial blood pressure and the model output for a subject tilted over a 180 second time span, without parameters impacted by cardiovascular regulation; (b) shows the same quantities as (a) where parameters impacted by cardiovascular regulation are estimated as described in (5.9); (c) shows the same as (b) using the calculated carotid pressure (5.1). Panels (d) and (g) show zoomed portions of (b) for $t = 0 - 5$ seconds and $t = 127 - 132$ seconds, respectively; Panels (e) and (h) shows optimized values for R_{aup} and E_{min}, the dark blue line shows results obtained optimizing against measured carotid data (b) and the light cyan line against calculated carotid pressure (c). Finally, (f) and (g) show predictions of diastolic ($R^2 = 0.83$) and systolic ($R^2 = 0.87$) pressure for (b). The vertical red line indicates the onset of HUT.

in (5.11), but during HUT, the blood volume and cardiac output are expected to vary, thus we cannot include our pseudo data estimating overall values for the subject in question. Thus during HUT identifiability was done using the residual in (5.12) giving rise to a subset without compliance parameters.
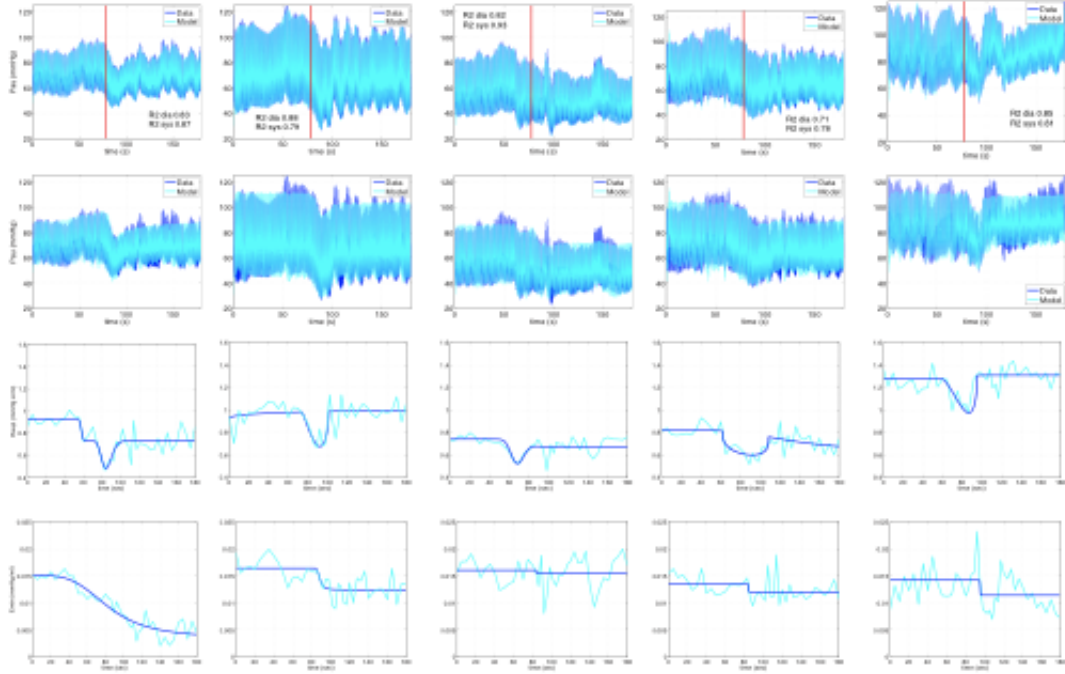
Figure 5.9: Results showing computed and measured carotid blood pressure for five subjects included in the study. Top row shows results predicting time-varying parameters using piecewise linear functions, the second row shows results predicting arterial blood pressure using functional expressions for R_{aup} and E_{min}, the bottom two rows show predictions of R_{aup} and E_{min}. For each subject R^2 values are marked on the graphs. The vertical red line (top row) marks the onset of the tilt.
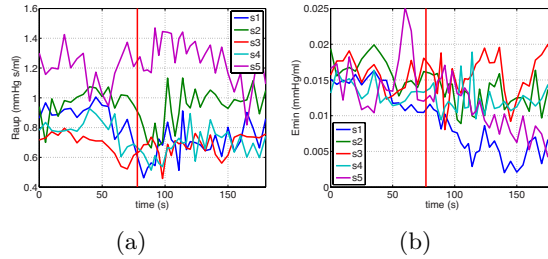
Figure 5.10: Estimated values for upper body resistance R_{aup} and and minimum contractility E_{min} for all five subjects.

5.5   Discussion and conclusions

This study has provided an approach to examine cardiovascular regulation during HUT. This was done by developing a five-compartment model that uses heart rate as an input to esti-
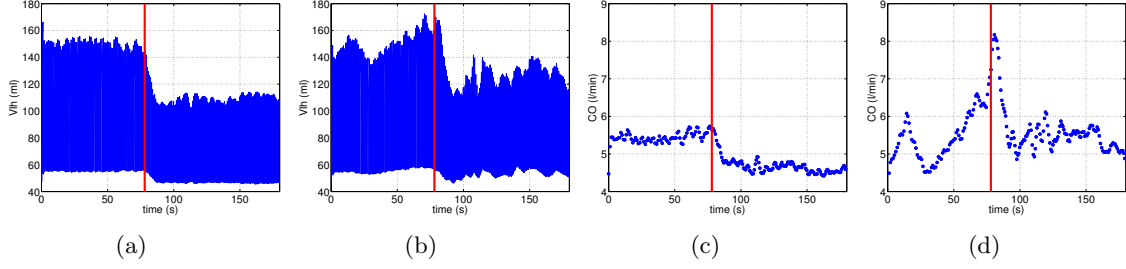
Figure 5.11: First two graphs show ventricular volume during HUT without (a) and with (b) cardiovascular regulation. The associated cardiac output are shown in (c) and with (d). The vertical lines mark the onset of HUT.
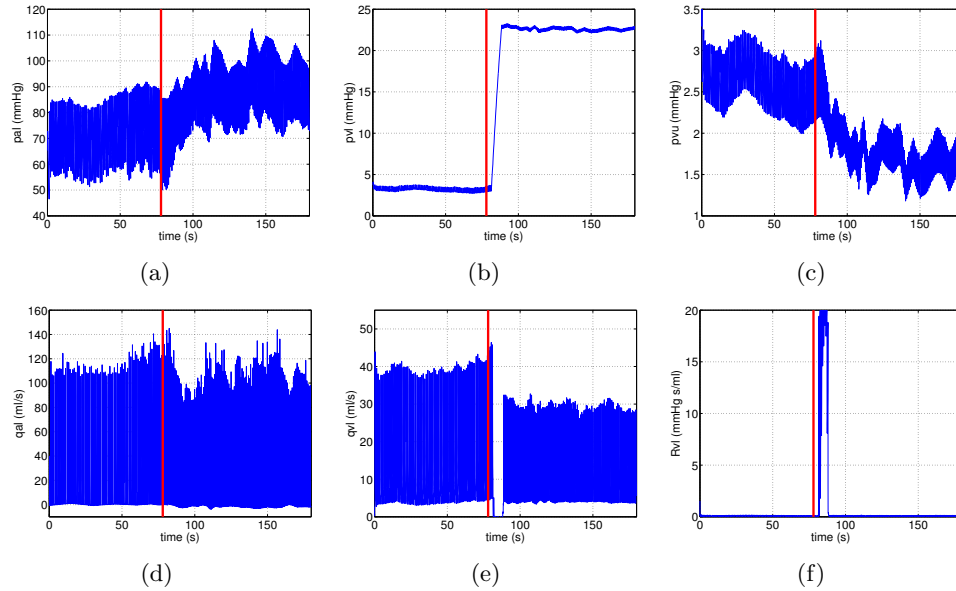
Figure 5.12: (a) Pressure in the lower body arteries; (b) pressure in the lower body veins; (c) pressure in the upper body veins; (d) flow f from upper to lower body arteries. (e) flow from lower to upper body veins; (f) resistance between lower and upper body veins. The vertical lines mark the onset of HUT.

mate pulsatile values of blood flow, pressure, and volume. HUT was imposed by including gravitational pooling of blood in the legs, and the autonomic response to HUT was included via time-varying parameters estimating vascular resistance and cardiac contractility. Nonlinear optimization minimizing the least squares error between measured and computed values of systolic and diastolic blood pressure was used to estimate the time-varying model parameters.

73

The model was compared with measured and calculated values for cardiac blood pressure for five healthy young adults.

Results showed (see Figs. 5.6–5.9), that the model was able to fit measured and calculated carotid blood pressures in supine position and during HUT. We noted, as expected that parameter variation during HUT is significantly larger than in supine position (compare Figs. 5.7 & 5.10). Based on these observations, we hypothesize that the large changes observed in Fig. 5.10 are due to cardiovascular regulation of these targets, while comparatively small variations observed in Fig. 5.7 (summarized in Table 5.4) is a result of variation due to respiration [137]. During inspiration the lungs are filled with air causing the diaphragm to lower, as a result the transmural pressure in the upper-body arteries and veins decrease. This decrease in tissue pressure is likely to impact compliance and resistance of the vessels. Similarly, it is likely that cardiac contractility is decreased during inspiration. However, assuming that no controls are operating while the subject is in supine position is not realistic. The control system is continuously active [32]. In addition, other quantities estimated by the model including cardiac output, pressures in the other compartments, blood volumes, were all reasonable compared to values reported in literature [1, 51].

To model the regulation during HUT, we varied upper and lower body resistance (R_{aup} and $R_{alp} = kR_{aup}$) and minimum elastance of the left heart (E_{min}). These quantities were modeled as piecewise linear time-varying functions, described using a set of nodes $\gamma = \{\gamma_{R_{aup},i}, \gamma_{E_{min},i}\}$ as described in (5.9). Results showed that immediately upon HUT, peripheral resistance dropped. This drop could be related to the muscle action [119, 146] or be a consequence of changes in hydrostatic pressure in the compartment below the heart. The latter is more likely, since the HUT maneuver is executed in a relaxed fashion, and no massive muscle action is provoked. After the initial drop, arterial peripheral resistance increased due to contraction of smooth muscles in the muscular and the elastic arteries, respectively, secondary to increased nerve traffic in the sympathetic efferent nerves. Sympathetic nerve activation also has a positive inotropic effect on the heart decreasing the left ventricular elastance allowing the heart to pump more blood through the system.

Due to changes in arterial resistance, blood volume is redistributed between the lower and upper body. Due to the increased hydrostatic pressure in the dependent regions during HUT, blood volume increases more in the lower body than in the upper body, which results in approximately 25% reduction of ventricular blood volume as described by [123] and [130]. The reduction in ventricular volume is paralleled by a significant drop in stroke volume as shown by [71] and [82]. Similar results were also observed in previous modeling studies [25, 34, 93, 107].

It should be noted that we controlled R_{aup} and R_{alp}. The need to control the upper body resistance stems from the fact that vessels in the abdomen including the gut, liver and kidney were included in the upper body. It is likely that if we had distinguished differently between

74

upper and lower body, by moving these vessels to the lower body that it would be adequate to control R_{alp}, though the concept presented in this study would be directly transferable to a model with redistributed volumes.

As the model shows, through regulation of the selected quantities, blood pressure at the carotid bifurcation returns to homeostatic levels after HUT, in line with the notion that the carotid baroreceptors dominate the blood pressure regulation in humans [82, 90]. Another key observation is that with regulation of the model parameters, cardiac output increases after the onset of HUT and then returns to homeostatic levels, which would also be expected as the metabolic demands in the passive upright position should be of the same magnitude as in supine state. This agrees to some extent with results reported in literature. Enishi et al [71] reported a slight decrease in cardiac output 1 minute after HUT, while [90] as well as [82] reported larger drops in cardiac output; their results though were reported for a subject being tilted for 10 and 20 minutes, respectively. Further proof of the significance of the model is given when examining other variables in the model where the left ventricular volume decreases when the tilt is performed in response to the decrease in filling pressure, which is also seen experimentally [71]. The estimated venous pressure (p_{vl}) increases in the lower compartment as previously shown by others [22, 69], while central venous pressure drops, again our results are similar to those reported in literature [82, 90].

Moreover, we showed that by prescribing E_{min} and R_{aup} by simple functions it is possible to predict general trends in arterial blood pressure, while minor oscillations could not be predicted, these may be a result of respiration, or the so-called Mayer-waves [105]. It should be noted that these secondary oscillations are more pronounced while the subject is tilted than in supine position,which is in agreement with the observations reported and analyzed by [105]. The results confirm our observations that during tilt, peripheral resistance drops, and then returns to the value before the tilt, or is slightly increased, while the minimum elastance is reduced slightly.

One limitation of our study is that heart rate was an input to the model, and thus, the model mainly predicts impact of sympathetic regulation via estimation of cardiac contractility and vascular resistance. In future studies one could consider including a model predicting heart rate as was done by Olufsen *et al.* [92, 95] and others [104, 105, 129]. Moreover, if this approach is used for a larger population study, the validity of values used for parameters not estimated should be analyzed further. In this study we used "text-book" values valid for the healthy young male, however, they would not be valid for all population groups. For example, values for venous pressure may be too low, while the assumption that the entire blood volume is circulated in a minute, used to obtain an estimate for cardiac output may not hold in general. One way to circumvent this last assumption is by including measurement of cardiac output while the subject is in supine position.

Finally, it should be noted, that the small secondary waves present in the blood pressure

data cannot be reproduced by our model in its present state. These waves arise from the reflection of the pulse-wave from the periphery, a phenomenon not included in our model. Such effects could be included in a number of ways, either by developing a lumped parameter wave propagation model from Womersley theory as suggested by [145], or by using empirically derived nonlinear capacitors as suggested by [109], though both of these ideas lead to a more complex model. While adding effects of wave-propagation are important for many applications, e.g., for the study of wave propagation in normal and pathological arterial networks or for studies designed to analyze modulating the coronary perfusion pressure, the inclusion of wave reflections are most likely of little importance in the cardiovascular control system.

Chapter 6

Cardiovascular Dynamics During Head-up and Head-down Tilt Assessed via Pulsatile and Non-pulsatile Models

Abstract

This study presents a pulsatile and a non-pulsatile model for the prediction of head-up tilt (HUT) and head-down tilt (HDT) dynamics for healthy young adults. In this study, HUT refers to tilting a patient from supine position upright, while HDT refers to the process of tilting the patient back to supine position after HUT. To explore potential deficits within the autonomic control system, which maintains the cardiovascular system at homeostasis, many people suffering from dizziness or light-headedness are often exposed to the head-up tilt test. This system is complex and difficult to study in vivo. As a result, we show how mathematical modeling can be used to extract features of the system that cannot be measured experimentally. More specifically, we show that it is possible to develop a mathematical model that can predict changes in cardiac contractility and vascular resistance, quantities that cannot be measured directly, but which are useful to assess the state of the system. The cardiovascular system is pulsatile, yet predicting the control in response to head-up tilt for the complete system is computationally challenging, and limits the applicability of the model. In this work we show how to develop a simpler non-pulsatile model that can be interchanged with the pulsatile model, which is significantly easier to compute, yet it still is able to predict internal variables. The models are validated using head-up tilt and head-down tilt data from healthy young adults.

6.1 Introduction

Emergency rooms and syncope clinics see a large number of people who have experienced light-headedness or dizziness. These symptoms may be associated with orthostatic intolerance: the inability to maintain blood pressure and flow in response to active standing or head-up tilt (HUT). Orthostatic intolerance [64] is triggered by a number of factors, the most important being dysautonomia, a disorder associated with the autonomic nervous system. This phenomenon is difficult to diagnose not only due to the ambiguity of the disorder, but also due to the inability to obtain clinical data for quantities pertinent to cardiovascular regulation. Consequently, we propose the use of mathematical modeling as a tool to gain insight and knowledge to predict quantities that can not be observed, which potentially can be used in diagnosis and treatments.

To this effect, our model can predict blood pressure and heart rate dynamics observed during HUT and head-down tilt (HDT). The protocol starts with a subject resting in supine position on a tilt-table. After steady oscillating values for heart rate and blood pressure have been recorded, the subject is tilted head up to a 60 degree angle. After 5-10 minutes, the subject is tilted back to supine position. Upon HUT, blood is pooled in the lower body causing a drop in blood pressure in the upper body, while blood pressure in the lower body is increased. HDT elicits the opposite response. In response to HUT, for healthy subjects, the autonomic system causes an increase in heart rate, cardiac contractility, and peripheral resistance, redistributing blood volume and thereby re-establishing homeostasis. For patients suffering from dysautonomia, these responses may be partly or completely inhibited causing chronic syncope and constant discomfort for patients.

More specifically, this paper develops a non-pulsatile model for the cardiovascular system that can predict HUT and HDT dynamics. We compare the non-pulsatile model with a pulsatile model, and show that parameters estimated with the pulsatile model can be used within the non-pulsatile model. The pulsatile model is beneficial because it enables analysis of dynamics within beats and can be used to understand how modulation of the system affects pulsatility [104], which is useful in the study of the response immediately following HUT (within the first minute of the tilt) and HDT. However, the pulsatile model is complex, thus if the objective is to analyze dynamics over longer time-scales, it is adequate to analyze the system with the simpler non-pulsatile model. For example, if the objective is to study dynamics associated with HUT followed by HDT (10-20 min).

Besides being able to interchange the non-pulsatile and pulsatile models, in itself, the non-pulsatile model has multiple advantages. First, since it is less complex, coupling a non-pulsatile model with more advanced models studying larger systems such as the respiratory or renal systems becomes feasible. The respiratory cycle is approximately a fourth of the cardiovascular cycle, and control associated with respiratory dynamics take min-hours [51]. The renal system

is one of the most complex physiological feedback systems, it interacts with the cardiovascular system, and feedback associated with this system is hours-days [51].

Even if the objective is to study the impact of fainting, often analyzed using HUT tests, it may be necessary to use a simpler model. Typically, after HUT it takes 10-20 minutes before the subject tilted experiences light headedness [64]. Finally, it should be emphasized that computations with the non-pulsatile model are significantly faster, in particular, since it is no longer necessary to account for the discrete events associated with opening and closing of the heart valves. In the following, we will present both a pulsatile and a non-pulsatile model and show that they can be used interchangeably in the study of HUT and HDT dynamics.

6.2 Methods

This section describes the pulsatile and non-pulsatile models, as well as the models required to predict gravitational effects and autonomic regulation necessary to predict HUT and HDT dynamics. This study includes three simulations:

(A) Steady state (before tilt) with the pulsatile and non-pulsatile models

(B) HUT for the pulsatile and non-pulsatile models

(C) HUT to HDT for the non-pulsatile model

We first discuss the data used for testing the models, then we describe the two models, the modeling of HUT and HDT, and finally we describe the methods needed for comparing model predictions.

6.2.1 Data

Pulsatile measurements include ECG signals recorded using standard precordial leads and blood pressure recorded using photoplethysmography (Finapres Medical Systems B.V.). Data was collected at the Coordinating Research Centre at Frederiksberg Hospital, Copenhagen, Denmark from healthy young male volunteers with no known heart or vascular diseases. The subjects were left to rest in supine position for 10 minutes. Subsequently, the subjects were tilted via a tilt table to an angle of 60 degrees at a speed of 15 degrees per second measured by way of an electronic marker. The subjects remained tilted for five minutes, and were then tilted back to supine position at the same tilt speed.

For the model based analysis of the pulsatile model, we extracted a total of 290 seconds of data: including a 180 second segment recorded while the subjects were in supine position for simulation (A) (see the second graph in Fig. 6.1), a 180 second segment recorded during HUT
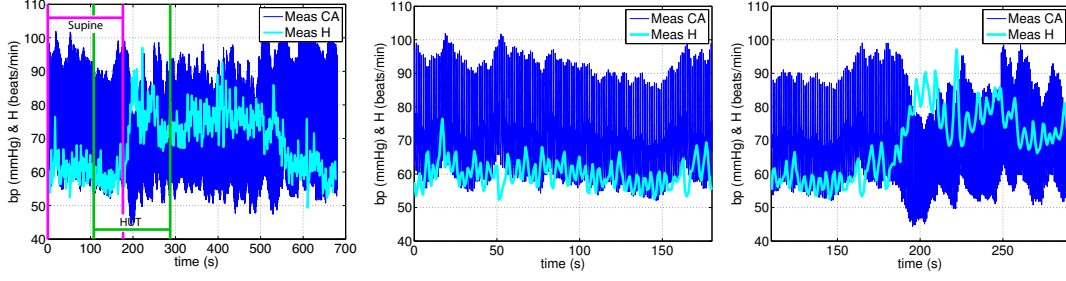
Figure 6.1: Graphs show the measured carotid pulsatile blood pressure (blue) and heart rate (cyan) for the complete data set. Data used to estimate the dynamics in supine position are marked with pink lines on the first graph and data used for prediction of HUT is marked with green lines on the first graph. The analysis of HUT followed by HDT use the entire time-series depicted. The second graph depicts a zoomed portion of the supine position data, while the last graph shows zoomed portion of the HUT data. Note there is an overlap between the data shown in the second and last graphs.
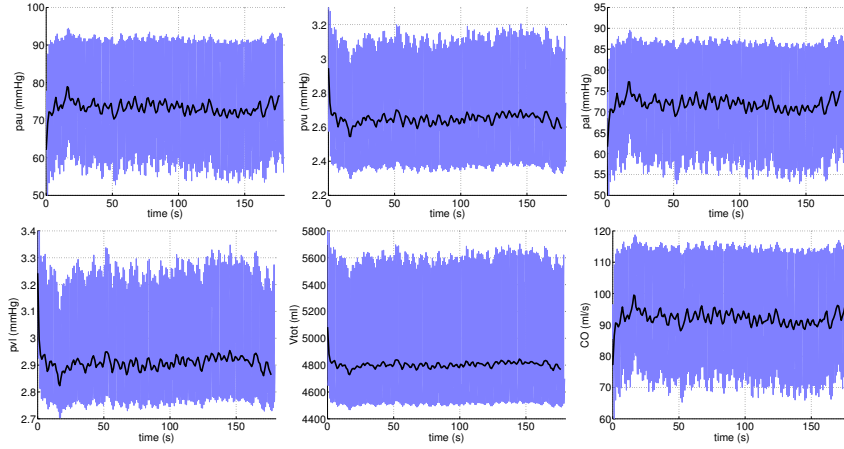
Figure 6.2: Upper body arterial and venous blood pressures, lower body arterial and venous pressures, total blood volume, and cardiac output results obtained using optimized values from the pulsatile model (blue) and calculated average values concatenated over each cardiac cycle (black) in supine position.

for simulations (B) and (C) (see the last graph in Fig. 6.1). Simulation C overlaps with the supine segment as illustrated on the first graph of the figure. Average blood pressure values were obtained for simulations with the non-pulsatile model. For each cardiac cycle, the mean of all pressures, cardiac output, and total blood volume outputs from the pulsatile model simulations were calculated. Then we concatenate those averages to use as data for the non-pulsatile model, see the black lines in Figures 6.2 and 6.3 for simulations (A) and (B), respectively. A longer
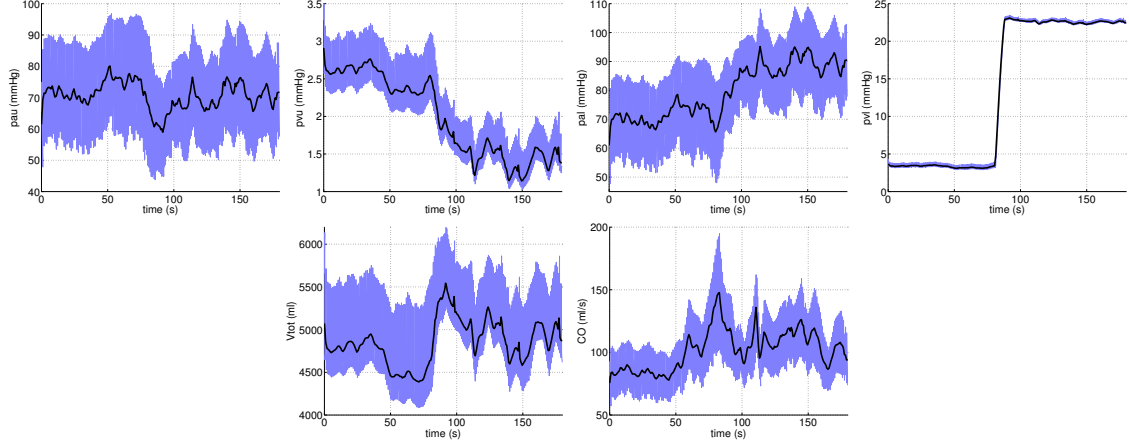
Figure 6.3: Upper body arterial and venous blood pressures, lower body arterial and venous pressures, total blood volume, and cardiac output results obtained using optimized values from the pulsatile model (blue) and calculated average values concatenated over each cardiac cycle (black) during HUT.

time scale extendend beyond 290s of the tilt portion of the data is used to include HDT for simulation (C). We use this data, $x = \{p_{aum}, p_{vum}, p_{alm}, p_{vlm}, V_{totm}, \text{and } CO_m\}$, to compare the two models.

6.2.2 Lumped cardiovascular models

This section describes the pulsatile and non-pulsatile cardiovascular models depicted in Figure 7.1. These models are developed to estimate blood flow, volume, and pressure in the systemic circulation during HUT for both pulsatile and non-pulsatile models and HDT for the non-pulsatile model only.

Both the pulsatile and non-pulsatile models follow the same basic layout shown in Figure 7.1, including four compartments representing arteries and veins in the upper and lower body and a compartment representing the heart. The latter, is the only compartment that differ between the two models. The general equations outlined below are valid for both models.

For each compartment, a pressure-volume relation can be defined as

$$V_i - V_{un} = C_i(p_i - p_{ext}), \tag{6.1}$$

where V_i (ml) is the compartment volume, V_{un} (ml) is the unstressed volume, C_i (ml/mmHg) is the compartment compliance, p_i (mmHg) is the compartment instantaneous blood pressure, and p_{ext} (mmHg) (assumed constant) is the pressure in the surrounding tissue. Moreover, for
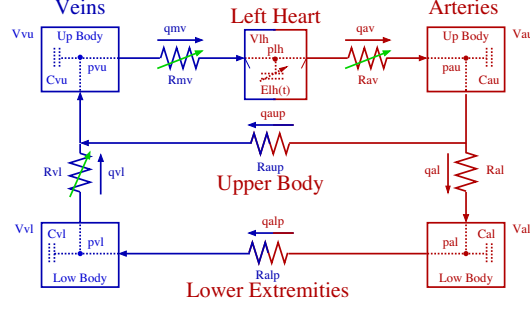
Figure 6.4: Compartment model predicting cardiovascular dynamics. For each compartment an associated blood pressure p (mmHg), volume V (ml), and compliance C (ml/mmHg) are defined. The compartments represent the upper body arteries (subscript au), lower body arteries (subscript al), upper body veins (subscript vu), lower body veins (subscript vl), and the left heart (subscript lh). Resistances R (mmHg s/ml) are placed between all compartments: R_{al} denotes the resistance between arteries in the upper and lower body, R_{aup} and R_{alp} denote resistance between arteries and veins in the upper and lower body, respectively. For the pulsatile model, the two heart valves, the mitral valve and the aortic valve, are modeled as pressure dependent resistors R_{mv} and R_{av}. Finally, the resistance between the lower and upper body veins R_{vl} is also modeled as pressure dependent to prevent retrograde flow into the lower-body during the HUT.

each compartment, the change in volume is given by

$$\frac{dV_i}{dt} = q_{in} - q_{out}, \tag{6.2}$$

where q (ml/s) denotes the volumetric flow. Using a linear relationship analogous to Ohm's law the volumetric flow q (ml/s) between compartments can be computed as

$$q = \frac{p_{in} - p_{out}}{R}, \tag{6.3}$$

where p_{in} and p_{out} are the pressure on either side of the resistor R (mmHg s/ml). Differentiating (6.1), using (6.2), and inserting (6.3) allows us to obtain a system of differential equations in blood pressure of the form

$$\frac{dp_i}{dt} = \frac{1}{C_i}\frac{dV_i}{dt} = \frac{1}{C_i}\left(\frac{p_{i-1} - p_i}{R_{i-1}} - \frac{p_i - p_{i+1}}{R_i}\right),$$

where i refer to the compartment for which the pressure p_i is computed, while $i-1$ and $i+1$ refer to the two neighboring compartments. For resistances that appear between compartments, R_{i-1} refer to the resistance between compartments $i-1$ and i, and R_i refers to the resistance between
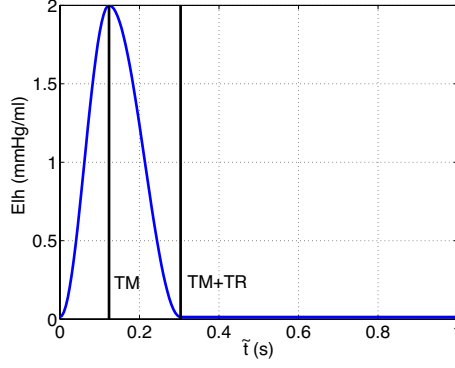
Figure 6.5: Time-varying elastance during a cardiac cycle. The maximum elastance is found at $\tilde{t} = T_M$ and the minimal elastance at $\tilde{t} = T_M + T_R$, while the length of the cardiac cycle $T = 1$ seconds. Values for T_M and $T = 1/H$ are obtained from data.

compartments i and $i+1$. The latter equation is valid since we assume that C_i (ml/mmHg) is constant. This formulation is utilized for the four arterial and venous compartments.

For the pulsatile model, (6.2) describes the change in volume of the left heart. Using a relation similar to (6.1) we get

$$p_{lh} = E_{lh}(V_{lh} - V_{un}), \tag{6.4}$$

where E_{lh} (mmHg/ml) is the left heart elastance (the reciprocal of its compliance) and V_{lh} is the left heart volume. Pumping is achieved by introducing a variable elastance function [34] of the form

$$E_{lh}(\tilde{t}) = \begin{cases} \frac{E_M - E_m}{2}\left(1 - \cos(\frac{\pi \tilde{t}}{T_M}) + E_m\right), & \tilde{t} \le T_M \\ \frac{E_M - E_m}{2}\left(\cos(\frac{\pi(\tilde{t} - T_M)}{T_R}) + 1\right) + E_m, & \tilde{t} \le T_M + T_R \\ E_m, & \tilde{t} \le T \end{cases}$$

where $\tilde{t}$ is the time within a cardiac cycle $T = 1/H$. E_m and E_M denote the minimum and maximum elastance, respectively. For each cardiac cycle elastance is increased for $0 < \tilde{t} < T_M$ and decreased for $T_M < \tilde{t} < T_M + T_R$, while during diastole $T_M + T_R < \tilde{t} < T$ elastance is kept constant at its minimum value. Values for T and T_M are obtained from data, while T_R is a model parameter. The time-varying elastance function is illustrated in Fig. 6.5.

Finally, heart valves are modeled using pressure dependent resistors for which a large resistance R_{cl} represents a closed valve, while a small resistance R_{op} represents an open valve. These are modeled as smooth sigmoidal functions of the form

$$R_v = R_{cl} - \frac{R_{cl} - R_{op}}{1 + e^{-\beta(p_{in} - p_{out})}}, \tag{6.5}$$

where p_{in} and p_{out} denote the pressures in compartments on either side of the valve. For $p_{in} > p_{out}$, $R_v \to R_{op}$ (the valve is open), and when $p_{out} > p_{in}$, $R_v \to R_{cl}$ (the valve closes).

The non-pulsatile heart model is adapted from work by Batzel et al. [66], which followed ideas put forth by Grodins [50]. To model cardiac filling, when the mitral valve is open, we assume that the inflow to the ventricle is dependent upon the difference between the filling pressure and the left ventricle pressure. Using an expression analogous to (6.3) gives

$$\dot{V}_{lh}(t) = \frac{1}{R_{mv,op}}(p_{pv}(t) - p_{lh}(t)), \tag{6.6}$$

where V_{lh} is the ventricular volume at time t after the filling process has started, p_{lh} is the ventricular pressure and p_{pv} is the venous filling pressure both assumed to be constant, and $R_{mv,op}$ is the ventricular resistance to the inflow of blood when the mitral valve is open.

For the relaxed ventricle at $E_{lh} = E_m$, using a volume-pressure relation similar to (6.1) we obtain

$$p_{lh}(t) = E_m(V_{lh}(t) - V_{un}). \tag{6.7}$$

The initial value for (6.6) is given by $V(0) = V_{ES}$, representing the beginning of cardiac filling where the volume of the left ventricle is at its minimum, see Figure 6.6. Substituting (6.7) in (6.6) we have,

$$\dot{V}_{lh}(t) + \frac{E_m}{R_{mv,op}}V_{lh}(t) = \frac{p_{pv}}{R_{mv,op}} + \frac{E_m V_{un}}{R_{mv,op}}. \tag{6.8}$$

Integrating (6.8) and letting $t = t_d$, the time of end-diastole, gives

$$V_{ED} = kV_{ES} + (1 - k)\left(\frac{p_{pv}}{E_m} + V_{un}\right), \tag{6.9}$$

where $k = \exp(-t_d E_m/R_{mv,op})$ and the time of end-diastole is given by $t_d = T - T_M$. Note, a similar calculation cannot be done during the ejection phase where the ventricular pressure, p_{lh} changes with time, see Figure 6.6. Consequently, the Frank-Starling mechanism was used to mimic this portion of the cardiac cycle.

The work in Batzel et al. does not explicitly model the pumping of the heart, but predicts cardiac output Q as a function of venous filling pressure p_{pv}. Their model utilized the complete circulation, including the pulmonary division of the cardiovascular system. As a result, it predicted cardiac output as a function of pulmonary venous pressure, while our current model only encompasses the systemic circulation. Thus, this study predicts cardiac output as a function of systemic venous pressure p_{vu}. The basic assumption concerning cardiac output, i.e. the outflow of blood from the heart, for non-pulsatile flow states that: Given the heart rate H (in strokes
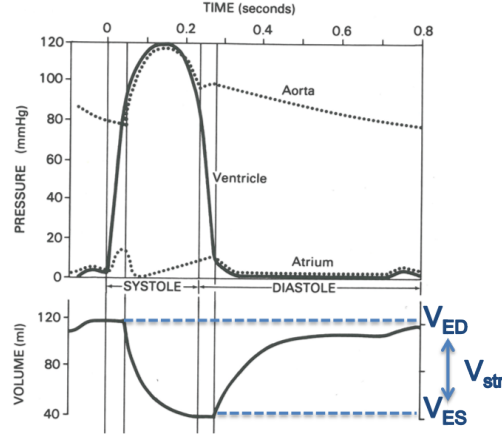
Figure 6.6: Systole and diastole phases of the cardiac cycle. The top picture is of left ventricular pressure, including aorta and atrium pressure waves. The bottom picture depicts the left ventricular volume. The dotted lines represent end-diastolic (V_{ED}) and end-systolic (V_{ES}) volumes, respectively. Stoke volume is also depicted on the figure. Adapted from [130].

per minute) the flow of the left ventricle Q generated by a ventricle is given by

$$Q = HV_{str}, \tag{6.10}$$

where V_{str} is the stroke volume, i.e., the volume of blood ejected during one stroke. The stroke volume is given by

$$V_{str} = V_{ED} - V_{ES}, \tag{6.11}$$

where V_{ED} is the end-diastolic volume and V_{ES} is the end-systolic volume of the heart.

A second assumption involves expressing stroke volume V_{str} as a function of the arterial and venous pressures acting on the ventricle. During the ejection phase of the cardiac cycle the so called Frank-Starling mechanism, also known as Starling's Law [21], is used to account for the fact that the stroke volume increases in response to an increase in the volume of blood filling the heart (the end diastolic volume) when all other factors remain constant. Consequently, increased filling of the ventricle during diastole, causes an increased contraction force during the following systole. This phenomenon can be modeled via

$$V_{str} = \frac{S}{p_a}(V_{ED} - Vun), \tag{6.12}$$

where p_a is the arterial pressure against which the ventricle has to eject (the afterload) and S denotes the contractility of the left ventricle.

85

Using the previous two assumptions the ventricular output Q (the cardiac output) as a function of blood pressure is expressed. Equations (6.9), (6.11) and (6.12) constitute a system of equations for V_{ED}, V_{ES}, and V_{str} of the form

$$V_{ED} = \frac{p_{pv}}{E_m} + V_{un} - \frac{kp_{pv}S}{E_m((1-k)p_a + kS)}, \tag{6.13}$$

$$V_{ES} = \frac{p_{pv}}{E_m} + V_{un} - \frac{p_{pv}S}{E_m((1-k)p_a + kS)}, \tag{6.14}$$

$$V_{str} = V_{ED} - V_{ES} = \frac{(1-k)p_{pv}S}{E_m((1-k)p_a + kS)}. \tag{6.15}$$

Generally, $p_{pv} > p_{vu}$ [130]. To compensate for the difference between the two venous pressures, p_{vu} is multiplied by a constant factor c, $p_{pv} = cp_{vu}$

Subsequenty, combining (6.10) and (6.15) gives the cardiac output out of the ventricle

$$Q = H\frac{acp_vS}{E_m(ap_a + kS)}. \tag{6.16}$$

Using these relations the pulsatile and non-pulsatile differential equations can be written as

$$\frac{dp_{au}}{dt} = ([q_{av}, Q] - q_{al} - q_{aup}) / C_{au}$$

$$\frac{dp_{al}}{dt} = (q_{al} - q_{alp}) / C_{al}$$

$$\frac{dp_{vl}}{dt} = (q_{alp} - q_{vl}) / C_{vl}$$

$$\frac{dp_{vu}}{dt} = (q_{aup} + q_{vl} - [q_{mv}, Q]) / C_{vu}$$

$$\frac{dV_{lh}}{dt} = q_{mv} - q_{av}$$

where

$$q_{aup} = \frac{p_{au} - p_{vu}}{R_{aup}}$$

$$q_{al} = \frac{p_{au} - p_{al}}{R_{al}}$$

$$q_{alp} = \frac{p_{al} - p_{vl}}{R_{alp}}$$

$$q_{vl} = \frac{p_{vl} - p_{vu}}{R_{vl}}$$

$$q_{av} = \frac{p_{lh} - p_{au}}{R_{av}}$$

$$q_{mv} = \frac{p_{vu} - p_{lh}}{R_{mv}}.$$

The pulsatile model terms are in blue, the non-pulsatile terms are in red, and the equations relevant for both models are in black. In the last set of equations the left ventricular pressure (p_{lh}) is predicted using (6.4), the pressure dependent resistances used to model the valves (R_{av}, R_{mv}) are predicted from (6.5), and the total blood volume can be computed from pressures using (6.1). These equations were solved in Matlab using the ODE15s differential equations solver. Abbreviations (subscripts) are explained in Table 6.1.

Modeling HUT & HDT

As the subject is tilted head up (shown in Figure 6.7), blood is pooled in the lower extremities leading to an increase in pressure in the lower body, while pressure in the upper body is decreased. During HDT blood is returned to the upper body decreasing pressure in the legs and increasing pressure in the upper body. Thus to account for gravity, a term representing hydrostatic pressure is added to q_{al}, but subtracted from q_{vl}. The gravitational effects are calculated as described by Olufsen et al. [93, 104], giving the following modified flow equations

$$q = \frac{\rho g h_{tilt} \sin(\theta(t)) + p_{in} - p_{out}}{R},$$ (6.17)

$$\theta(t) = \frac{\pi}{180} \begin{cases} 0 & t < t_{us} \\ v_t(t - t_{us}) & t_{us} \le t < t_{us} + t_{ue} \\ 60 & t_{us} + t_{ue} \le t < t_{ds} \\ -v_t(t - t_{ds}) & t_{ds} \le t \le t_{ds} + t_{de} \\ 0 & t > t_{ds} + t_{de} \end{cases}$$

where ρ (g/ml) is blood density, g (cm/s^2) is the constant of gravitational acceleration, h_{tilt} (cm) is the absolute height between the upper body and lower body compartments, $\theta(t)$ is the

Table 6.1: Abbreviations (subscripts) used in the compartmental model.

Abbreviation	Name
au	upper body arteries
al	lower body arteries
aup	upper body "peripheral" vascular bed
alp	lower body "peripheral" vascular bed
vu	upper body veins
vl	lower body veins
lh	the left heart (ventricle and atrium)
av	aortic valve
mv	aortic valve
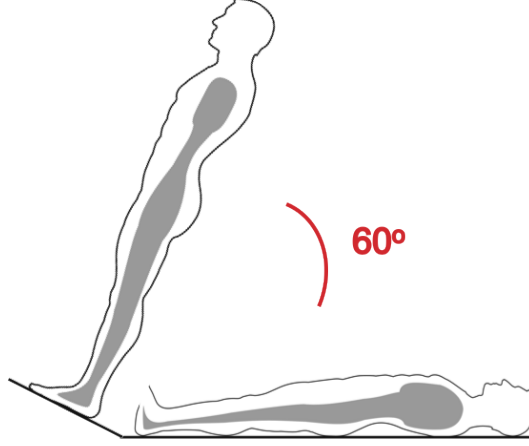
Figure 6.7: The HUT test: The subject depicted is tilted to an angle of 60 degrees at a constant speed of 15 degrees per second. Red and yellow circles indicate the locations for the blood pressure sensors. Each sensor is mounted on the index finger, one finger (red) is placed at the level of the carotid artery, while the other (yellow) is placed at the level of the heart. Upon HUT blood is pooled in the lower extremities.

tilt angle (in radians), $v_t = 15$ degrees/s is the tilt speed, while t_{us}, t_{ue}, t_{ds}, and t_{de} denote the time at which HUT and HDT are started and ended. The combined term $\rho g h_{tilt} \sin(\theta(t))$ denotes the hydrostatic pressure between the upper and lower body compartments.

Modeling effects of cardiovascular regulation

Upon HUT/HDT firing of the baroreceptor nerves are modulated by the aortic and carotid sinus baroreceptors sensing changes in the stretch of the arterial wall. Typically, HUT leads to a decrease in blood pressure mediating an increase in sympathetic outflow along with parasympathetic withdrawal. Sympathetic stimulation elicits changes in vascular resistance and cardiac contractility, while parasympathetic withdrawal primarily has an effect on heart rate and cardiac contractility. HDT elicits the opposite response. Heart rate is used as an input, consequently, parasympathetic heart rate regulation is implicitly accounted for in the model. In the pulsatile model, regulation of cardiac contractility was modeled by allowing the minimum elastance E_m of the left heart and vascular resistance in both the upper R_{aup} and lower body R_{alp} to vary with time. However, the compartments representing the upper and lower body arteries appear in parallel, hence both resistances are not identifiable. Thus, R_{aup} is controlled directly, while we let $R_{alp} = kR_{aup}$, where k is the ratio of the optimized supine values of R_{aup} and R_{alp}.

Similar to [104] we predict R_{aup}, E_m, and S as time-varying quantities by expressing them

as piece-wise linear functions given by

$$X(t) = \sum_{i=1}^{N} \gamma_i K(t), \tag{6.18}$$

$$K(t) = \begin{cases} \dfrac{t - t_{i-1}}{t_i - t_{i-1}}, & t_{i-1} \leq t \leq t_i \\ \dfrac{t_{i+1} - t}{t_{i+1} - t_i} & t_i \leq t \leq t_{i+1} \\ 0, & \text{otherwise} \end{cases}$$

where the unknown coefficients γ_i, $i = 1 \ldots N$ are the new parameters to be estimated to predict the control. N is the number of nodes along the time span analyzed. The spread of the N nodes should be specified in the model. For simulations reflecting dynamics observed in supine position we placed the nodes with a frequency of 6-10 seconds, but during HUT and HDT, where dynamics change, significantly more points are added. It should be noted that the more points are added to the time-span, the longer the simulations.

For the non-pulsatile simulations we investigate three models to regulate contractility:

(M1) Modeling contractility via the Bowditch Effect [77], which states that contractility is proportional to heart rate. The Bowditch effect can be accounted for by introducing the second order ordinary differential equation, of the form

$$\ddot{S} + \gamma \dot{S} + \alpha S = \beta H, \tag{6.19}$$

where γ, α, and β are positive constants and H is heart rate. The second order ODE is then written as two first order equations and those equations are added to the non-pulsatile differential equations given previously. R_{aup} is made time-varying via (6.18) and E_m remains constant.

(M2) Assuming contractility S is a time-varying quantity, but instead of using (6.19), we predict S using (6.18) similar to R_{aup} while E_m remains constant.

(M3) Assuming contractility S to be a model parameter and predicting R_{aup} and E_m as time-varying quantities using (6.18) as done in the pulsatile model.

To compare results of the pulsatile and non-pulsatile models, we modify only the heart compartment parameters, while the other compartments remain identical to their pulsatile counterparts. Comparisons are done using sensitivity analysis, subset selection, and gradient based optimization [75]. More specifically, we estimate a set of model parameters minimizing the least squares error between states computed by the two models. To achieve baseline parameter values while

the subject is in supine position, only parameters that represented differences between the two models (i.e., the heart component) are allowed to vary. Upon modeling HUT and HDT, model parameters representing peripheral resistance and minimum elastance are varied, as was done with the pulsatile model in [99].

Sensitivity analysis

The first step in identifying a subset of parameters to be estimated given available data was to conduct a sensitivity analysis and rank parameters from the most to the least sensitive. For the three models, parameter sets include

$$
\begin{aligned}
\theta_1 &= \{R_{aup}, R_{al}, R_{vl}, R_{alp}, C_{au}, C_{al}, C_{vl}, C_{vu}, E_m, \gamma, \alpha, \beta, c\} \\
\theta_2 &= \{R_{aup}, R_{al}, R_{vl}, R_{alp}, C_{au}, C_{al}, C_{vl}, C_{vu}, E_m, S\}
\end{aligned}
\tag{6.20}
$$

where θ_1 corresponds to contractility model (M1) and θ_2 corresponds to models (M2) and (M3).

The sensitivity matrix is defined as

$$
\chi = \frac{\partial R}{\partial \tilde{\theta}},
\tag{6.21}
$$

where $\tilde{\theta}$ is log-scaled parameters and the residual vector R between computed (y_c) and measured (y_d) quantities is given by

$$
R = \frac{1}{\sqrt{K}} \left[\frac{y_1^c - y_1^d}{y_1^d}, \frac{y_2^c - y_2^d}{y_2^d}, ..., \frac{y_K^c - y_K^d}{y_K^d} \right]^T,
\tag{6.22}
$$

where K is the length of the model output vector defined as

$$
y_i = [x_{i1}, x_{i2}, x_{i3}, \ldots, x_{iM}],
\tag{6.23}
$$

where M is the number of cardiac cycles analyzed. Depending on the specific study $\{x_i\}$ has several quantities. Since the model outputs may contain states with different units, and since the data segments analyzed may vary in length, we scaled the residual by the value of the measurements and by the square root of the number of samples K. Note quantities in y do not depend continuously on time, but represent one value for each cardiac cycle.

Sensitivities were computed using the forward difference approximation

$$
\frac{\partial y_k}{\partial \tilde{\theta}_i} = \frac{y_k(t, \tilde{\theta} + \delta e_i) - y_k(t, \tilde{\theta})}{\delta},
$$

where

$$e_i = \begin{bmatrix} 0 & \dots & 0 & \overset{i}{\widehat{1}} & 0 & \dots \end{bmatrix}^T$$

is the unit vector in the i'th component direction, and $\delta = \sqrt{\xi}$ is the step-size. $\xi = 10^{-8}$ is the integration tolerance used for solution of the dynamical system. A scaled 2-norm

$$\chi_i = \left(\frac{1}{K} \sum_{j=1}^{K} \chi_{i,j}^2 \right)^{1/2}. \tag{6.24}$$

was used to get the total sensitivity, χ_i, to the i'th parameter. Parameters were split into two sets: sensitive and insensitive parameters. The sensitive parameters were subsequently analyzed using subset selection to investigate correlations among parameters.

Subset selection

The set of sensitive parameters from θ_1 and θ_2, were analyzed by computing pair-wise correlations. To do so we use the model Hessian defined by $\mathcal{H} = \chi^T \chi$, where χ is the sensitivity matrix defined in (6.21). Using $\mathcal{H}$ the correlation matrix Ψ was computed as

$$\Psi_{i,j} = \frac{C_{i,j}}{\sqrt{C_{i,i} C_{j,j}}}, \quad C = \mathcal{H}^{-1},$$

where it is symmetric with 1's in the diagonal. All off-diagonal elements have values between $-1 \leq \Psi_{i,j} \leq 1$, values close to 1 indicate that parameters are correlated [104]. It should be noted that Ψ cannot be computed if $\mathcal{H}$ is singular. For the non-pulsatile model, only the parameters corresponding to the heart compartment, (α, β, γ, c) and (S,c) for contractility models (M1) and (M2/M3), respectively were analyzed. $\mathcal{H}$ is analyzed to guarantee nonsingularity, thus Ψ can easily be computed. For either parameters, the entries $\Psi_{i,j}$ are not close to 1, indicating that all parameters in the subsets are identifiable. It should be noted that all analysis methods presented here are local and only valid in a region close to the parameter values investigated, i.e., results may change as the parameters change. To ensure that optimized parameters were not correlated, this analysis should be repeated for the optimized parameter values.

Parameter estimation

Gradient-based optimization [75] was utilized to estimate the set of identifiable model parameters that minimize the least squares error between the measured data and the model. This formulation relies on the assumption that the measurements can be described fully by the

underlying model plus an error term representing the measurement noise, i.e. we assume that

$$y_{d,i} = y_m(t_i; \theta_\rho, \theta_{n-\rho}) + \epsilon_i, \quad i = 1, 2, \ldots, K$$

where K denotes the number of elements in the output vector, θ_ρ are the parameters to be estimated, and $\theta_{n-\rho}$ are the parameters kept at their baseline values. For formulation of the statistical model we assume that the errors ϵ_i are independent identically distributed (iid) random variables with mean $E[\epsilon_i] = 0$, covariance $\text{cov}(\epsilon_i, \epsilon_j) = 0$, and constant variance $\text{var}[\epsilon_i] = \mu^2$. Given this form of the statistical model, the objective function can be defined using the sum of least squares errors

$$\theta_{opt,\rho} = \arg\min_{\theta_\rho} J(\theta)$$

with

$$J(\theta) = R^T R.$$

Note, only parameters in the subset θ_ρ corresponding to the heart compartment will be estimated, while the remaining $\theta_{n-\rho}$ parameters are kept constant at the nominal parameter values. The identifiable parameters θ_ρ were estimated using Levenberg-Marquadt algorithm [75]. Upper and lower bounds were set for all model parameters. For simulations presented here we allowed parameters to increase or decrease by a factor of 4 from nominal parameter values.

6.3   Results

The results are organized as follows:

- First, we show results for the supine simulation where contractility model (M1) parameters include α, β, γ, and c and contractility models (M1) and (M2), only c and S are included in the parameter set.

- Next are results obtained when the same subject is tilted upright to a 60 degree angle (see Figure 6.7). During HUT the parameters estimated are $(\gamma R_{aup,i})$, $(\gamma R_{aup,i}, \gamma S_i)$ and $(\gamma R_{aup,i}, \gamma E_{m,i})$ for contractility models (M1), (M2) and (M3), respectively, corresponding to the piece-wise linear spline function given in (6.18).

- Finally, we extend the time-series to include HDT allowing parameters to vary with time. Parameters estimated are the same as during HUT.

For each event we estimate parameters minimizing the least squares error between the model output and data. To develop two models (pulsatile and non-pulsatile) that can be interchanged, we compute averages over each cardiac cycle and concatenate those values for the quantities $x =$

$\{p_{au,m}, p_{vu,m}, p_{al,m}, p_{vl,m}, CO_m, V_{tot,m}\}$ (Figures 6.2 and 6.3) using supine and HUT pulsatile model outputs predicted in [99]. We then use those quantiities as data for the non-pulsatile model.

6.3.1 Optimization during supine position

First we predict dynamics during supine position, as stated above. These simulations are included to tune the model to the subject studied. For all contractility models, (M1), (M2), and (M3) we minimize the least squares error

$$J = \frac{1}{N} \sum_{i=1}^{N} \left(\frac{x_i^d - x_i^m}{x_i^d} \right)^2, \tag{6.25}$$

where x denotes the states listed above, superscript d refers to the non-pulsatile model data (obtained from the pulsatile model [99] discussed in Section 2.1, and superscript m refers to measurements obtained with the non-pulsatile model.

It should be noted that for supine simulations, since the parameters not associated with the heart compartment represent components common for the two models, they were kept constant at their optimized values from the pulsatile model simulations. Results comparing the pulsatile and non-pulsatile models during steady state are shown in Figure 6.8. This figure shows all pressures, cardiac output, and total blood volume. Each graph shows pulsatile model results from [99], calculated averages over each cardiac cycle predicted from the pulsatile model (black line), computations with the non-pulsatile model using nominal parameters (cyan dashed line), and computations with optimized parameters for the non-pulsatile model (magenta line). Note that for all states the two models agree well. Results shown arre for the contractility model (M1). Simulations with the other contractility models give similar results.

6.3.2 HUT optimization

Once baseline parameters were obtained, HUT was imposed by modifying flows between the upper and lower body as described in (6.18). For these simulations, we only estimate the control parameters $\gamma_{R_{aup,i}}$, $\gamma_{E_{m,i}}$, and/or γ_{S_i} depending on which contractility model is used, i.e., we let the parameters R_{aup}, E_m, and/or S vary in time as in (6.18). Three different cost functions were surveyed to determine which gave the best fit. The first cost only included $x = p_{au,m}$ in (6.25), as we did with HUT in the pulsatile model. The second cost function includes all pressures $x = (p_{au,m}, p_{vu,m}, p_{al,m}, p_{vl,m})$ in (6.25). The third cost function includes $x = (p_{au,m}, p_{vu,m}, p_{al,m}, p_{vl,m}, V_{tot,m}, CO)$, the same quantities included for prediction of steady state simulations with the pulsatile and non-pulsatile models.
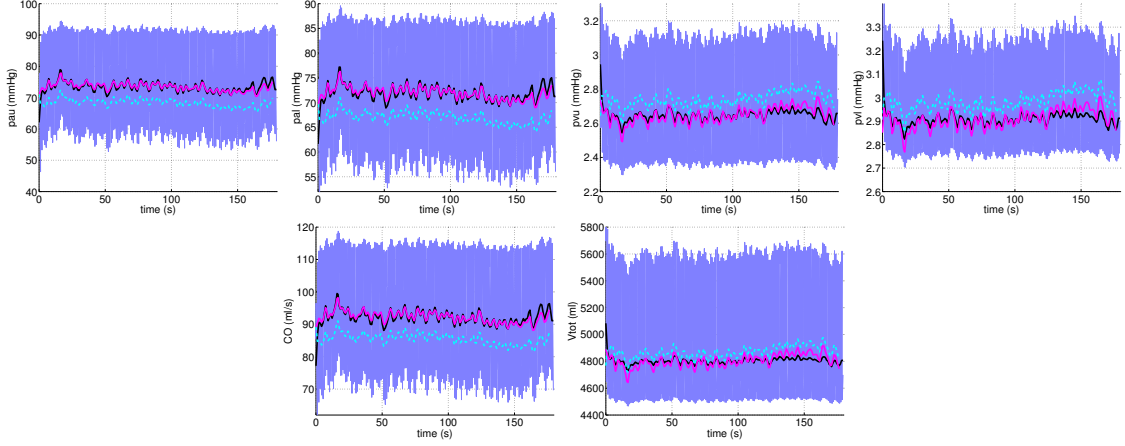
Figure 6.8: Predictions during supine position. All graphs include the pulsatile model output (blue), the calculated mean over each pulse of the pulsatile model output (black), the non-optimized (cyan, dashed) and optimized (magenta) non-pulsatile model output for the upper and lower body arterial pressure p_{au} and p_{al}, upper and lower body venous pressure p_{vu} and p_{vl}, cardiac output CO, and total volume V_{tot}.

For p_{au}, V_{tot}, and CO, Figure 6.9 shows the pulsatile model output (blue), the computed averages from the pulsatile model (black), and results using nominal (cyan dashed) and optimized (magenta) parameter values during HUT with the three different cost functions. Figure 6.10 shows the other pressures as well as the time-varying prediction of peripheral vascular resistance R_{aup} for both the pulsatile (blue) and non-pulsatile (magenta) models comparing the cost functions. The graphs shown use contractility model (M1). The graphs for contractility models (M2) and (M3) gave similar results. The subject is tilted after about 80 sec and remains upright for the duration of the simulation. The top three graphs in Figure 6.9 depict dynamics without activating the control, i.e., for this simulation R_{aup}, is kept at its baseline value. Note that after about 100 sec, this part of the model deviates slightly from results obtained with the pulsatile model. This is likely due to the fact that the non-pulsatile model results already incorporate control of contractility (S) when using (M1), while the "data" obtained from the pulsatile model were obtained using constant contractility values for E_m.

The remaining rows in Figure 6.9 and the graphs depicted in Figure 6.10 show p_{au}, V_{tot}, CO, p_{vu}, p_{al}, p_{vl}, and R_{aup} obtained with the non-pulsatile model using optimized parameter values for each of the different cost functions. Note since the first cost function only includes p_{au}, predictions for p_{au} are significantly closer than for the other states. In other words, no effort was made to account for variation in the remaining states with the first cost function. Through analyzing the comparisons between the several cost functions, we choose the most suitable for our work to be the cost function including all pressures, cardiac output, and total blood volume
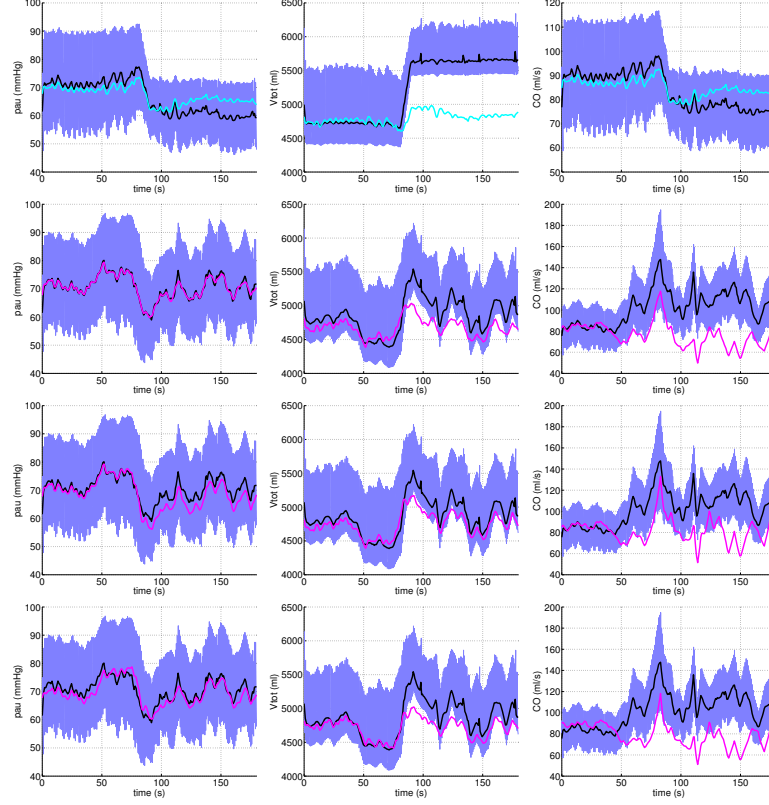
Figure 6.9: Predictions during HUT. Pulsatile (blue), computed averages from pulsatile model (black), non-pulsatile model with nominal (cyan dashed) and optimized (magenta) parameter values. The top row of graphs shows p_{au}, V_{tot}, and CO predicted using nominal parameter values without cardiovascular regulation for the various cost functions. The latter graphs compare the different cost functions for p_{au}, V_{tot}, and CO with cardiovascular regulation. The rows include the cost functions $X = p_{au}$, $X = (p_{au},\ p_{vu},\ p_{al},\ p_{vl})$, and $X = (p_{au},\ p_{vu},\ p_{al},\ p_{vl},\ V_{tot},\ CO)$, respectively.

depicted in the last row of Figure 6.9 and the last column of Figure 6.10. For the analysis in the remainder of this section, we use this cost function, $x = (p_{au},\ p_{vu},\ p_{al},\ p_{vl},\ V_{tot},\ CO)$.

Figure 6.11 depicts results including all pressures, cardiac output, total blood volume and upper body peripheral resistance modeled by the Bowditch Effect (M1) (left), S as a time-varying parameter with E_m remaining constant (M2) (center), and S modeled as a constant parameter with E_m time-varying (M3) (right). The last graph in the right column shows E_m as a time-varying quantity in the pulsatile (blue) and non-pulsatile (magenta) models using (M3). As before, the pulsatile model output (blue), the computed averages from the pulsatile model (black), and results using nominal (cyan dashed) and optimized (magenta) parameter values are shown. Recall, all simulations are now done with the cost function incorporating all

95
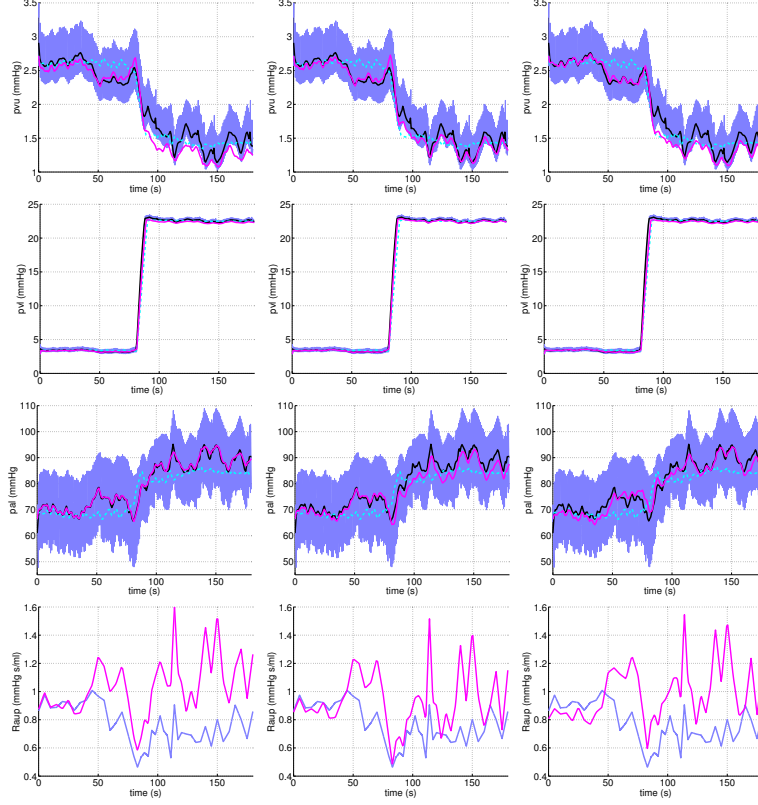
Figure 6.10: Other pressure predictions and R_{aup} during HUT. Again, pulsatile (blue), pulsatile computed averages (black), and non-pulsatile (cyan, dashed) denote simulations with nominal and (magenta) with estimated parameter values. The columns include the cost functions $x = p_{au}$, $x = (p_{au}, p_{vu}, p_{al}, p_{vl})$, and $x = (p_{au}, p_{vu}, p_{al}, p_{vl}, V_{tot}, CO)$, respectively.

pressures, cardiac output and total blood volume. Although all three models provide accurate predictions of p_{au}, prediction of R_{aup} is significantly better when E_m is regulated.

The last figure, Figure 6.12 shows model results when the non-pulsatile estimated time-varying quantities R_{aup} and E_m (i.e. using contractility model M3) are input into the pulsatile model. The graphs show the pulsatile model output for p_{au}, p_{vu}, p_{al}, p_{vl}, V_{tot}, and CO with R_{aup} and E_m estimated in the pulsatile model (blue) and those quantities estimated via the non-pulsatile model (magenta).

6.3.3 HDT Optimization

The HUT simulations are extended on a longer time-scale including data from 110-590 seconds (see the first graph of Figure 6.1) to include HDT dynamics. These simulations include contractility model (M3) only, i.e. R_{aup} and E_m vary with time. The cost function will only

96
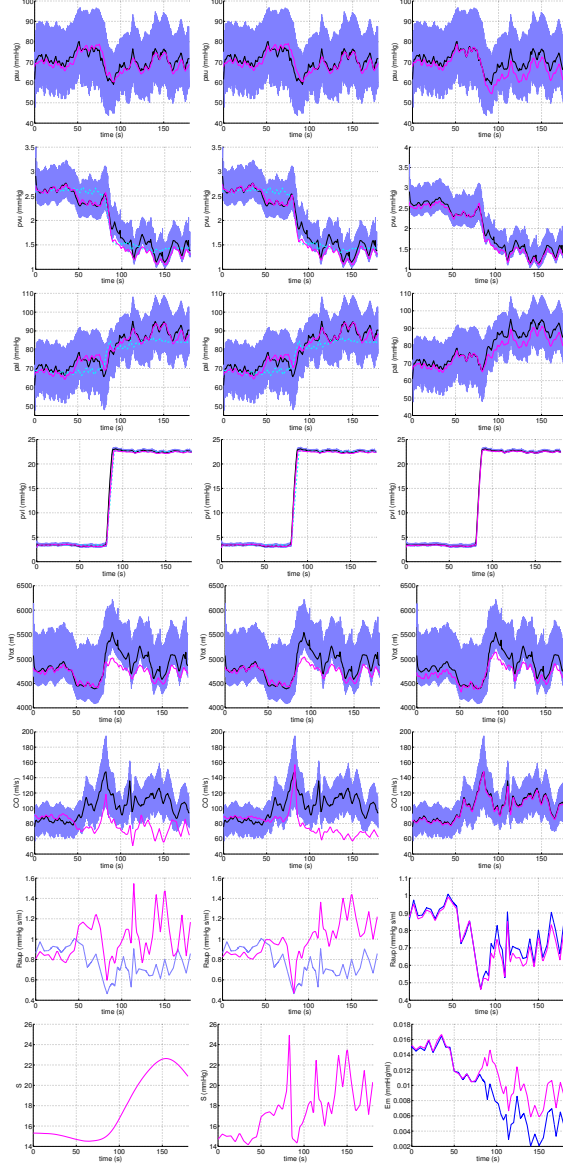
Figure 6.11: S as a Parameter during HUT: The first column depicts simulations using contractility model (M1) where S is modeled using the Bowditch effect and R_{aup} as a time-varying quantity. The second column shows simulations using contractility model (M2) where S and $Raup$ are time-varying quantities and E_m remains constant. The third column shows results using contractility model (M3) where E_m and R_{aup} are time-varying and S is a constant parameter. Again, the graphs show pulsatile (blue), pulsatile computed averages (black), and non-pulsatile simulations with nominal(cyan) and estimated (magenta) parameter values. Graphs shown include p_{au}, p_{vu}, p_{al}, p_{vl}, V_{tot}, CO, R_{aup} and S. We also show E_m as a time-varying quantity for both the pulsatile and non-pulsatile models.
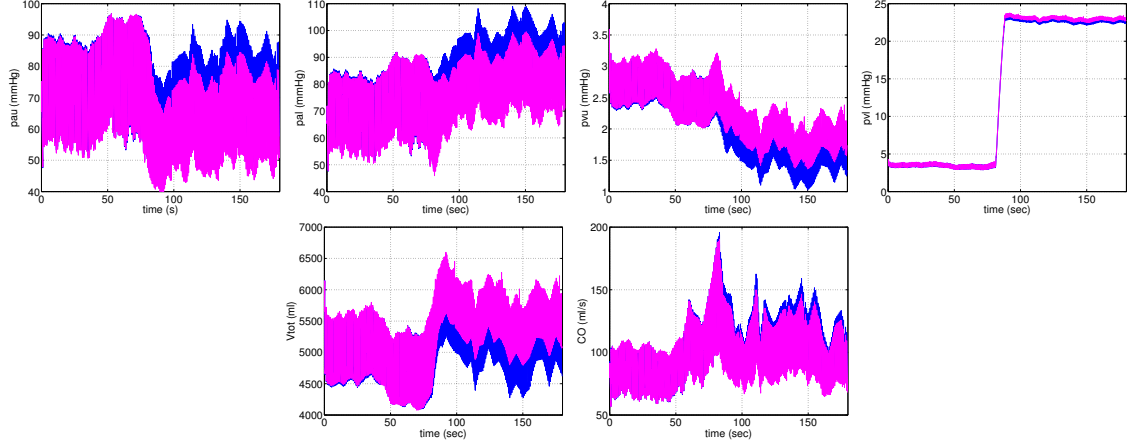
Figure 6.12: Pulsatile predictions during HUT with non-pulsatile model estimates of R_{aup} and E_m. All graphs include the pulsatile model output with the estimated quantities from the pulsatile model (blue) and the non-pulsatile model (magenta) for the upper and lower body arterial pressure p_{au} and p_{al}, upper and lower body venous pressure p_{vu} and p_{vl}, cardiac output CO, and total volume V_{tot}.

include the upper body arterial pressure since we do not have HDT data from the pulsatile model simulations.
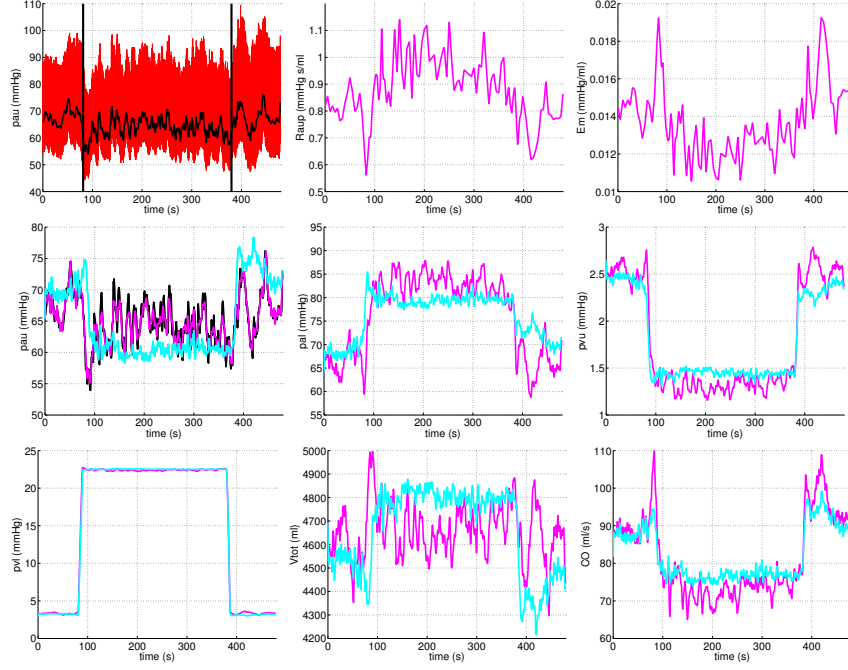
Figure 6.13: Predictions during HUT and HDT with non-pulsatile model estimates of R_{aup} and E_m. The first graph in the top row depicts the carotid blood pressure data (red) and the computed average of that data (black). The vertical lines show the onset of HUT and HDT. The other two graphs in the top row show the controlled quantities R_{aup} and E_m. The remaining graphs include p_{au}, p_{vu}, p_{al}, p_{vl}, V_{tot}, and CO before the control is imposed (cyan) and after the control is implemented (magenta).

Figure 6.13 illustrates model results for HUT and HDT with the non-pulsatile model. The clinical carotid blood pressure data (red) and the concatenated computed averages over each cardiac cycle are shown in the first graph of the top row. The results of the controlled quantities R_{aup} and E_m after optimization are also depicted in the first row. The latter graphs show the results of other quantities p_{au}, p_{vu}, p_{al}, p_{vl}, V_{tot} before R_{aup} and E_m are regulated (cyan) and after (magenta).

6.4 Discussion

This study has shown that it is possible to develop interchangeable pulsatile and non-pulsatile models that can predict dynamics during HUT, and that time-varying parameters (R_{aup}, E_m) can be predicted by both models. To our knowledge this has not been done before. We have also shown that HUT and HDT dynamics can be predicted via the non-pulsatile model. This was done by developing two five-compartment models that use heart rate as an input to estimate

pulsatile and non-pulsatile values of blood flow, pressure, and volume. HUT and HDT were imposed by including gravitational pooling of blood in the legs, and the autonomic response to HUT and HDT was included via time-varying parameters estimating vascular resistance and minimum elastance. Nonlinear optimization was used to estimate the time-varying model parameters.

The non-pulsatile model was compared with calculated concatenated averages from the pusatile model for a healthy young adult (see Figures 6.2 and 6.3). Moreover, we have shown that it is possible to use parameter estimates obtained with the non-pulsatile model within the pulsatile model and obtain similar results (see Figure 6.12). Note, the discrepancy between the two pulsatile outputs after the tilt is most likely due to the discrepancy between the pulsatile and non-pulsatile model estimates of E_m (see Figure 6.11). The non-pulsatile E_m estimate is slightly larger than the pulsatile E_m estimate after the tilt due to the effect of Starling's law providing averaged values for the non-pulsatile heart model.

Having pulsatile and non-pulsatile models that can be interchanged could be applicable to simulations done over long time-scales (min-hours), where it may only be necessary to study pulsatility intermittently, e.g., following given events within the system. The non-pulsatile model is better for longer time-scales because it takes a significant less amount time to predict the cardiac regulation in comparison to the pulsatile model. The pulsatile model took about 48 hours to complete the time-varying quantities estimations, while the non-pulsatile model took about 4 hours. Simulations were performed on a Macbook Pro with a 2.66 GHz Intel Core 2 Duo processor. The non-pulsatile model could also be used for coupling the HUT model with more complex models involving, respiration, renal activity, etc, model that are to be analyzed in future work. Finally, it should be noted that compartments and parameters associated with the arterial and venous subsystems are identical for the two models. The only difference is the compartment predicting dynamics of the left heart.

Results showed (see Figures 6.8 and 6.11), that the non-pulsatile model was able to fit the "data" created from the pulsatile model for the blood pressures as well as total blood volume and cardiac output in supine position and during HUT. We also showed that we could model contractility regulation several ways, but obtain similar results with each method. Another option to be investigated is using the Bowditch effect to model contractility while also allowing E_m to vary with time. As the models show, through regulation of the selected quantities, blood pressure at the carotid bifurcation returns to homeostatic levels after HUT, in line with the notion that the carotid baroreceptors dominate the blood pressure regulation in humans [90, 82]. Moreover, we showed that by representing E_m and R_{aup} by simple functions it is possible to predict general trends in arterial blood pressure for both the non-pulsatile and pulsatile models.

One limit of this study is the use of the Frank-Starling mechanism. Although there has been experiments supporting the assumption that stroke volume of the heart increases in response to

an increase in the volume of blood filling the heart, it is very difficult to actually justify this [21]. The equation given in (6.12) is an empirical equation adapted from [66]. It does not have any real biological significance. In future work, we would like to directly integrate the pulsatile and non-pulsatile models by use the equations involving elastance (6.4) and (6.5) utilized in the pulsatile model, to describe not only the flow coming into the heart (Q or q_{mv}), but the flow coming out of the heart q_{av}.

6.5   Conclusion

In summary, we have developed a non-pulsatile model interchangeable with a pulsatile model and shown that it can be used to predict HUT and HDT dynamics. These models (the pulsatile and non-pulsatile models) have many potential benefits for the study of complex models, which contain a cardiovascular component. The advantage of results presented here is that the non-pulsatile model can be included in applications that require analysis of data over large time-scales and that it is simpler and faster than its pulsatile counterpart .

Chapter 7

Modeling Head-up Tilt via an Optimal Control Approach and a Non-pulsatile Model

Abstract

This chapter presents an optimal control approach to modeling effects of cardiovascular regulation during head-up tilt (HUT). Many patients, who are suffering from dizziness or light-headedness, are often exposed to the head-up tilt test to explore potential deficits within the autonomic control system, which maintains the cardiovascular system at homeostasis. This system is complex and difficult to study in vivo, thus we propose to use mathematical modeling to achieve a better understanding of the cardiovascular regulation system during HUT. In particular, we show the feasibility of using optimal control to predict changes in vascular resistance and cardiac contractility, quantities that cannot be measured directly, but which are useful to assess the state of the cardiovascular system. A non-pulsatile and interchangeable pulsatile model is utilized as well as a direct transcription method to regulate the cardiovascular system.

7.1   Introduction

Short-term cardiovascular responses to orthostatic stress involve complex interactions among various mechanisms of short-term cardiovascular and respiratory blood flow and pressure control. Failure of this system has clinically significant consequences including dizziness, loss of balance leading to collapses, and reflex mediated syncope, in particular for the elderly and for patients with hypertension and diabetes. The underlying pathophysiology leading to regulatory failure is difficult to analyze since the detailed physiology involved with blood flow and pressure

control is not well understood, and it is difficult to study the complex regulatory responses experimentally. These facts suggest that there is a need for the development of a modeling approach to predict blood flow and blood pressure regulation.

Sit-to-stand as well as the more commonly used HUT tests are often used to assess patients ability to regulate blood pressure, in particular for patients who suffer from frequent episodes of syncope, lightheadedness, or dizziness [88]. During the HUT test, the patient rests on a tilt-table in supine position. After steady values for pressure and heart rate are achieved the table is tilted to an angle of 60-70 degrees. Upon tilting, gravity causes pooling of 500-1000 ml of blood in the lower extremities reducing venous return, which induces a reduction in cardiac filling, pressure and volume [64, 121]. As a response, blood pressure in the upper body decreases, while blood pressure in the lower body increases. Baroreceptors located in the carotid sinuses sense the drop in blood pressure causing sympathetic activation and parasympathetic withdrawal, which in turn lead to an increase in heart rate, cardiac contractility and vascular resistance [32].

In this chapter, an optimal control approach is proposed for the regulation of vascular resistance and cardiac contractility to predict dynamics during HUT. Optimal control has mostly been used to model the regulation of drug treatments for a disease, most notably HIV and cancer [29, 57, 100, 114]. Using optimal control to model the regulation of the cardiovascular system is a novel approach. Only a few people have demonstrated this method, however they use optimal control in a very different manner, employing feedback mechanisms. Batzel et al. [68] employed optimal control to study the effects of congestive heart failure on the cardiovascular and respiratory control systems. In this study the goal of the control problem is to model the regulatory mechanisms of the cardiovascular and respiratory systems. The cost function consists of the two control variables, heart rate and the ventilation rate, as well as stabilizing terms for the mean arterial pressure and partial pressure of blood gas in arterial blood for CO_2 and O_2.

Previous efforts to regulate vascular resistance and cardiac contractility used piecewise linear splines with gradient based optimization [99] and Kalman filtering [13]. This method proved to be computationally expensive, as well as requiring *a priori* knowledge of the system for placement of the nodes for the splines. The spread of the nodes were manually specified in the model. During HUT, where dynamics change more frequently, significantly more points were added than in supine position. It should be noted that the more points that are added to the time-span, the longer the optimization simulations. The goal of using optimal control theory is the specification of controlled parameters based on time dependent blood pressure data points. A promising approach for approximating the solution to the optimal control problem is the direct transcription method [35]. This method approximates the original optimal control problem by a discrete optimization problem, an approach often referred to in the literature as "discretize then optimize". In this work, we employed GPOPS (General Pseudo-spectral Optimal Control Software) [12], a MATLAB based optimal control software that implements an adaptive Radau

pseudo-spectral method to transcribe the optimal control problem to a nonlinear programming problem (NLP). The NLP is then solved using either the NLP solver SNOPT or IPOPT. The optimal control solutions from GPOPS are then compared with the results obtained from using the piecewise linear spline approximation.

7.2 Methods

This section describes both the pulsatile and non-pulsatile cardiovascular models as well as the optimal control formulation.

7.2.1 Lumped cardiovascular models

The pulsatile and non-pulsatile cardiovascular models depicted in Figure 7.1 are developed to estimate blood flow, volume, and pressure in the systemic circulation during HUT with and without a pulsating heart. Both models follow the same basic layout shown in Figure 7.1 including compartments representing arteries and veins in the upper and lower body as well as a compartment representing the heart [99]. The latter is the only compartment that differs between the pulsatile and non-pulsatile models.

For each compartment, a pressure-volume relation is given by

$$V_i - V_{un} = C_i(p_i - p_{ext}), \tag{7.1}$$

where V_i (ml) is the compartment volume, V_{un} (ml) is the unstressed volume, C_i (ml/mmHg) is the compartment compliance, p_i (mmHg) is the compartment instantaneous blood pressure, and p_{ext} (mmHg) (assumed constant) is the pressure in the surrounding tissue. For each compartment, we also use a differential equation to predict the change in volume

$$\frac{dV_i}{dt} = q_{in} - q_{out}, \tag{7.2}$$

where q (ml/s) is the volumetric flow. Using a linear relationship analogous to Ohm's law the volumetric flow q (ml/s) between compartments can be computed as

$$q = \frac{p_{in} - p_{out}}{R}, \tag{7.3}$$

where p_{in} and p_{out} are the pressure on either side of the resistor R (mmHg s/ml). Differentiating (7.1), using (7.2), and inserting (7.3) allows us to obtain a system of differential equations in
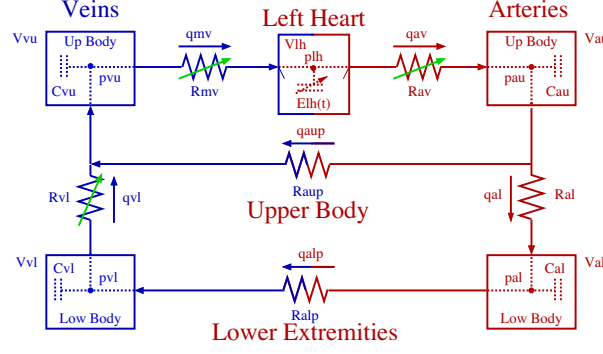
Figure 7.1: Compartment model used for predicting HUT dynamics. For each compartment an associated blood pressure p (mmHg), volume V (ml), and compliance C (ml/mmHg) are defined. The compartments represent the upper body arteries (subscript au), lower body arteries (subscript al), upper body veins (subscript vu), lower body veins (subscript vl), and the left heart (subscript lh). Resistances R (mmHg s/ml) are placed between all compartments: R_{al} denotes the resistance between arteries in the upper and lower body, R_{aup} and R_{alp} denote resistance between arteries and veins in the upper and lower body, respectively. The two heart valves, the mitral valve and the aortic valve, are modeled as pressure dependent resistors R_{mv} and R_{av}. Finally, the resistance between the lower and upper body veins R_{vl} is also modeled as pressure dependent to prevent retrograde flow into the lower-body during the HUT.

blood pressure of the form

$$\frac{dp_i}{dt} = \frac{1}{C_i}\frac{dV_i}{dt} = \frac{1}{C_i}\left(\frac{p_{i-1} - p_i}{R_{i-1}} - \frac{p_i - p_{i+1}}{R_i}\right),$$

where i refer to the compartment for which the pressure p_i is computed, while $i-1$ and $i+1$ refer to the two neighboring compartments. For resistances that appear between compartments, R_{i-1} refer to the resistance between compartments $i-1$ and i, and R_i refer to the resistance between compartments i and $i+1$. The latter equation is valid since we assume that C_i (ml/mmHg) is constant. This formulation is utilized for the four arterial and venous compartments.

The pulsatile heart model is the same used in previous work [98, 99]. The non-pulsatile heart model is adapted from the work by Batzel et al. [66], which followed ideas originally proposed by Grodins [50]. When the mitral valve is open, cardiac filling is modeled by assuming that the inflow into the ventricle depends on the difference between the filling pressure and the left ventricle pressure. Using an expression analogous to (7.3), we have

$$\dot{V}_{lh}(t) = \frac{1}{R_{mv,op}}(p_{pv}(t) - p_{lh}(t)), \tag{7.4}$$

where V_{lh} is the ventricular volume at time t after the filling process has begun, p_{lh} is the

constant ventricular pressure, p_{pv} is a constant representing the venous filling pressure, and $R_{mv,op}$ is the ventricular resistance to the inflow of blood when the mitral valve is open.

For the relaxed ventricle, a similar volume pressure relation can be derived as in (7.1),

$$p_{lh}(t) = E_m(V_{lh}(t) - V_{un}),$$ (7.5)

where V_{un} denotes the unstressed volume of the relaxed ventricle and E_m denotes the minimum elastance of the left heart. The initial value for (7.4) is given by $V_{lh}(0) = V_{ES}$. Using (7.5) in (7.4), integrating, and letting $t = t_d$, the time of end-diastole, we obtain

$$V_{ED} = kV_{ES} + a\left(\frac{p_{pv}}{E_m} + V_{un}\right),$$ (7.6)

where $k = \exp(-t_d E_m/R_{lh})$, $a = 1 - k$ and the time of end-diastole is given by $t_d = T - T_M$, T_M being the time of end-systole.

The Batzel et al. model does not explicitly depict the pumping of the heart, but predicts cardiac output Q as a function of venous filling pressure p_{pv}. The original model was used with both the systemic and pulmonary circulations. It predicted cardiac output as a function of pulmonary venous pressure, the current model only encompasses the systemic circulation, and consequently this study predicts cardiac output as a function of systemic venous pressure p_{vu}.

The general assumption concerning cardiac output, i.e., the outflow of blood from the heart, for non-pulsatile flow states that: Given the heart rate H (in strokes per minute) the flow of the left ventricle Q is given by

$$Q = HV_{str},$$ (7.7)

where V_{str} is the stroke volume, i.e., the volume of blood ejected during one stroke. As a result time varying quantities in the non-pulsatile model are to be interpreted as averages over the length of a pulse. The stroke volume is given by

$$V_{str} = V_{ED} - V_{ES},$$ (7.8)

where V_{ED} is the end-diastolic volume and V_{ES} is the end-systolic volume of the heart. Another assumption involves expressing stroke volume V_{str} as a function of the arterial and venous pressures acting on the ventricle. Concerning the ejection phase of the heart cycle we invoke the so called Frank-Starling mechanism [21], which states that the stroke volume of the heart increases in response to an increase in the volume of blood filling the heart (the end diastolic volume) when all other factors remain constant. Consequently, increased filling of the ventricle during diastole, causes an increased contraction force during the following systole. Frank-Starling

mechanism is modeled as

$$V_{str} = \frac{S}{p_a}(V_{ED} - V_{un}),\tag{7.9}$$

where p_a is the arterial pressure against which the ventricle has to eject (the afterload) and S denotes the contractility of the left ventricle.

Using the previous two assumptions we express the ventricular output Q (the cardiac output) as a function of blood pressure. Equations (7.6), (7.8) and (7.9) constitute a system of equations for V_{ED}, V_{ES}, and V_{str} of the form

$$V_{ED} = \frac{p_{pv}}{E_m} + V_{un} - \frac{kp_{pv}S}{E_m(ap_a + kS)},\tag{7.10}$$

$$V_{ES} = \frac{p_{pv}}{E_m} + V_{un} - \frac{p_{pv}S}{E_m((1-k)p_a + kS)},\tag{7.11}$$

$$V_{str} = V_{ED} - V_{ES} = \frac{(1-k)p_{pv}S}{E_m((1-k)p_a + kS)}.\tag{7.12}$$

Recall that our model does not include both the systemic and pulmonary circuits, thus we do not have a component for venous filling pressure p_{pv}. The incoming pressure into the ventricle in this model is the upper body venous pressure p_{vu}. Generally, $p_{pv} > p_{vu}$ [130]. To compensate for the difference between the two venous pressures, p_{vu} is multiplied by a constant factor c, $p_{pv} = cp_{vu}$. Subsequently, combining (7.7) and (7.12) gives the cardiac output out of the ventricle

$$Q = H\frac{(1-k)cp_vS}{E_m((1-k)p_a + kS)}.\tag{7.13}$$

7.2.2 Optimal control formulation

The objective of our control problem is to regulate vascular resistance and elastance during HUT. For the cost functional we computed averages over each cardiac cycle of p_{au}^d, p_{vu}^d, p_{al}^d, p_{vl}^d, CO^d and V_{tot}^d, from the pulsatile model output predictions in Williams et al. [4], and joined these averages together to be used as data. For the steady state, we employed the cost functional (**G1**)

$$J = 10^2\left[\left(\frac{p_{au}^m - p_{au}^d}{p_{au}^d}\right)^2 + \left(\frac{p_{vu}^m - p_{vu}^d}{p_{vu}^d}\right)^2 + \left(\frac{p_{al}^m - p_{al}^d)}{p_{al}^d}\right)^2 + \left(\frac{p_{vl}^m - p_{vl}^d)}{p_v l^d}\right)^2\right]$$
$$+ 10^2\left(\frac{CO^m - CO^d}{CO^d}\right)^2 + 10^2\left(\frac{V_{tot}^m - V_{tot}^d}{V_{tot}^d}\right)^2 + R_{aup}^2 + E_m^2,\tag{7.14}$$

where superscript d refers to the averages (computed from the predictions of the pulsatile model) used as data and m refers to the non-pulsatile model quantities. Here, the control variables are

the vascular resistance R_{aup} and the minimum elastance E_m, both included in the cost. We want the dynamics to fit the data more than we would like to minimize the control variables, thus a weight of 10^2 is multiplied by the terms in the cost function involving data.

For HUT we have a cost functional of the form

$$J = 10^2 \left(\frac{p_{au}^m - p_{da}^d}{p_{da}^d} \right)^2 + R_{aup}^2 + E_m^2, \tag{7.15}$$

where p_{da} is the pulsatile blood pressure data gathered by clinicians used with the pulsatile model in [99]. The superscript m is included because an average is computed over each cardiac cycle and those values are concatenated together, the same procedure done to create the "data" for the non-pulsatile model using the pulsatile model simulations.

We employed GPOPS, an open-source MATLAB optimal control software that implements the Radau pseudo-spectral method (RPM). In a pseudo-spectral method, the states and controls are approximated using global polynomials, and collocation of the differential-algebraic equations (the right hand side of the system of ODEs) is achieved at orthogonal collocation points (i.e. the collocation points are the roots of an orthogonal polynomial and/or a linear combination of an orthogonal polynomial and its derivatives). In particular, GPOPS approximates the states and controls using a basis of Lagrange-Gauss-Radau points. The continuous-time optimal control problem is then transcribed to a finite-dimensional nonlinear programming problem (NLP) and the NLP is solved using well-known software tools [11]. Features of the RPM include: (1) it is a Gaussian quadrature implicit integration scheme; (2) it has been shown to converge exponentially fast for problems with smooth solutions; (3) the initial boundary is able to be obtained unlike in other pseudo-spectral methods (e.g. Gauss pseudo-spectral method (GPM) and Lobatto pseudo-spectral method (LPM)); (4) the implementation is significantly less complex [12, 46]. The bounds on the states and controls for the steady-state and tilt portions for GPOPS are given in Tables 7.1 and 7.2, respectively. These values were chosen by referencing results from previous work [99, 4].

Table 7.1: Steady-state bounds for GPOPS

Quantity	Start lower bound	During lower bound	End lower bound	Start upper bound	During upper bound	End upper bound
p_{au}	71.1	68	68	71.1	80	80
p_{vu}	2.6	2	2	2.6	3	3
p_{al}	69.7	68	68	69.7	80	80
p_{vl}	2.9	2.7	2.7	2.9	3	3
R_{aup}	0.75	-	0.75	0.95	-	0.95
E_m	0.005	-	0.005	0.02	-	0.02

Table 7.2: Tilt bounds for GPOPS

Quantity	Start lower bound	During lower bound	End lower bound	Start upper bound	During upper bound	End upper bound
p_{au}	67.8	50	50	67.8	100	100
p_{vu}	2.6	0.3	0.3	2.6	3.5	3.5
p_{al}	66.4	50	50	66.4	115	115
p_{vl}	2.9	1	1	2.9	25	25
R_{aup}	0.2	-	0.2	1.1	-	1.1
E_m	0.005	-	0.005	0.017	-	0.017

The optimal control approach is used exclusively on the non-pulsatile model with simulated data generated from the pulsatile model as described in [4]. The pulsatile model output for the pressures, total volume, and cardiac output where averaged over each cardiac cycle and those values concatenated together to form data. The control variables include the upper body peripheral resistance R_{aup} and the minimum elastance E_m, which are quantities in both the non-pulsatile and pulsatile models. The control variables change on a slower time-scale when compared to the time-scale of the pulsatile model, hence making it infeasible to find simultaneous solutions for the state equations and the control variables. Furthermore, the differences in time-scales for the state dynamics and the control variables stem from the fact that the con-

trols try to resolve dynamics within a single beat rather than between beats as in the pulsatile model. As a result, with the pulsatile model, an abundance of collocation points are needed to solve the optimal control problem effectively. The more collocation points used, the longer the simulation. Consequently, the problem would need to be solved in several phases when using GPOPS to expedite the computation time. However, since the non-pulsatile and pulsatile models are interchangeable, the optimal control solutions using the non-pulsatile model can be utilized within the pulsatile model to predict R_{aup} and E_m thus eliminating the need for piece-wise linear splines and gradient based optimization.

7.3   Results

We first show results obtained for a subject in supine position followed by results obtained when the same subject was tilted upright to a 60° angle. The first set of HUT results are to validate the optimal control method given all the data available. The second set of HUT results show the potential of the method when used without the pulsatile model (i.e. averaged quantities of the actual clinical data is used only). Predictions from our previous work were obtained using a piece-wise linear spline model, hence between consecutive points, the model predictions are given by straight lines. By adapting the control to predict results from piecewise linear splines some bias may be introduced, since biologically, the parameters vary nonlinearly, rather than linearly [130].

7.3.1   Steady-state

Dynamics during supine position were predicted initially to test that the method is applicable for baseline values. The cost function in (7.14) is used.
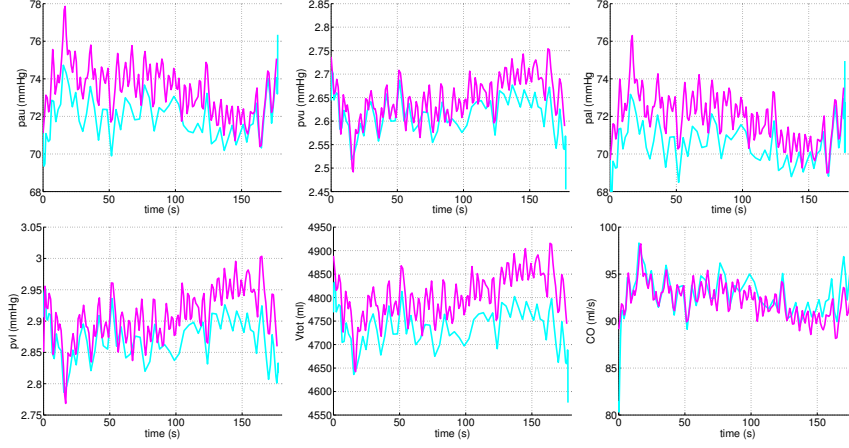
Figure 7.2: Predictions during supine position. All graphs include the pulsatile model output using piecewise linear splines (magenta), and the optimal control output using GPOPS (cyan) for upper body arterial pressure, p_{au}, upper body venous pressure p_{vu}, lower body arterial pressure p_{al}, lower body venous pressure p_{vl}, total blood volume V_{tot} and the cardiac output CO.

Figure 7.2 depicts the output from the pulsatile model (magenta) as described previously versus the non-pulsatile dynamics from GPOPS (in cyan) for p_{au}, p_{vu}, p_{al}, p_{vl}, V_{tot}, and CO. As expected, the non-pulsatile model dynamics with the optimal control agree well with the averaged dynamics from the pulsatile model. Furthermore, the control variables, R_{aup} and E_m, are relatively constant, following the assumption that they are inactive at rest.

7.3.2   Head-up tilt: validation

During HUT, Figure 7.3 depicts results using the same cost function as the supine simulation in (7.14) including all available data, where the non-pulsatile dynamics with R_{aup} and E_m are predicted from the piece-wise linear spline method (blue) and with GPOPS (cyan). This figure includes dynamics of p_{au}, p_{vu}, p_{al}, p_{vl}, CO, V_{tot}. We also show R_{aup} and E_m predicted using the piece-wise linear spline method compared with those quantities predicted by GPOPS. We see that the results obtained with piece-wise linear splines agree well with those of the optimal control method.

Figure 7.3: Predictions during HUT with cost function (7.14). All graphs include the non-pulsatile model output using piecewise linear splines (magenta), and the optimal control output using GPOPS (cyan) for upper body arterial pressure, p_{au}, upper body venous pressure p_{vu}, lower body arterial pressure p_{al}, lower body venous pressure p_{vl}, total blood volume, V_{tot} and the cardiac output CO. Also shown are the control variables upper body peripheral resistance R_{aup} and E_m computed from the optimal control approach via GPOPS (cyan) compared against the piecewise linear spline approach (magenta) in the non-pulsatile model.

An eventual goal of this work is to be able to use predictions of the controlled quantities using GPOPS in the pulsatile model. Figure 7.4 shows model results when the optimal control predicted time-varying quantities R_{aup} and E_m, using cost function (7.14) with all available data, are input into the pulsatile model. The graphs show the pulsatile model output for p_{au}, p_{vu}, p_{al}, p_{vl}, V_{tot}, and CO with R_{aup} and E_m estimated in the pulsatile model (blue) and those quantities estimated via the optimal control approach (cyan).

7.3.3 Head-up tilt

An aim for this study was to be able to use the non-pulsatile model and the optimal control method without using any averaged "data" created from the pulsatile model. We would like to instead be able to use the clinical pulsatile blood pressure data only. Thus the cost function 7.15 is utilized.

Figure 7.5 depicts the same dynamics as Figure 7.3 but using the cost function in (7.15). As shown, this cost functional does not yield accurate dynamics for CO. One way to rectify this issue is to include CO in the cost functional (7.15) as in

$$J = 10^2 \left[\left(\frac{p_{au}^m - p_{da}^d}{p_{da}^d} \right)^2 + \left(\frac{CO^m - CO^d}{CO^d} \right)^2 + \left(\frac{V_{tot}^m - V_{tot}^d}{V_{tot}^d} \right)^2 \right] + R_{aup}^2 + E_m^2. \qquad (7.16)$$
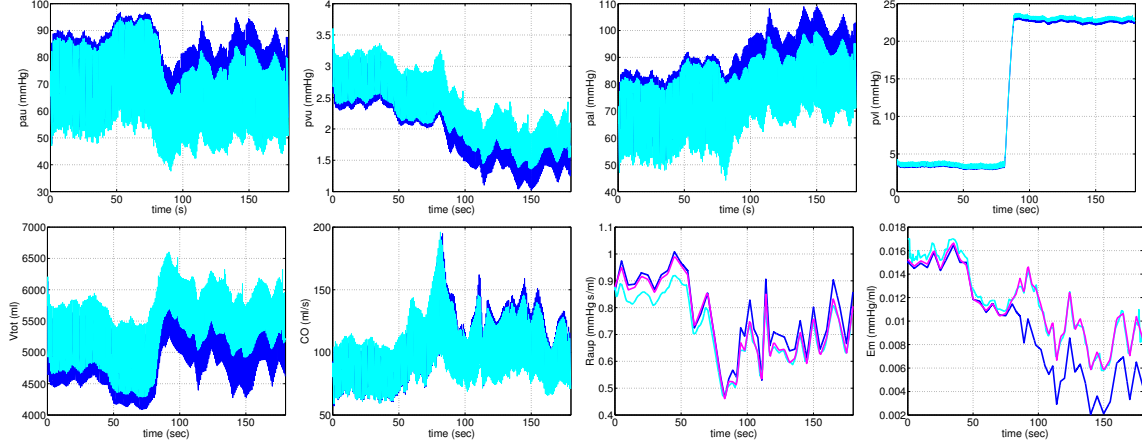
Figure 7.4: Pulsatile predictions during HUT with optimal control estimates of R_{aup} and E_m with cost function (7.14). All graphs include the pulsatile model output (blue) with R_{aup} and E_m predicted from the pulsatile model compared with those quantities predicted from the optimal control approach (cyan) for the upper body arterial pressure, p_{au}, the upper body venous pressure p_{vu}, the lower body arterial pressure p_{al}, the lower body venous pressure p_{vl}, total blood volume V_{tot} and the cardiac output CO. Also shown are predicted quantities R_{aup} and E_m for the pulsatile model simulation (blue) and from GPOPS (cyan).

Figure 7.6 depicts results with (7.16). It shows the same graphs as in the previous three figures, illustrating that the optimal control approach (cyan) now follows the piece-wise linear spline method (magenta) with cardiac output and total blood volume now in the cost functional. As in the previous section, we want to analyze the pulsatile results with the GPOPS predicted time-varying quantities R_{aup} and E_m. These results are depicted in Figure 7.7 with several cost functions including (7.15) and (7.16) among them.

7.4 Discussion and conclusions

This study shows that it is feasible to use an optimal control approach to predict time-varying quantities within cardiovascular regulation. The optimal control approach yields similar results to previous work [4, 99] using a piece-wise linear spline approach and Kalman filtering [13], however our method proved to be favorable in several ways. First, utilizing optimal control is more advantageous since there is no need to have in depth knowledge of the system before hand. Second, the computation time is significantly decreased with this method. With the optimal control approach, we are able to specify the controlled parameters based on time dependent blood pressure data points in less than triple the amount of time as the piecewise linear spline approach on a Macbook Pro with a 2.66 GHz Intel Core 2 Duo processor. Third, we have also
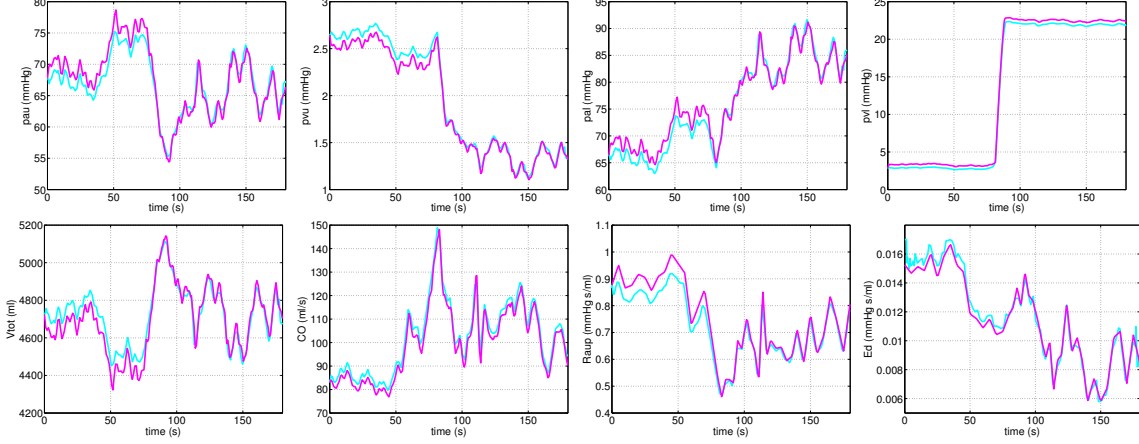
Figure 7.5: Predictions during HUT with cost function (7.15). All graphs include the non-pulsatile model output using piecewise linear splines (magenta), and the optimal control output using GPOPS(cyan) for upper body arterial pressure, p_{au}, upper body venous pressure p_{vu}, lower body arterial pressure p_{al}, lower body venous pressure p_{vl}, total blood volume, V_{tot} and the cardiac output CO. Also shown are the control variables upper body peripheral resistance R_{aup} and E_m computed from the optimal control approach via GPOPS (cyan) compared against the piecewise linear spline approach (magenta) using the non-pulsatile model.

shown that although the optimal control method is suitable for use with a non-pulsatile model, results can be embedded in a pulsatile model rendering accurate dynamics. Optimal control methods have predominately been used in mathematical models of cancer or HIV treatments [29, 57, 100, 114]. The use of optimal control to regulate time-varying quantities to study the control of the cardiovascular system is a novel approach. To our knowledge, Batzel and Kappel [66] are the only researchers to have used optimal control to study cardiovascular dynamics. However, they use the method in a very different manner than what we have proposed.

Figures 7.2 and 7.3 validate that predicting R_{aup} and E_m with an optimal control approach using GPOPS can render almost equivalent dynamics for HUT, compared to using a piece-wise linear spline approach coupled with gradient-based optimization. As discussed, the quick time-scale of the pulsatile model depicting beat-to-beat dynamics is incompatible with the slower control variables modeling dynamics over an average heart beat within the optimal control approach. However, Figures 7.4 and 7.7 illustrate that it is feasible to use optimal control with a simple non-pulsatile model to analyze dynamics for a more complex pulsatile model and yield accurate dynamics.

It is important to note that cardiac output data is essential to ensure accurate model dynamics during HUT as discussed in Ellwein [34]. To ensure accurate cardiac output estimates it is necessary to either include measurements of cardiac output in the cost function or to predict
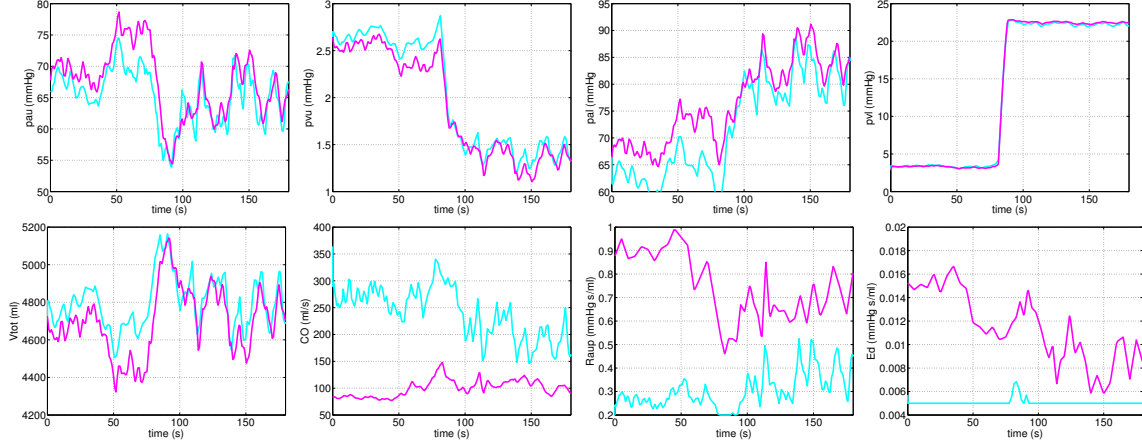
114
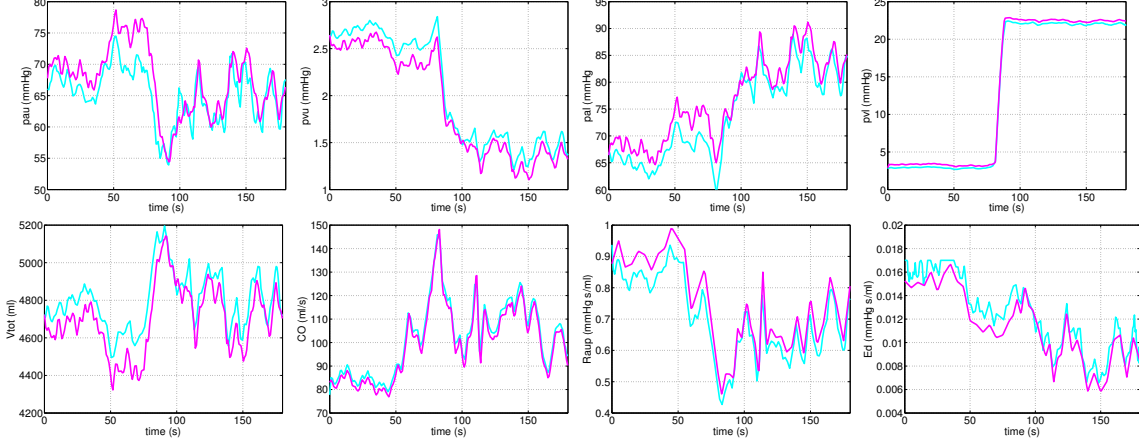
Figure 7.6: Predictions during HUT with cost function (7.16). All graphs include the pulsatile model output using piecewise linear splines (magenta), and the optimal control output using GPOPS (cyan) for upper body arterial pressure, p_{au}, upper body venous pressure p_{vu}, lower body arterial pressure p_{al}, lower body venous pressure p_{vl}, total blood volume, V_{tot} and the cardiac output CO. Also shown are the control variables upper body peripheral resistance R_{aup} and E_m computed from the optimal control approach via GPOPS (cyan) compared against the piecewise linear spline approach (magenta).

cardiac output from the blood pressure measurements as proposed in Wesseling et al. [76] and Parklikar et al. [133]. Comparing Figures 7.5 and 7.6, we see that prior to cardiac output being added to the cost function, it is over-predicted, but once it is included, dynamics appear accurate. In future work it would be interesting to see what other data (e.g. venous upper or lower body pressure, total blood volume) can be included to yield improved prediction of the time-varying quantities. A preliminary analysis of this has been done by considering various components in the tilt cost function and observing the results when input into the pulsatile model. Considering Figure 7.7, it is clear that cardiac output is necessary to give accurate dynamics.

Figure 7.6 shows results without using the pulsatile model. This shows that the optimal control method has the ability to predict forward simulations without having to use a more complex model. The significance of this is now having the option to analyze longer time-scales for both models, thus enabling us to better understand the cardiovascular system during the entire tilting procedure, including tilting back down to supine position. Moreover, being able to explore longer time-scales allows the models to be coupled with larger and more complex systems such as the respiratory or renal systems, which function at time-scales of minute-hours rather than seconds-minutes [80].

Note that any discrepancy between model predictions involving the pulsatile model and

GPOPS may arise due to the fact that GPOPS is utilized with the non-pulsatile model which differs from the pulsatile when modeling the heart compartment. The use of the Frank-Starling mechanism within the non-pulsatile model involves a cardiac contractility parameter S that is not present with the pulsatile model. The coupling of the parameter S and E_m together as in (7.13) causes a variation in predictions of the controlled quantities. Thus, causing variations in the outputs between the pulsatile model with piece-wise linear splines and the pulsatile model with the GPOPS predictions. This is one limitation to our model. See Chapter 7 for a more in depth explanation. Another limitation to this work is the sensitivity to the upper and lower bounds on quantities needed to utilize GPOPS. A value for a specific parameter or state bound is chosen for biological reasons, however numerically that value may disrupt the calculation of the solution to the optimal control problem, in turn leading GPOPS to be unable to find an optimal solution for the problem or causing the simulation time to increase. Thus, it is important to understand the dynamics of the system and find a balance between the biological significance and the numerical computation.
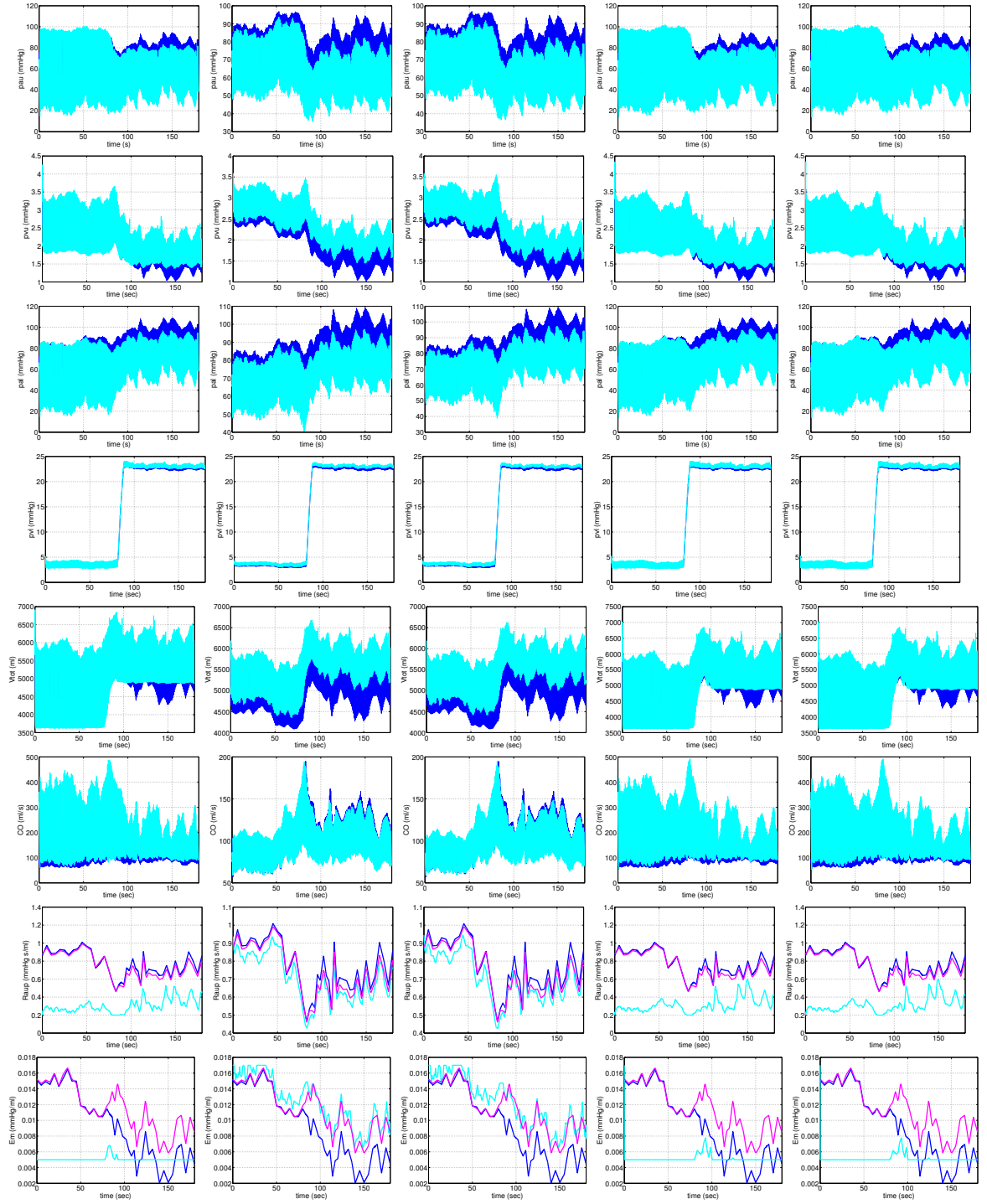
Figure 7.7: Pulsatile predictions during HUT with optimal control estimates of R_{aup} and E_m. The columns are with cost functions (7.15), (7.16), (7.15) with CO, (7.15) with pvu, and (7.15) with pvu, pal, pvl, respectively.

Chapter 8

Simulations and Predictions

This chapter presents pulsatile model predictions illustrating the effect of certain drugs mentioned in the Introduction used by clinicians to treat patients with OI. Recall that through regulation of the cardiovascular control system by the baroreceptors, blood volume, arterial blood pressure, vascular resistance, and compliance are effected during HUT. The drugs effect the sympathetic nervous system to adjust blood volume and promote vasoconstriction, thus having an effect on the efferents mentioned.
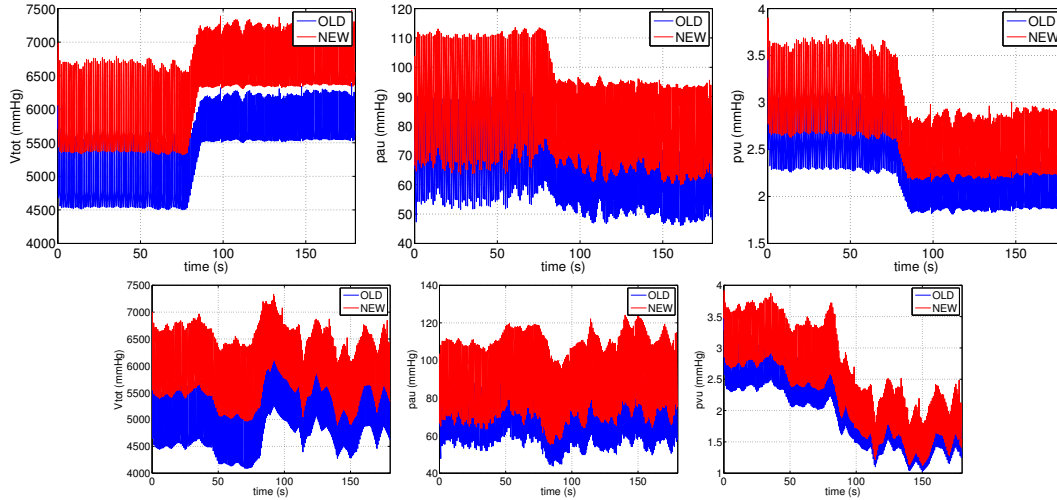
Figure 8.1: Increased Total blood volume. Resulting upper body arterial pressure and upper body venous pressure before the increase in volume (blue) and after the change in volume (red). The top row is without control, while the bottom row is with control.

Desmopressin increases water absorption in the kidneys leading to increased blood volume. Recall that during HUT, upper body arterial blood pressure falls and patients with OI have difficulty raising it back to homeostasis. When blood volume is increased, blood pressure is increased. To simulate this with the pulsatile model, the total blood volume V_{tot} is increased by increasing the blood volume in the heart V_{lh}. Figure 8.1 shows the results on upper body arterial and venous pressures when total blood volume is increased with (bottom row) and without control (top row). The dynamics before the change in volume are in blue, while those after the change are in red. Results show the blood pressures does indeed increase when blood volume is increased illustrating the effect of Desmopressin on the cardiovascular system.

Figure 8.2: Increased peripheral resistance. Resulting upper body arterial pressure, upper body venous pressure, and total blood volume before the increase in resistance (blue) and after the change in resistance (red). The top row is without control, while the bottom row is with control.

Drugs like midodrine and phenylpropanolamine cause vasoconstriction (increase peripheral vascular resistance and decrease venous capacitance) which help to decrease venous pooling by increasing upper body arterial pressure. To simulate this with the pulsatile model, upper body peripheral resistance is increased, see Figure 8.2 and lower body venous compliance is decreased, see Figure 8.3. These figures show the increase in the upper body peripheral resistance and decrease of compliance, respectively, resulting in an increase in upper body arterial pressure, decrease in venous pressure, and a decrease in volume. Thus these simulations depict accurately the effect of Midodrine and phenylpropanolamine on the cardiovascular system.
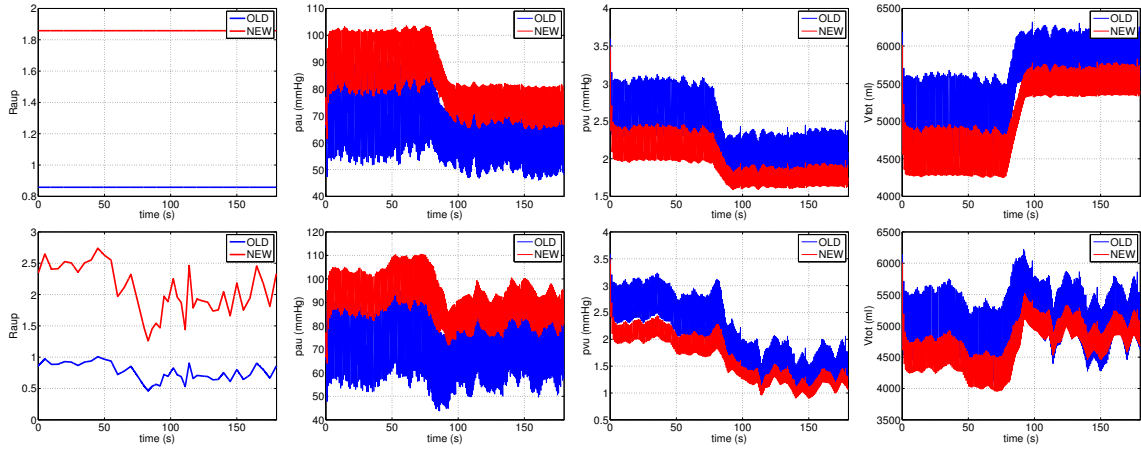
119
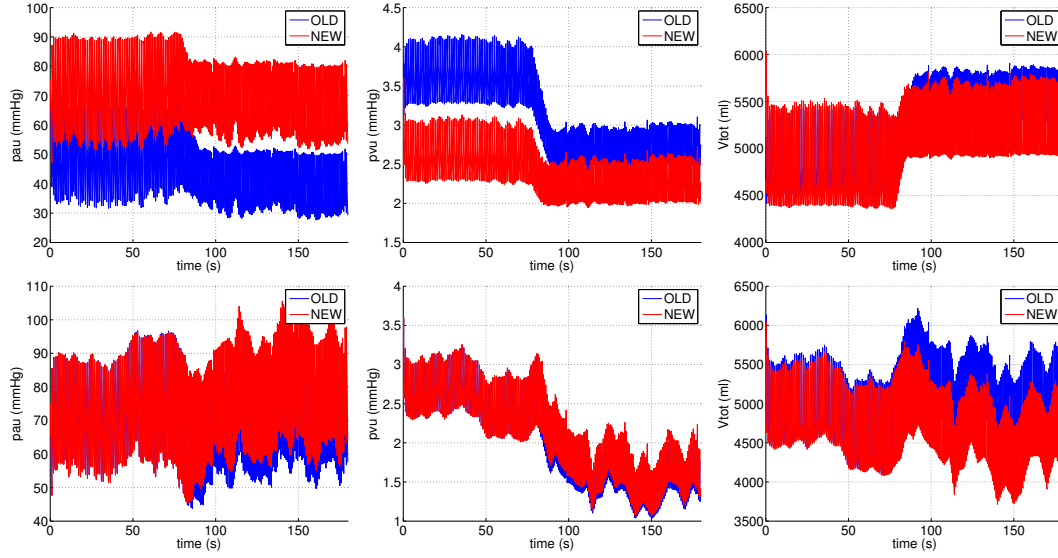
Figure 8.3: Decreased lower body venous compliance. Resulting upper body arterial pressure, upper body venous pressure, and total blood volume before the increase in resistance (blue) and after the change in resistance (red). The top row is without control, while the bottom row is with control.

Chapter 9

Closing Remarks

9.1 General Conclusions

Chapter 5 of this work presented a pulsatile cardiovascular model constructed to predict blood pressure and flow dynamics during HUT and regulate peripheral resistance and cardiac contractility using a piecewise linear spline approach. This study showed how to estimate constant parameters and regulate time-varying quantities permitting the model to fit data measured at the level of the carotid artery. In addition, it is shown how carotid pressure can be calculated from data measured at the level of the aorta and that complementary parameter estimates are obtained comparing model outputs with the measured and calculated carotid pressures.

The work in Chapter 6 presented a comparison between a non-pulsatile model and pulsatile model that can predict dynamics during HUT and HDT. The non-pulsatile model development is described in detail demonstrating advantages and disadvantages in comparison to the pulsatile model. This study showed that results predicted with the non-pulsatile model can be integrated into the pulsatile model in the study of HUT dynamics using the least-squares optimization method to predict time-varying quantities. We also describe how the non-pulsatile model can be used for longer time scales to include HUT/HDT dynamics.

Chapter 7 illustrates how optimal control can be used with the non-pulsatile model to predict time-varying quantities, peripheral resistance and cardiac contractility. Model results were compared to the piecewise linear spline approach presented in Chapters 6 and 7. The implementation of the optimal control approach results into the pulsatile model are described and advantages and disadvantages are discussed.

9.2 Future Work

While this work represents a novel approach to regulating time-varying quantities when studying the cardiovascular control system during head-up tilt, future work is also of importance. This dissertation focused on cardiovascular regulation on a short-time scale. In actuality, there is a longer time scale to consider involving the renal system. The work done here using optimal control can be utilized in models that invoke a longer-time scale to study the effects of tilting on the cardiovascular system of subjects with orthostatic intolerance.

A goal of studying OI is to be able to illustrate what parameters are of importance to a specific patient no matter the age or health of the individual. Thus, more studying can be done on OI and HUT with data sets of various groups comparing patients' with varying ages and healthy anomalies. Moreover, predictions using the models presented in this thesis can be simulated to help clinicians understand what treatments can be affective as seen in Chapter 8.

Further research can be established on the use of optimal control with only using a pulsatile model. This proved to be difficult in our study, however, it would be beneficial to be able to use the actual pulsatile data available to clinician to make predictions without having to alter it in any way. Additionally, more study can be done on designing a model using optimal control that has closed-loop properties being that the cardiovascular system is a closed network.

REFERENCES

[1] *T.A. Goers, M.E. Klingsensmith, L.E. Chen and S.C. Glasgow.* Wolters Kluwer Health/Lippencott Williams & Wilkins, Philadelphia, 2008.

[2] *Quantitative Human Physiology: An Introduction.* Academic Press, Massachusetts, 2012.

[3] Diagram of the human heart, 2013.

[4] 3rd Int Conf on Simulation and Modeling Meth, Tech, and Appl. *Cardiovascular dynamics during head-up tilt assessed via a pulsatile and non-pulsatile model*, 2013.

[5] 8th IFAC Wkshp on Control Applications of Nonlinear Programming and Optimization. *Solution of the optimal control problem using the software package STOPM*, 1989.

[6] A. Capaldi A. CIntron-Arias, H.T. Banks and A.L. Lloyd. A sensitivity matrix based methodology for inverse problem formulation. *J Inv Ill-Posed Problems*, 17:545–564, 2009.

[7] V. Bari E. Tobaldini A.C. Takahashi A.M. Catal A. Porta, T. Bassani and N. Montano. odel-based assessment of baroreflex and cardiopulmonary couplings during graded head-up tilt. *Comput Biol Med*, 42:298–305, 2011.

[8] S. Bastianini P. Lenzi A. Silvani, E. Magosso and M. Ursino. Mathematical modeling of cardiovascular coupling: Central autonomic commands and baroreflex control. *Auton Neurosci*, 162:66–71, 2011.

[9] AAS/AIAA Astrodynamics Specialist Conf. *A survey of numerical methods for optimal control.* AAS Paper 09-334 Pittsburg,PA, August 2009.

[10] T.G. Coleman A.C. Guyton and H.A. Granger. Overall regulation. *Ann Rev Phsiol*, 34:13–44, 1972.

[11] C.L. Darby M.A. Patterson C. Francolin I. Sanders A.V. Rao, D.A. Benson and G.T. Huntington. Algorithm 902: Gpops, a matlab software for solving multiple-phase optimal control problems using the gauss pseudo-spectral method. *ACM Transactions on Mathematical Software*, 22:1–39, 2010.

[12] D.A. Benson A.V. Rao and G.T. Huntington. User's manual for gpops version 5.0 : a matlab software for solving multiple-phase optimal control problems using hp-adaptive pseuodpectral methods.

[13] M.S Olufsen H. Tran N. Williams B. Matzuka, J. Mehlsen. A kalman filtering based approach for the modeling of the cardiovascular regualtion system. pages 107–112. The International Workshop on Innovative Simulation for Healthcare (IWISH), 2012.

[14] E.D. Gommer B. Spronck, E.G.H.J. Martens and F.N. van de Vosse. A lumped parameter model of cerebral blood flow control coupling combining cerebral autoregulation and neurovascular coupling. *Am J Physiol Heart Circ Physiol*, 303:H1143–H1153, 2012.

[15] J.T. Betts. Survey of numerical methods for trajectory optimization. *Jounral of Guidance, Control, and Dynamics*, 21(2):193, 1998.

[16] J.T. Betts and W.P. Huffman. Sparse optimal control software-socs. Technical report, Boeing Information and Support Services, 1997.

[17] L.T. Biedler and V.M. Zavala. Large-scale nonlinear programming using ipopt: an integrating framework for enterprise-wide optimization. *Computers and Chemical Egineering*, 33(3):575–582, 2008.

[18] K. Bischoff and R. Brown. Drug distribution in mammals. *Chemical Engineering Progess Symposium Series*, 62(66):33–45, 1966.

[19] H.G. Bock and K.J. Pitt. A multiple shooting algorithm for direct solution of optimal control problems. *IFAC 9th Worl COngress*, 1984.

[20] R. Burattini and P.O. Di Salvia. Development of systemic arterial mechanical properties from infancy to adulthood interpreted by four-element windkessel models. *J Appl Physiol*, 103(1):66–79, 2007.

[21] A.C. Burton. *Physiology and biophysics of the circulation*. Year Book Medical Publishers, Chicago, second edition, 1972.

[22] G. Rudofsky C. Kegler, M. Strunk. Venous pressure dynamics of the healthy human leg. *J Vasc Res*, (38):20–29, 2001.

[23] W.W. Hager D. Garg and A.V. Rao. Pseudospectral methods for solving infinite-horizon optimal control problems. *Automatica*, 47:829–837, 2011.

[24] H.T. Banks D. Bia Y. Zocalo R. Armentano D. Valdez-Jasso, M.A. Haider and M.S. Olufsen. Viscoelastic mapping of the arterial ovine system using a kelvin model. *IEEE Trans Biomed Eng*, 56:210–219, 2008.

[25] M. Danielsen. *Modeling of feedback mechanisms which control the heart function in a view to an implementation in cardovascular models*. PhD thesis, Department of Mathematics, Roskilde University, Denmark, 1998.

[26] M. Danielsen and J. Ottesen. Describing the pumpoing heart as a pressure source. *J Theor Biol*, 212:71–81, 2001.

[27] M. Danielsen and J.T. Ottesen. A dynamical approach to the baroreceptor regulation of the cardiovascular system. In *Symbiosis '97*, pages 25–29. Proceedings of the 5th International Symposium, 1997.

[28] M. Danielsen and J.T. Ottesen. A cardiovascular model. In *Applied Mathematical Models in Human Physiology*, chapter 6. SIAM, Philadelphia, 2004.

[29] J.A. David. *Optimal Control, Estimation, and Shape Deisgn: Analysis and Applications*. PhD thesis, North Carolina State University, 2007.

[30] J. Beneken & B. Dewitt. A physical approach to hemodynamic aspects of the human cardiovascular system. *Physical Bases of Circulatory Transport: Regulation and Exchange*, pages 1–45, 1967.

[31] D. Dochain and P.A. Vanrolleghem. *Dynamical modelling and estimation in wastewater treatment processes*. IWA Publishing, London, 2001.

[32] P.A. Low D.W. Robertson and R.J. Polinsky. *Primer on the autonomic nervous system*. Academic Press, San Diego, second edition, 2004.

[33] D.L. Eckberg. Arterial baroreflexes and cardiovascular modeling. *Cardiovasc Eng*, 8:5–13, 2008.

[34] L. Ellwein. *Cardiovascular and respiratory modeling*. PhD thesis, Dept of Mathematics, N.C. State University, Raleigh, NC, 2008.

[35] A. Engelsone. *Direct transcription methods in optimal control: theory and practice*. PhD thesis, Dept of Mathematics, N.C. State University, Raleigh, NC, 2006.

[36] M. Eslami. *Theory of sensitivity in dynamic systems: an introduction*. Springer, Berlin, 1994.

[37] M. Fink F. Kappel and J. Batzel. Aspects of control of the cardiovascular-respiratory system during orthostatic stress induced by lower body negative pressure. *Math Biosci*, 206:273–308, 2007.

[38] L. Antiga S. Merelli A. Veneziani G. Puppini G. Faggian-A. Mazzucco F. Viscardi, C. Vergara and G.B. Luciani. Comparative finite element model analysis of ascending aortic flow in bicuspid and tricuspid aortic valve. *Artificial Organs*, 34(12):1114–1120, 2010.

[39] U.J. Johannsen F.M. Abboud, D.L. Eckberg and A.L. Mark. Carotid and cardiopulmonary baroreceptor control of splanchnic and forearm vascular resistance during venous pooling in man. *J Physiol*, 286:173–184, 1979.

[40] R.S. Srinivasen F.M. Melchoir and J.B. Charles. Mathematical modeling of human cardiovascular system for simulation of orthostatic response. *Am J Physiol*, 262:H1920–H1933, 1992.

[41] B. Folkow and E. Neal. *Circulation*. Oxford Univ Press, 1971.

[42] S. Forth and M. Edvall. User guide for mad - a matlab automatic differentiation toolbox tomlab/mad version 1.4: The forward mode, 2007.

[43] S.I. Fox. *Human physiology*. McGraw-Hill, 2007.

[44] P. Frank. *Introduction to sensitivity theory*. Academic Press, New York, 1978.

[45] Y.C. Fung. *Biomechanics circulation*. W.B. Springer Verlag, New York, 1996.

[46] Divya Garg. *Advances in global pseudospectral methods for optimal control*. PhD thesis, University of Florida, 2011.

[47] R. Stevenson G.L. Brauer, D.E. Cornick. Capabilities and applications of the program to optimize and stimulate trajectories. Technical report, NASA, 1977.

[48] T.G. Glover and M.D. LeVan. Sensitivity analysis of adsorption bed behavior: Examination of pulse inputs and layered-bed optimization. *Chem Eng Sci*, 63(8):2086–2098, 2008.

[49] W. Grimm and A. Markl. Adjoint estimation from a multiple-shooting method. *Journal of Opti- mization Theory and Applications*, 92:263–283, 1997.

[50] F.S. Grodins. Integrative cardiovascular physiology: A mathematical synthesis of cardiac and blood vessel hemodynamics. *Q Rev Biol*, 34:93–116, 1959.

[51] A.C. Guyton and J.E. Hall. *Textbook of medical physiology*. W.B. Saunders Company, Philadelphia, 1996.

[52] A.S. Perelson H. Miao, X. Xia and H. Wu. On indentifiability of nonlinear ode models and applications in viral dynamics. *SIAM Rev Soc Ind Appl Math*, 53(1):3–39, 2011.

[53] H. Herzel H. Siedel and D.L. Eckberg. Phase dependencies of the human baroreceptor reflex. *Am J Physiol*, 272:H2040–H2053, 1997.

[54] K. Sagawa H. Suga and A.A. Shoukas. Load independence of the instantaneous pressure-volume ratio of the canine left ventricle and effects of epinephrine and heart rate on the ratio. *Circulation Research*, 32:314–322, 1973.

[55] C.A. Swenne B.J. TenVoorde H. van de Vooren, M.G.J. Gademan, M.J. Schali, and E.E. Wall. Baroreflex sensitivity, blood pressure buffering, and resonance: what are the links? computer simulation of healthy subjects and heart failure patients. *J Appl Physiol*, 102(4):1348–1356., 2007.

[56] J. Knowles H. Wang D.S. Broomhead H. Yue, M. Brown and D.B. Kell. Insights into the behavior of systems biology models from dynamic sensitivity and identifiability analysis: a case study of an nf-kb signalling pathway. *Mol BioSyst*, 2:640–649, 2006.

[57] A.V. Kamyad H. Zarei and S. Effati. Multiobjective optimal control of hiv dynamics. *Math Prob Eng*, 2010:29 pages, 2010.

[58] C.R. Hargraves and S.W. Paris. Direct trajectory optimization using nonlinear programming and collocation. *Jounral of Guidance, Control, and Dynamics*, 10(4):338–342, 1987.

[59] J.R. Samuels H.T. Banks, M. Davidian and K.L. Sutton. An inverse problem statistical methodology summary. In L.M.A. Bettencourt G. Chowell, J.M. Hyman and C. Castillo-Chavez, editors, *Mathematical and statistical estimation approaches in epidemiology*. Springer-Verlag, 2009.

[60] C.T. Kelley I. Ipsen and S.R. Pope. Rank-deficient nonlinear least squares problems and subset selection. *J Numer Anal*, 49:1244–1266, 2011.

[61] J. Mandel R. Prutow J. Martin, A. Schneider and N. Smith. A new cardiovascular model for real-time applications. *Transactions*, 3:31–65, 1986.

[62] R.A. Rifle J. Melbin, D.K. Detweiler and A. Noordergraaf. Coherence of cardiac output with rate changes. *Am J Physiol*, 243:H499–H504, 1982.

[63] J. Mehlsen M. Brackle M. Stubgaard J. Møgelvang, C. Thomsen and O. Henriksen. Evaluation of left ventricular volumes measured by magnetic resonance imaging. *Eur Heart J*, 7:1016–1021, 1986.

[64] M.B. Mote J.B. Lanier and E.C. Clay. Evaluation and management of orthostatic hypotension. *Am Fam Physician*, 84:527–536, 2011.

[65] D. Khoury F. Ghorbel J.B. Olansen, J.W. Clark and A. Bidani. A closed-loop model of the canine cardiovascular system that includes ventricular interaction. *Computers and Biomedical Research*, 33(4):260–295, 2000.

[66] D. Schneditz J.J. Batzel, F. Kappel and H. T. Tran. *Cardiovascular and respiratory systems: modeling, analysis, and control.* SIAM, Philadelphia, 2007.

[67] H.K. Lackner A. Roessler M. Bachar F. Kappel J.J. Batzel, N. Goswami and H. Hinghofer-Szalkay. Patterns of cardiovascular control during repeated tests of orthostatic loading. *Cardiovasc Eng*, 9(4):134–143, 2009.

[68] S. Timischi-Teschl J.J. Batzel and F. Kappel. A cardiovascular-respiratory control system model including state delay with application to congestive heart failure in humans. *J Math Biol*, 50:293–335, 2005.

[69] C.W. Wouters M. Kooijman J.T. Groothius, F. Poelkens and M.T.E. Hopman. Leg intravenous pressure during head-up tilt. *J Appl Physiol*, 105:811–815, 2008.

[70] M. Saeed T. Heldt J.X. Sun, A.T. Reisner and R.G. Mark. The cardiac output from blood pressure algorithms trial. *Crit Care Med*, 37:72–80, 2009.

[71] H. Akimoto K. Enishi, F. Tajima and R. Mita. Initial drop of blood pressure during head-up tilt in patients with cerebrovascular accidents. *Environ Health and Prev Med*, 9:228–233, 2004.

[72] W.J. Stok S. Dijkstra K. van Heusden, J. Gislof and J.M. Karemaker. Mathematical modeling of gravitational effects on the circulation: importance of the time course of venous pooling and blood volume changes in the lungs. *Am J Physiol*, 291:H2152–H2165, 2006.

[73] F. Kappel and R. Peer. A mathematical model for fundamental regulation processes in the cardiovascular system. *J Math Biol*, 31:611–631, 1993.

[74] H.B. Keller. *Numerical Solution of Two Point Boundary Value Problems.* SIAM, 1976.

[75] C.T. Kelley. *Iterative Methods for Optimization.* SIAM, Philadelphia, 1999.

[76] J.J. Settels K.H. Wesseling, J.R.C. Jansen and J.J. Screuder. Computation of aortic flow from pressure in humans using a nonlinear three-element model. *J Appl Physiol*, 74:2566–2573, 1993.

[77] R.E. Klabunde. *Cardiovascular physiology concepts.* Lippincot, Williams and Wilkins, Philadelphia, 2011.

[78] D. Kraft. On converting optimal control problems into nonlinear programming codes. In *NATO ASI Series,Computational Mathematical Programming*, pages 261–280. Springer-Verlag, Berlin, 1985.

[79] W.P. Santamore L. Sheffer and O. Barnea. Cardiovascular simulation toolbox. *Cardiovasc Eng*, 7:81–88, 2007.

[80] J.R. Levick. *An introduction to cardiovascular physiology.* Hodder Arnold Publishers, 5th edition, 2010.

[81] F.L. Lewis and V.L. Syrmos. *Optimal Control.* John WIley & Sons, Inc, second edition, 1995.

[82] F.L. Lewis and V.L. Syrmos. Stroke volume of the heart and thoracic fluid content during head up and head down tilt in humans. *Acta Anaestisiol Scand*, 49:1287–1292, 2005.

[83] A. Xie J.J. Batzel C.T. Kelley L.M. Ellwein, S.R. Pope and M.S. Olufsen. Modeling cardiovascular and respiration dynamics in congestive heart failure. *Math Biosci*, 241:56–74, 2013.

[84] A. Xie J.J. Batzel C.T. Kelley L.M. Ellwein, S.R. Pope and M.S. Olufsen. Patient-specific modeling of cardiovascular and respiratory dynamics during hypercapnia. *Math Biosci*, 241:56–74, 2013.

[85] J.J. Batzel M. Fink and F. Kappel. An optimal control approach to modeling the cardiovascular-respiratory system: an application to orthostatic stress. *Cardiovasc Eng*, 4:27–38, 2004.

[86] Microwave and Telecommunication Technology 15th International Crimean Conference. *Snap analysis of cardiovascular system based on inductance-capacitance heart model*, volume 2, 2005.

[87] S. Middleman. *Transport Phenomena in the Circulatory System*. Wiley-Interscience, New York, 1972.

[88] T.H. Miller and J.E. Kruse. Evaluation of syncope. *Am Fam Physician*, 72:1492–1500, 2005.

[89] J. Morio. Global and local sensitivity analysis methods for a physical system. *European J Phys*, 32(6):1577–1583, 2011.

[90] M. Jenstrup F. Potts M.P.M. Harms, J.J. van Lieshout and N.H. Secher. Postural effects on cardiac output and mixed venous oxygen saturation in humans. *Exp Physiol*, 88:611–616, 2003.

[91] H.T. Tran M.S. Olufsen and J.T. Ottesen. Modeling cerebral blood flow control during posture change from sitting to standing. *J Appl Physiol*, 4(1):47–58, 2004.

[92] H.T. Tran REU L.A. Lipsitz M.S. Olufsen, J.T. Ottesen and V. Novak. Modeling barore-flex regulation of heart rate during orthostatic stress. *Am J Physiol*, 4:R1368–R1455, 2006.

[93] J.T. Ottesen L.M. Ellwein L.A. Lipsitz M.S. Olufsen, H.T. Tran and V. Novak. Blood pressure and blood flow variation during postural change from sitting to standing - modeling and experimental validation. *J Appl Physiol*, 99(4):1523–1537, 2005.

[94] L.A. Lipsitz M.S. Olufsen, A Nadim. Dynamics of cerebral blood flow regulation explained using a lumped parameter model. *Am J Physiol*, 282:R611–R622, 2002.

[95] H.T. Tran J.T. Ottesen M.S.Olufsen, A. Alston and V. Novak. Modeling heart rate regulation - part i: Sit-to-stand versus head-up tilt. *Cardiovasc Eng*, 8(73-87), 2008.

[96] J.P. Mulier. *Ventricular pressure as a function of volume and flow*. PhD thesis, University of Leuven, Belgium, 1994.

[97] J. Meister N. Stergiopoulos and N. Westerhof. Determinants of stroke volume and systolic and diastolic aortic pressure. *Am J Physiol*, 270:H2050–H2059, 1996.

[98] H.T. Tran N.D. Williams and M.S. Olufsen. An optimal control approach to modeling head-up tilt. pages 97–102. Int. Wksp. on Innovative Simulation for Healthcare, September 25-27 2013.

[99] REU Program J. Mehlsen J. Ottesen N.D. WIlliams, O. Wind-Willassen and M.S. Olufsen. Patient specific modeling of head-up tilt. *Math Med Biol*, In press.

[100] R.M. Neilan and S. Lenhart. An introduction to optimal control with an applicatoin in dieasea modeling. *DIMACS Series in Discrete Math and Theor Comp Sci*, 75:67–81, 2010.

[101] J.A. Nelder and R. Mead. A simplex method for function minimization. *Computer Journal*, 7:308–313, 1965.

[102] S. Neumann. *Modeling Acute Hemorrhage in the Human Cardiovascular System*. PhD thesis, University of Pennsylvania, Philadelphia, 1996.

[103] A. Noordergraaf. *Circulatory system dynamics*. Academic Press, New York, 1978.

[104] M.S. Olufsen and J.T. Ottesen. A practical approach to parameter estimation applied to model predicting heart rate regulation. *J Math Biol*, 67(1):39–68, 2012.

[105] J. Ottesen. Modeling of the baroreflex-feedback mechanism with time-delay. *J Math Biol*, 36:41–63, 1997.

[106] J.T. Ottesen. *General compartmental models of the cardiovascular system*. IOS Press, Amsterdam, 2000.

[107] J.T. Ottesen and M. Danielsen. Modeling ventricular contraction with heart rate changes. *J Theor Biol*, 222:337–346, 2003.

[108] M. Afanasyeva H.C. Champion D.P. Judge H.D. Millar P. Verdonck-D.A. Kass N. Stergiopulos P. Segers, D. Georgakopoulos and N. Westerhof. Conductance catheter-based assessment of arterial input impedance, arterial function, and ventricular-vascular interaction in mice. *Am J Physiol Heart Circ Physiol*, 288:H1157–H1164, 2004.

[109] T. de Backer S. Carlier P. Verdonck P. Segers, A. Qasem and A. Avolio. eripheral "oscillatory" compliance is associated with aortic augmentation index. *Hypertension*, 37:1434–1439, 2001.

[110] M.A. Saunders P.E. Gill, W. Murray and M.H. Wright. User's guide for npsol (version 4.0): a fortran package for nonlinear programming. Technical report, Department of Operations Reserch, Stanford University, January 1986.

[111] W. Murray P.E. Gill and M.A. Saunders. Snopt: an sqp algorithm for large-scale constrained optimization. *SIAM J Optim*, 12(4):979–1006, 2002.

[112] C.S. Peskin and D.M. McQueen. A three-dimensional computational method for blood flow in the heart. i. immersed elastic fibers in a viscous incompressible fluid. *J Comp Physics*, 81(2):372–405, 1989.

[113] T.G. Pickering. Orthostaic intolerance. *J Clinical Hypertension*, 4:306–308, 2002.

[114] L.G. De Pillis and A. Radunskaya. The dynamics of an optimally controlled tumor model: a case study. *Mathematical and Computer Modelling*, 37:1221–1244, 2003.

[115] A. Bhattacharya P.N. Dwivedi and R. Padhi. Suboptimal midcourse guidance of interceptors for high-speed targets with alignment angle constraint suboptimal midcourse guidance of interceptors for high-speed targets with alignment angle constraint read more: http://arc.aiaa.org/doi/abs/10.2514/3.28907?journalcode=jsr. *J Guidance, Control, and Dynamics*, 34(3):860–877, 2011.

[116] H. Mehmanesh C.F. Vahl R. Bauernschmitt, S. Schulz and R. Lange. Simulation of baroreflex control in a pulsatile mathematical model of the human arterial circulation. *Comp Cardiol*, 26:229–232, 1999.

[117] J. Nocedal R.H. Byrd and R.A. Waltz. Knitro:an integrated package for nonlinear optimization. *Large Scale Nonlinear Optimization*, pages 35–59, 2006.

[118] V. Rideout. *Mathematical and Computer Modeling of Physiological Systems*. Prentice Hall, New Jersey, 1991.

[119] A.L. Imholz R.L. Sprangers, K.H. Wesseling and W. Weiling. Initial blood pressure fall on stand up and exercise explained by changes in total peripheral resistance. *J Appl Physiol*, 70:523–530, 1991.

[120] I.M. Ross and F. Fahroo. User's manual for dido 2001: a matlab application for solving optimal control problems. Technical report, Department of Aeronautics and Astronautics, Naval Postgraduate School, 2001.

[121] L.B. Rowell. Ideas about control of skeletal and cardiac muscle blood flow (1876-2003): cycles of revision and new vision. *J Appl Physiol*, 97:384–392, 2004.

[122] H. Seywald R.R. Kumar and E.M. Cliff. Near-optimal three-dimensional air-to-air missile guidance against maneuvering target. *J Guidance, Control, and Dynamics*, 18(3):457–464, 1995.

[123] S. Groth D.B. Friedman S. Matzen, G. Perko and N.H. Secher. Blood volume distribution during head-up tilt induced central hypovolaemia in man. *Clin Physiol*, 11:411–422, 1991.

[124] Q. Barnes W.L. Eubank M.N. Hawkins S. Purkayatha A. O-Yurvati S. Ogoh, R.M. Brothers and P.B. Raven. ffects of changes in central blood volume on carotid-vasomotor baroreflex sensitivity at rest and during exercise. *J Appl Physiol*, 101:68–75, 2006.

[125] G. Clermont S. Zenker, J. Rubin. From inverse problems in mathematical physiology to quantitative differential diagnoses. *PloS Comp Biol*, 3:2072–2086, 2007.

[126] A.E. Sabroff. Advanced spacecraft stabilization and control techniques. *Journal of Spacecraft and Rockets*, 5:1377–1393, 1968.

[127] H. Seywald and R.R. Kumar. Method for automatic costate calculation. *Jounral of Guidance, Control, and Dynamics*, 19(6):1252–1261, 1996.

[128] W. Shoemaker. Fluids and electrolytes in the acutely ill adult. In *Textbook of critical care*. W.B. Saunders Company, Philadelphia, 1989.

[129] A.W. Cowley S.M. Bugenhagen and D.A. Beard. Identifying physiological origins of baroreflex dysfunction in salt-sensitive hypertension in the dahl ss rat. *Physiol Genomics*, 42:23–41, 2010.

[130] J.J. Smith and J.P. Kampine. *Circulatory physiology-the essentials*. The Williams & Wilkins Company, Baltimore, 1990.

[131] C.L. Zapata V. Novak C.T. Kelly S.R. Pope, L.M. Ellwein and M.S. Olufsen. Estimation and identification of parameters in a lumped cerebrovascular model. *Math Biosci Eng*, 6:93–115, 2009.

[132] J. Stoer and R. Bulirsch. *Introduction to Numerical Analysis.* Springer-Verlag, 2002.

[133] G.V. Ranade T.A. Parklikar, T. Heldt and G.C. Verghese. Model-based estimation of cardiac output and total peripheral resistance. *Comp Cardiol*, 34:379–382, 2007.

[134] B.J. TenVoorde and R. Kingma. A baroreflex model of short term blood pressure and heart rate variability. *Math Modeling Med*, 71, 2000.

[135] R.Y. Tham. *A Study of Effects of Halothane on Canine Cardiovascular System and Baroreceptor Control,.* PhD thesis, University of Wisconsin, Madison, 1988.

[136] G.J. Tortora. *Principles of anatomy and physiology.* Harper & Row, New York, 1990.

[137] J.K. Triedman and J.P. Saul. lood pressure modulation by central venous pressure and respiration. buffering effects of the heart rate reflexes. *Circulation*, 89:169–179, 1994.

[138] M. Ursino. Interaction between carotid baroregulation and the pulsating heart: a mathematical model. *Am J Physiol*, 44:H1733–H1747, 1998.

[139] M. Ursino. A mathematical model of the carotid baroregulation in pulsating conditions. *IEEE Trans Biomed Eng*, 46:382–392, 1999.

[140] M. Ursino. Modelling the interaction among several mechanisms in the short-term arterial pressure control. In M. Danielsen and J. Ottesen, editors, *Mathematical Modeling in Medicine*, pages 139–162. IOS Press, Philadelphia, 2000.

[141] G. Le Vey and C. Vermeiren. *hort term autonomic nervous control of the cardiovascular system: A system theoretic approach.* IOS Press, Amsterdam, 2000.

[142] O. von Stryk. Numerical solution of optimal control problems by direct collocation. *Interational Series of Numerical Mathematics*, 111:129–143, 1993.

[143] O. von Stryk. User's guide for dircol version 2.1: A direct collocation method for the numerical solution of optimal control problems. Technical report, Technische Universitat Darmstadt, 1999.

[144] O. von Stryk and R. Bulirsch. Direct and indirect methods for trajectory optimization. *Annals of Operation Research*, 37(1):357–373, 1992.

[145] W. Kroon R.N. Planken J.H.M. Tordoir W. Huberts, A.S. Bode and F.N. van de Vosse. A pulsewave propagation model to support decision-making in vascular access planning in the clinic. *Med Eng Phys*, 34:233–248, 2011.

[146] A.D. ten Harkel J.J. Lieshout W. Wieling, M.P. Harms and R.L. Sprangers. Circulatory response evoked by a 3s bout of dynamic leg exercise in humans. *J Physiol*, 494:601–611, 1996.

[147] F.S. Wang W.H. Wu and M.S. Chang. Sensitivity analysis of dynamic biological systems with time-delays. In *BMC BioInformatics*, volume 11. 9th International Conference on Bioinformatics, Biomed Central, England, 2010.

[148] W.E. Williamson. Use of polynomial approximations to calculate suboptimal controls. *AIAA Jounral*, 9(11):2271–2273, 1971.

[149] L. Qi X. Chen and K.L. Teo. Smooth convex approximation to the maximum eigenvalue function. *J Global Opt*, 30:253–270, 2004.

[150] E.N. Brown Z. Chen, P.L. Purdon and R. Barbieri. A differential autoregressive modeling approach within a point process framework for non-stationary heartbeat intervals analysis. *Conf Proc IEEE Eng Med Biol Soc*, 2010:3567–3570, 2010.